UNIVERSITY OF CALIFORNIA
RIVERSIDE

Colloidal Synthesis and Assembly of Functional Nanomaterials

A Dissertation submitted in partial satisfaction
of the requirements for the degree of

Doctor of Philosophy

in

Materials Science and Engineering

by

Yiding Liu

June 2015

Dissertation Committee:
Dr. Yadong Yin, Chairperson
Dr. Elaine D. Haberer
Dr. Jianlin Liu

The Dissertation of Yiding Liu is approved:

_____

_____

_____

Committee Chairperson

University of California, Riverside

Acknowledgements

I regard the past five years as one of the critical period during my lifetime. Although everyday life here in Riverside is rather simple as most of the time was spent in the lab, it witnessed a significant improvement of myself, as a human being: rapid growth in knowledge, deeper understanding in philosophy, broader experiences in life and finally, finishing my Ph. D study. However, it is difficult for me to imagine without continuous guidance, help and support from different people around me, I can obtain these achievements. Thus, I am taking this opportunity to convey my most sincere thanks to all of them.

First, I would like to express my deepest gratitude to my Ph. D advisor, Professor Yadong Yin, who offered me valuable guidance and continuous support, not only in academic but also in life. Academically, he is insightful and acute. As an advisor, he is extremely patient and cheerful. Therefore, under his supervision, I was able to acquire proficiency in a variety of scientific research skills starting from zero experience. In daily life, I was also influenced by a lot of his precious personalities. Definitely Yadong is my role model in my future life and career. I am also thankful to my defense committee members – Professor Elaine D. Haberer and Professor Jianlin Liu, for their valuable comments and advice on my dissertation.

Besides, I am grateful to all of my lab colleagues for their inspirations and collaborations. I will cherish this great working experience and the friendship with all of them. I here want to acknowledge my special thanks to: Dr. Xiaogang Han, Dr. Qiao Zhang, Dr. Chuanbo Gao, Dr, James Goebl, Dr. Aiwei Tang, Dr. Xiaofang Liu, Dr.

Jingbing Liu, Dr. Guoqing Wang, Yaocai Bai, Lishun Fu and Dawei Wang and undergraduate students: Shelly See and Chiranj Modi, who have collaborated with me on different research projects. My special thanks also go to Dr. Yu Lu for her assistance in scientific research and helpful tips in daily life. I thank Dr. Krassimir N. Bozhilov, Stephen McDaniel and Mathias Rommelfanger for assistance in using facilities in CFAMM, Dr. Dan Borchardt for assistance in using optical facilities in Chemistry Department.

Most importantly, I must thank my parents Ling Yang and Qizhi Liu who had brought me to this world for their understandings and continuous support, my grandparents Zufang Liu and Yongxi Yang for their forgiveness on my long term absence from home, and all of other family members for everything they have done for me.

Last but not least, I thank Rachel Cui, Fei Bu, Yuanhang Huang, Mingsheng Wang, Chen Yang, Yang Li, Quan Ma, Wei Wang, Lei Guo and all other friends who have helped me and shared my happiness and sorrow.

Dedication

To my family

ABSTRACT OF THE DISSERTATION

Colloidal Synthesis and Assembly of Functional Nanomaterials

by

Yiding Liu

Doctor of Philosophy, Graduate Program in Materials Science and Engineering
University of California, Riverside, June 2015
Dr. Yadong Yin, Chairperson

In this dissertation, I present my research on the colloidal synthesis of anatase titanium dioxide nanocrystals and reversible assembly of charged gold nanoparticles as well as the applications of these novel nanomaterials.

Titanium dioxide nanomaterials are well known for their photoactive properties and have been used in a variety of energy and environmental applications. Since the structural factors of TiO_2 nanomaterials including size, shape, crystallinity have significant effects on their performance in these applications, it is highly demanded to develop robust synthesis methods for the production of TiO_2 nanomaterials with highly configurable and predictable structure and morphology. Herein, a systematic study on shape controlled synthesis of anatase TiO_2 nanocrystals was carried out. Synthesis and shape transformation of anatase TiO_2 nanocrystals with controllable exposing facets were realized by a nonaqueous sol-gel pyrolysis reaction with the addition of fluorine as shape-directing agent. Anatase TiO_2 nanocrystals with core-antenna morphology were further produced by a seed-mediated growth method. When used in photocatalytic reactions, the

core-antenna nanocrystals were found to possess superior photocatalytic activities than those with simple morphologies. The high structural configurability of the core-antenna nanocrystals made it possible to optimize the catalyst parameters and achieve excellent photocatalytic performance.

Noble metal nanoparticles possess novel optical properties due to surface plasmon resonance. Since assembly of plasmonic nanoparticles induces plasmon coupling between adjacent nanoparticles and results in optical property change, realization of reversible assembly of plasmonic nanoparticles can enable dynamic tuning of the optical properties of the materials. In our study, theoretical considerations on how to realize reversible assembly by control of colloidal interactions were first discussed. Experimentally, one-dimensional assembly and disassembly of gold nanoparticles were achieved by appropriate synthesis, surface modification and application of external stimuli. Kinetics study of the reversible assembly process was also carried out. When the as-assembled one-dimensional gold nanoparticle chain structures were transferred into polymer matrices, they can also be disrupted by mechanical forces and be used as colorimetric stress memorable sensor.

Based on the results of my current research, future works of the study on colloidal synthesis of TiO_2 nanocrystals and reversible assembly of plasmonic nanoparticles will also be discussed.

Table of Content

Abstract of The Dissertation vii

List of Figures xii

Chapter 1 Overview of Colloidal Nanomaterials 1

1.1 Brief introduction to nanotechnology 1

1.2 Colloidal synthesis of nanocrystals 3

1.2.1 General understandings of colloidal synthesis of nanocrystals 3

1.2.2 Strategies towards size control in colloidal synthesis 9

1.2.3 Strategies toward shape control in colloidal synthesis 14

1.2.4 Template synthesis – an extension 17

1.2.5 Challenges in Future Applications 18

1.3 Self-assembly of colloidal nanoparticles 19

1.3.1 General introduction 19

1.3.2 Colloidal interactions 23

1.3.3 Self-assembly of nanoparticles at different dimensions 27

1.4 The Scope of This Thesis 30

Chapter 2 Shape Control Synthesis of Anatase TiO2 Nanocrystals and Their Application in Photocatalysis 32

2.1 Introduction 32

2.2 Experimental Methods 36

2.2.1 Chemicals 36

2.2.2 Syntheses 37

2.2.3 Structural Characterizations 40

2.2.4 Photocatalysis 41

2.3 Shape control of anatase TiO_2 nanocrystals by addition of fluorine ions 42

2.3.1 Transformation of anatase TiO_2 nanorods 43

2.3.2 One-pot synthesis of fluorine doped TOB-shaped nanocrystals 45

2.4 Seed-mediated growth of anatase TiO_2 nanocrystals with core-antenna structures 50

2.4.1 Synthesis of broom-like core-antenna nanocrystals 50

2.4.2 Formation mechanism of core-antenna nanocrystals 52

2.4.3 Control the growth by manipulating the growth kinetics 63

2.4.4 Growth on seeds with different shapes 66

2.5 Photocatalytic performance of anatase TiO_2 nanocrystals with different shapes[71

2.5.1 Phase transfer of nanocrystals 71

2.5.2 Photocatalytic activities of nanocrystals with different shapes 72

2.6 Conclusions 78

Chapter 3 Reversible One-Dimensional Assembly of Charged Gold Nanoparticles and Its Applications 81

3.1 Introduction 81

3.2 Experimental methods 87

3.2.1 Chemicals 87

3.2.2 Synthesis and ligand exchange of AuNPs 88

3.2.3 Thermoresponsive assembly and disassembly of AuNPs 88

3.2.4 Kinetics study 89

3.2.5 Studies on AuNPs-polymer composite films 89

3.3 Theoretical study on reversible assembly of AuNPs 90

3.3.1 Thermodynamics of reversible assembly of AuNPs 91

3.3.2 Kinetics of reversible assembly of AuNPs 105

3.4 Colorimetric stress memory sensor based on disassembly of gold nanoparticle chains 109

3.5 Conclusions 121

Chapter 4 Conclusion and Outlook 124

4.1 Conclusion of this thesis 124

4.2 Outlook and future work 126

References 130

List of Figures

Figure 1.1 (a) The La Mer plot which describes the nucleation and growth of nanoparticles as a function of reaction time. (b) The plot which demonstrate the free Gibbs energy change as a function of the radius of nucleus during the nucleation process. (Page 8)

Figure 1.2 Schematic illustration of size control of nanocrystals by (a) size focusing and (b) seed-mediated growth. (Page 13)

Figure 1.3 Schematic illustration of ideal self-assembly process. (a) the interaction energy requirement: a net attraction at equilibrium separation, overall a balance between attraction and repulsion. (b) irreversible assembly results in random aggregation. (c, d) reversible assembly enables building blocks self-adjust to ordered structures. (Page 22)

Figure 2.1 (a, b) Schematic illustrations of the Wulff shapes of rutile phase (a) and anatase phase (b) titanium dioxide. (c) Schematic illustration of the principle of photocatalytic reactions by using titanium dioxide as catalyst. (Page 35)

Figure 2.2 Transformation of nanorods to bipyramidal nanocrystals. TEM images of (a) as-obtained TiO_2 nanorods; (b-c) after adding NaF for (b) 30 min; and (c) 2 hours. (Page 47)

Figure 2.3 TEM images showing the evolution process of TiO_2 nanocrystals with TOB shape in one-pot synthesis. (a-e) TEM images of the as-prepared nanocrystals by taking samples from the reaction system at (a) 250 °C and after reacted at 270 °C for (b) 1 min; (c) 5 min; (d) 10 min; (e) 30 min; and (f) 180 min. The HRTEM images (g) and (h) show the crystal structure of the as-obtained nanocrystals. (Page 48)

Figure 2.4 (a) XRD characterization of the aliquots during the synthesis. It proved a successful dissolution of NaF and a continuous growth of anatase TiO_2. (b-e) UV-vis absorption spectra (b) and XPS measurement confirmed the fluorine doping in the product nanocrystals (c-e). (Page 49)

Figure 2.5 Structural characterization of TOB nanocrystal seeds and core-antenna nanocrystals after seed-mediated growth. (a, c) Low magnification TEM image of TOB and core-antenna nanocrystals. (b, d) Typical HRTEM images of TOB and core-antenna nanocrystals. Insets in (b) and (d) are the corresponding FFT patterns (along [100] zone axis). (e) XRD patterns of TOB and core-antenna nanocrystals. (Page 53)

Figure 2.6 The effect of heating time on the morphology of the core-antenna nanocrystals. (a, b) TEM images of the core-antenna nanocrystals synthesized (a) right after the complete addition of precursor solution and (b) with 1 hour of additional heating at 270 ℃. (c) Plot showing the dependence of the length of antenna nanorods on additional heating time. (Page 57)

Figure 2.7 TEM and HRTEM images of nanocrystals synthesized with (a, b) 0.5 mL and (c, d) 2.0 mL of TBOT under the typical conditions. Insets in (b) and (d) are the corresponding FFT patterns (along [100] zone axis). The arrows in d) indicate the <001> direction. (Page 58)

Figure 2.8 Schematic illustration showing the growth pathway of core-antenna nanostructures from TOB-shaped seeds. (Page 59)

Figure 2.9 TEM and HRTEM images of (a-c) rhombic anatase TiO_2 nanocrystal seeds and (d-f) the resultant nanocrystals after seeded growth. (Page 62)

Figure 2.10 The effect of TBOT feeding rate on the growth behavior. (a-d) TEM images of resultant nanocrystals with introduction rate at (a) 1.0 mL/h, (b) 2.0 mL/h, (c) 6.0 mL/h, and (d) quick injection. (e) Change of length, diameter of the longest antenna nanorods with the change of the TBOT feeding rate. (Page 65)

Figure 2.11 Growth of TiO_2 nanorods on nanorod seeds. (a) TEM image of anatase TiO_2 nanorod seeds. (b) TEM image of the elongated nanorods after seeded growth. (c) Schematic illustration of the growth behavior. (Page 69)

Figure 2.12 Seed-mediated growth of TiO_2 nanorods on square-shaped nanoplates. (a, b) TEM images of nanoplate seeds horizontally lying (a) and vertically stand (b) on the grids. (c, d) TEM images of brush-like nanocrystals produced by addition of 0.5 mL (c) and 1.0 mL (d) of TBOT. (e) Schematic illustration of the growth behavior and representative brush-like nanocrystals imaged at different orientation. (Page 70)

Figure 2.13 Phase transfer of core-antenna nanocrystals (a) TEM image of the typical broom-like nanocrystals prepared with addition of 2.0 mL TBOT at the rate of 3.0 mL/h. (b) TEM image of broom-like nanocrystals after phase transfer to water. (c) FTIR spectra of nanocrystals before and after phase transfer. (Page 76)

Figure 2.14 The photocatalytic activity of anatase TiO_2 nanocrystals with different morphologies. (a) Change of RhB concentration versus UV irradiation time when nanorods, nanoplates, brush-like TiO_2 nanocrystals synthesized by addition of different amount of TBOT and commercial P25 were used as the catalysts. (b) Change of RhB concentration versus UV irradiation time when TOB nanocrystals, broom-like TiO_2 nanocrystals synthesized by addition of 2 mL of TBOT at different addition rate and commercial P25 were used as the catalysts. (Page 77)

Figure 3.1 (a) Schematic illustration of interactions between light and plasmonic nanoparticles and induced localized surface plasmon resonance (LSPR). (b) The relationship between interparticle distance, chain length and plasmon coupling peak position in one-dimensional assembly of plasmonic nanoparticles. (Page 86)

Figure 3.2 TEM images of (a) the as-synthesized charged AuNPs and (b) the chain-like AuNP assemblies prepared at 5°C in the presence of salt. To prepare the TEM sample of (b), a drop of AuNP assembly solution was supported on a carbon coated copper grid and then freeze-dried at a low temperature achieved using dry ice. (Page 94)

Figure 3.3 The thermoresponsive tuning of plasmonic properties of charged colloidal AuNPs: (a) schematic illustration and photos showing AuNPs switching between the disassembled and assembled states in response to temperature changes, (b) the extinction spectra of a typical AuNP dispersion when cooled from 40 ℃ to 5 ℃, and (c) the extinction spectra of the same sample when heated from 5 ℃ back to 40 ℃. There is a 5 ℃ temperature difference between each neighboring spectrum. (Page 95)

Figure 3.4 (a) The extinction spectra of a typical AuNP dispersion during 9 cycles of repeated heating (at 40 ℃) and cooling (at 5 ℃). (b) The repeated switching of plasmonic peak positions (isotropic peak at 40 ℃ and coupling peak at 5 ℃) for nine cycles. (Page 96)

Figure 3.5 (a) Zeta potential vs. temperature plotted for colloidal AuNPs in 0.09 M NaCl aqueous solution. (b) Interparticle energy vs. interparticle distance plot of AuNPs in 0.09 M NaCl aqueous solution. (Page 102)

Figure 3.6 The extinction spectra measured at 40 ℃ and 5 ℃ for AuNP dispersions containing (a) 0.05 M and (b) 0.13 M of NaCl, and the plots showing the interparticle energy vs. separation calculated for various temperatures for AuNP dispersions containing (c) 0.05 M and (d) 0.13 M of NaCl. (Page 103)

Figure 3.7 (a, b) The extinction spectra of samples with different AuNPs concentration at (a) 40 ℃ and (b) 5 ℃. (c, d) The extinction spectra of samples with different agarose concentration at (c) 40 ℃ and (d) 5 ℃. (Page 104)

Figure 3.8 Temperature path-dependence in thermoresponsive assembly. (a) The initial state of the assembly process. Initially, nanoparticles are at different temperatures. At higher temperature, more isolated particles and fewer aggregates and vice versa. (b) Final states of the assembly repeatedly start from 40 °C, show nearly identical optical properties. (c) Final states of the

assembly started from different temperature, show distinctive different optical properties. (Page 107)

Figure 3.9 Schematic illustration of the design of the stress-responsive colorimetric film based on disassembly of gold nanoparticle chains in a polymer flow. (Page 115)

Figure 3.10 Fabrication of the composite film and its pressure-responsive color switching performance. (a) Illustration of film fabrication procedure and compression test results. (b, c) Normalized UV-Vis extinction profiles for films before/after pressing (b) and the nanoparticle suspensions recovered from both films (c). (Page 116)

Figure 3.11 (a) The UV-Vis extinction spectra of a typical composite film after experiencing different pressures for a fixed application time (1 min). (b) The CWT of the spectra in (a). (c) Physical deformation profiles of the film after being subjected to various pressures for 1 min. (d) Plot of coupling peak position shift for films experiencing different pressures and application times (1 min and 5 min). (Page 117)

Figure 3.12 Tuning the sensitivity of the optical change to stress by doping the composite film with plasticizer. (a) UV-Vis extinction spectra (left) and their CWT profiles (right) for films doped with different amounts of PEG before (dot) and after (line) being treated with 1.6×10^4 psi of pressure for 1 min. (b) Plot of pressure-dependent coupling peak shift for films doped with different amounts of PEG (press time is 1 min). (c) Digital images of films doped with 11 wt % PEG after experiencing different pressures for 1 min. (d) Deformation profiles of films without and with 17 wt % PEG doping under different pressures for 1 min. (Page 118)

Chapter 1

Overview of Colloidal Nanomaterials

1.1 Brief introduction to nanotechnology

Date back to ancient times, nanoscale materials have already been existed in nature and been manipulated by human beings for different applications. As an example, the Romans made the dichromic Lycurgus Cup in the 4th century which contains gold and silver nanoparticles. Benefit from the light absorption and scattering properties of these nanoparticles, the cup shows red color when lit from inside and green color when lit from outside. In scientific studies, as early as in 1857, Michael Faraday had noticed the unusual ruby red color of colloidal gold produced by chemical synthesis.[1] However, not until Richard Feynman's famous talk was delivered in 1959 which predicted "there is plenty of room at the bottom", people's understanding of nanoscale materials and their properties start becoming rational. Gradually, nanotechnology becomes a field of study with solid theoretical foundations and explicit objectives.

Now, it is commonly agreed nanotechnology is a collection of research areas aiming at engineering materials and devices at the scale of 1 to 100 nm that allow access to new size-dependent phenomena.[2] It has been realized materials at nanoscale possess a variety of novel physical and chemical properties including the effect of quantum confinement which enables bandgap engineering and tuning of density of states of semiconductors[3], giant magnetoresistance by nanoscale multilayers which can change

in magnetic susceptibility of materials[4], improved strength and stiffness of materials[5], tunable light absorption and fluorescence properties of materials[6, 7], the effect of phonon confinement which can improve the thermoelectric performance of materials[8] and large surface to volume ratio which allows presence of novel interfacial and surface chemistry phenomena.[9]

To harness these exciting properties and explore their possible applications, the study on synthesis and fabrication of nanostructured materials is of great importance. In the past two decades, tremendous efforts have been put on the development of synthesis and fabrication strategies for nanostructured materials with well-defined size, shape, composition and spatial configurations.[10-14] In general, these efforts can be sorted as two categories – top-down and bottom-up approaches. In top-down approaches, bulk materials are broken down into nanoscale units by physical or chemical methods. However, there are limitations in these approaches. When materials fall into nanoscale, conventional top-down synthesis methods such as attrition and milling have little chance to produce materials with well-defined size and shape. The products from these methods also suffers from drawbacks such as existence of contaminates from the milling media. As another class of important materials preparation methods, different types of nanoscale lithography techniques are known to be capable to produce nanostructures with positional control. However, the nanostructures produced by lithography typically have imperfections on surface due to the damage during patterning and resist etching, which may cause significant impact on physical property and surface chemistry of nanostructures.[15] Besides, the next generation lithography techniques such as e-beam

lithography also suffer from problems such as high cost and low throughput.[16] In contrast, bottom-up approaches, typically are chemical synthesis reactions starting from molecular precursors, have better chances to produce nanostructures with well-defined size, shape, crystallinity and surface structures with reasonable cost and throughput. In order to fabricate these nanostructures into desired secondary structures and apply them in real devices, strategies including self-assembly are widely considered and studied.[17, 18] However, there also exists bottle-neck for the development of bottom-up approaches. To date, colloidal synthesis is generally limited to production of nanomaterials with simple structures and there are even fewer mature strategies that can control the assembly process in predictable manners.

In this chapter, I would like to present a general introduction of colloidal nanomaterials from fundamental studies to applications. In **Section 1.2**, the principle of colloidal synthesis of nanocrystals, its recent advances, applications and challenges will be discussed. In **Section 1.3**, development of strategies toward assembly of colloidal nanomaterials and their applications will be discussed. Finally in **Section 1.4**, the scope of this thesis will be presented.

1.2 Colloidal synthesis of nanocrystals

1.2.1 General understandings of colloidal synthesis of nanocrystals

As an important branch of bottom-up nanosynthesis approach, colloidal synthesis has been utilized for production of a widespread of high quality nanoparticles.[10] Although there are different manifestations of colloidal synthesis, they are very similar in

general principles. A typical synthesis always starts from a chemical reaction which can convert the molecular precursors to the monomers of the targeted materials. Reactions include decomposition, reduction, oxidation, metathesis are all possibly to be adopted.[19-21] Then, the monomers will grow into nanoparticles through two processes: nucleation and growth.

The theory of nucleation and growth of colloids were first proposed and extensively studied by La Mer and coworkers (Figure 1.1a).[22, 23] In this theory, at the early stage, the nucleation process is triggered from a supersaturated solution. When the monomer concentration exceeds the saturation threshold, a burst of nucleation will occur and lead to the formation of a large number of nuclei. Rapid growth of these nuclei will then takes place, allow these nuclei grow into larger particles and at the same time significantly reduce the monomer concentration to the level lower than saturation threshold. At the later stage, the growth process further takes place in which the monomers diffuse to the solid-liquid interface and deposit on the nuclei through surface reactions. Finally, the monomers are depleted and the nanoparticles come to their finalized morphology.

Through the analysis of the thermodynamics, it is revealed the process of nanoparticle growth in solution is continuously driven by minimization of the energy of the system (Figure 1.1b).[15, 24, 25] At the stage of nucleation, when a solution is supersaturated, the Gibbs free energy of the solution is high and will be reduced if the solutes are segregated into solid phase from the solution. Equation 1.1 expresses the Gibbs free energy change during the formation of solid phase per unit volume:

$$\Delta G_V = -\frac{kT}{\Omega}\ln\left(\frac{C}{C_0}\right) \qquad (1.1)$$

where C is the concentration of the solute, C_0 is the concentration of the solute at equilibrium, k is the Boltzmann constant, T is the absolute temperature and Ω is the atomic volume. This indicates if the concentration of the solute exceeds its concentration at equilibrium, the Gibbs free energy change of the formation of solid phase becomes negative and nucleation process becomes energy favorable. Assume a formation of a spherical nucleus with a radius of r, the Gibbs free energy change can be described as:

$$\Delta\mu_V = \frac{4}{3}\pi r^3 \Delta G_V \qquad (1.2)$$

However, the formation of solid phase will simultaneously create a solid-liquid interface at the cost of the raise of Gibbs free energy change. In nanocrystal synthesis, this interfacial energy, or surface energy is contributed from the extra energy possessed by the surface atoms resulted from dangling bonds, torture of bonds between the surface atoms, inward force etc. The raise of Gibbs free energy change caused by surface energy of a spherical nucleus with a radius of r can be described as Equation 1.3:

$$\Delta\mu_S = 4\pi r^2 \gamma \qquad (1.3)$$

where γ is the surface energy per unit area. Combining the Gibbs free energy change caused from the volume change of solid and the creation of interface, the total Gibbs free energy change during the formation of a nucleus with a radius of r can be obtained and described as Equation 1.4:

$$\Delta G_{total} = \Delta\mu_V + \Delta\mu_S = \frac{4}{3}\pi r^3 \Delta G_V + 4\pi r^2 \gamma \qquad (1.4)$$

Consider the total Gibbs free energy change ΔG_{total} as a function of the radius of the nucleus r, ΔG_{total} reaches its maxima ΔG^* if the r reaches the critical value r_c at which:

$$\frac{\partial \Delta G_{total}}{\partial r}\Big|_{r=r_c} = 0 = 4\pi r_c^2 \Delta G_V + 8\pi r_c \gamma \quad (1.5)$$

According the relationship in Equation 1.5, r_c and ΔG^* can be described as in Equation 1.6 and 1.7:

$$r_c = -\frac{2\gamma}{\Delta G_V} \quad (1.6)$$

$$\Delta G^* = \frac{16\pi\gamma}{(3\Delta G_V)^2} \quad (1.7)$$

These results clearly demonstrate the formation of nuclei needs to overcome an energy barrier until the nucleus size surpasses a critical value, there after the growth becomes spontaneous.

After the formation of nuclei, the concentration of the monomers dramatically decreases to the level lower than the saturation concentration. At this stage, formation of nuclei is no longer energy favorable and subsequent growth process will become dominant, although it has occurred simultaneously after the formation of nuclei.[15, 26] From the energy point of view, the nuclei are very small in size and have a large surface to volume ratio. Consequently, the system is still not thermodynamically stable due to the large surface energy contributed from the large surface area of nuclei. Hence, growth of the nuclei into larger particles is thermodynamically allowed to reduce the total energy of the system. Typically, the growth process is constituted of two components: diffusion of monomers which supplies materials for growth and surface deposition reaction which

enables incorporation of monomers into the solid particles. After extensive growth by direct deposition of molecular monomers, other coarsening effects such as Ostwald ripening and agglomeration can also happen in order to further reduce the surface energy.[10, 27-30] During the Ostwald ripening process, small particles are consumed and re-deposited on large particles due to the Gibbs-Thomson Effect, which effectively eliminates small particles and reduce the surface energy of the system. In contrast, the growth of particles through agglomeration process is not at the expense of dissolution of small particles, in which many primary particles are associated with one another through physical and chemical interactions. As an example, faceted nanocrystals can be associated and fused into one single crystal through oriented attachment. This process is energetically allowed as the coalesce of the high energy surfaces significantly reduces the surface energy.[29, 30]

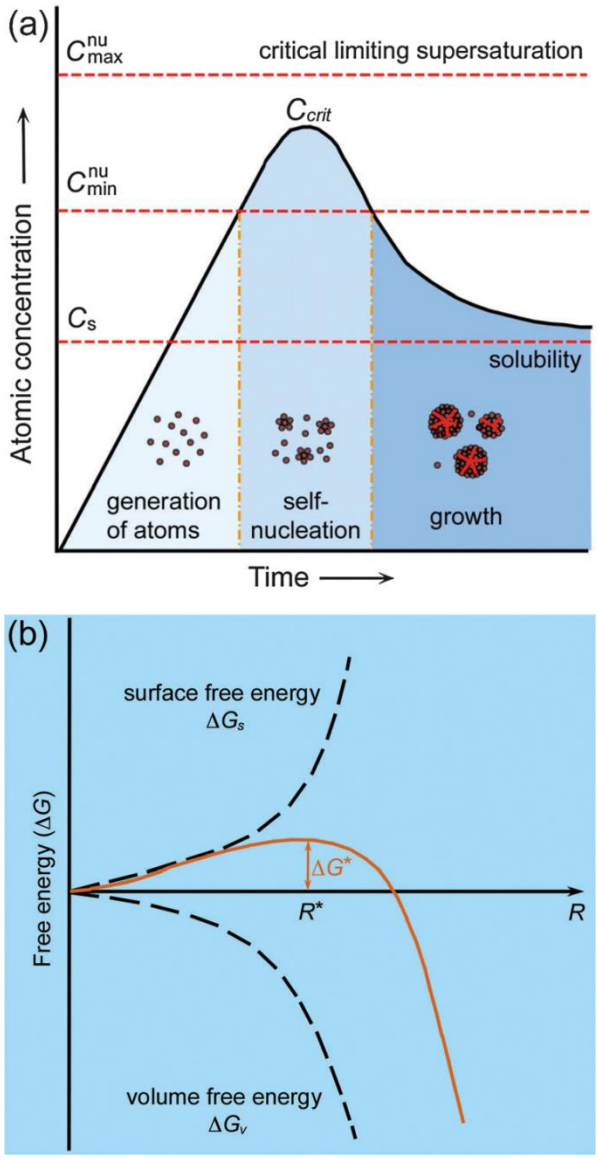

Figure 1.1 (a) The La Mer plot which describes the nucleation and growth of nanoparticles as a function of reaction time. (b) The plot which demonstrate the free Gibbs energy change as a function of the radius of nucleus during the nucleation process. Adapted with permission from ref 23.

1.2.2 Strategies towards size control in colloidal synthesis

Control the size of nanoparticles is very important for synthesis since the physicochemical properties of materials at nanoscale are highly dependent on their size.[3, 31, 32] For example, plasmonic nanoparticles with different sizes will show distinctive optical properties.[32-34] Nanocatalysts such as gold nanoparticles also show a size-dependent activities in carbon monoxide oxidation reaction.[35, 36] In this section, the strategies towards synthesis of uniform nanoparticles with controllable size will be discussed according to the theoretical considerations presented in the last section. Examples of corresponding practical methods will also be introduced.

Theoretically, to obtain nanoparticles with uniform size in classical synthesis, the ideal case is to separate the nucleation and growth processes temporally. Therefore, all the nuclei can be grown under similar conditions and at the end, form nanoparticles with uniform size. In reality, nucleation and growth always have overlapping period and the strategy towards synthesis of monodispersed nanoparticles is to speed up the nucleation rate and shrink the nucleation stage to a very short period of time.[15] The nucleation rate can be described by the Arrhenius formulation:

$$J = A\exp\left(\frac{-E_a}{kT}\right) = \left(\frac{CkT}{3\pi\lambda^3\eta}\right)\exp\left(\frac{-\Delta G^*}{kT}\right) \qquad (1.8)$$

where J is the nucleation rate, A is the Arrhenius constant, E_a is the activation energy. In this case, the activation energy should correspond to the energy barrier ΔG^* described in Equation 1.5 – 1.7 and Figure 1.1b while the Arrhenius constant is directly related to the parameters including the initial monomer concentration C, temperature T, the diameter of

the monomer λ and the viscosity of the solution η. According to this relationship, it can be concluded fast nucleation is favored by high initial monomer concentration, low viscosity of solution, low critical energy barrier and usually high temperature.

During the growth process, theoretically, high concentration of monomers also benefits production of uniform nanoparticles due to the "size focusing" effect (Figure 1.2a).[37-39] According to Equation 1.1 and 1.6, the critical size of the particles increases within the decrease of initial monomer concentration. Therefore, when the monomer concentration is low, the Ostwald ripening becomes the dominant pathway for particle growth since at such conditions, particles with sizes below the critical size may constitute a significant portion of the total particles and these particles tend to be dissolved back to the solution rather than continuously grow into larger particles like the particles larger than the critical size do, which will cause a defocus of size distribution.

Practically, several types of synthesis methods have been developed for production of uniform nanoparticles. The typical case is synthesis of uniform nanoparticles in hot organic solutions with surfactants.[40, 41] This method is capable for synthesis of a variety types of nanocrystals including metal, metal oxide, chalcogenide etc. with good uniformity.[19, 26, 42-44] In these syntheses, appropriate precursors are first chosen to initiate synthesis reactions. Molecules including organometallic compounds are favored as they can rapidly decomposed and produce monomers for nucleation and growth. For example, in the synthesis of cobalt nanoparticles, dicobalt octacarbonyl is preferred in the synthesis as it can be decomposed into metallic cobalt atoms, which serve as the monomers for the nucleation and growth, and carbon monoxide,

which can easily leave the reaction system, at relatively low temperature.[19] In the experiments, the synthesis typically takes place in a hot solution. At elevated temperature, in most cases, the decomposition of precursors can be accelerated and the solution is overwhelmed with supersaturated monomers. Especially in nanocrystal synthesis by hot injection, syntheses can be finished in a time period as short as several seconds with yield of nanocrystals with narrow size distribution right after the injection of precursors as high monomer concentration as well as high temperature allows an instant formation of nuclei and a fast growth process.[19, 40] As an extension to this hot-injection method, by sequential addition of precursors into the solution at different reaction time, uniform nanocrystals with relatively larger sizes can be obtained. The mechanism in this synthesis can be ascribed to the "size focusing" effect.[37-39] With additional injection of precursors, the monomer concentration is maintained at a high level, which can prevent the size defocusing from the Ostwald ripening and continuously increase the size of the particles. This method was first successfully demonstrated in the size-controlled synthesis of cadmium selenide quantum dots and was later extended to other materials.

As discussed early in this section, the ideal strategy towards synthesis of monodispersed nanocrystals is to separate the nucleation and growth to two different stages. In practice, seed-mediated growth methods were employed to realize size control in colloidal synthesis.[45] Different from one-pot synthesis, the principle for seed-mediated growth method is to synthesize uniform nanoparticles by two steps – preparation of seeds and overgrowth on the seeds. In the prior step, nanocrystals typically with small size are first prepared as seeds. The seed preparation is typically according to

the well-established one-pot synthesis methods for uniform nanoparticles. As an example, in gold nanoparticle synthesis, tiny nanoparticles with size less than 5 nm can be prepared as seeds by several methods.[46, 47] In the latter step, subsequent overgrowth of materials on the pre-existing seeds is realized during which the concentration of monomers is kept at a low level in order to minimize nucleation (Figure 1.2b). Typically, the strategies for reducing the monomer concentration include choose of mild reagents and reaction conditions, reduce the concentration or chemical potential of the precursors. As an example, in the synthesis of gold nanospheres by seed-mediated growth, the strong reducing agent, sodium borohydride, which was used in preparation of seeds was substituted by the weak ascorbic acid in the overgrowth process. Iodide ions were also introduced to complex with the typical gold precursor, chloroauric acid. Therefore, the reduction potential of the gold precursor was significantly reduced and allowed a high precursor concentration in the solution while kept the monomer concentration at a low level during the synthesis. This strategy successfully enabled seed-mediated growth of gold and silver nanoparticles in a large size range within one round of growth.[33, 34] Since the low concentration of monomers also favors size defocusing through the Ostwald ripening, in growth step, the synthesis is typically under a mild condition, such as at a reduced temperature, compared to the classical synthesis conditions. The seed-mediated growth strategy has been successfully realized in synthesis of different types of nanocrystals, majorly noble metals as well as several types of metal oxides and chalcogenides. [47-50]

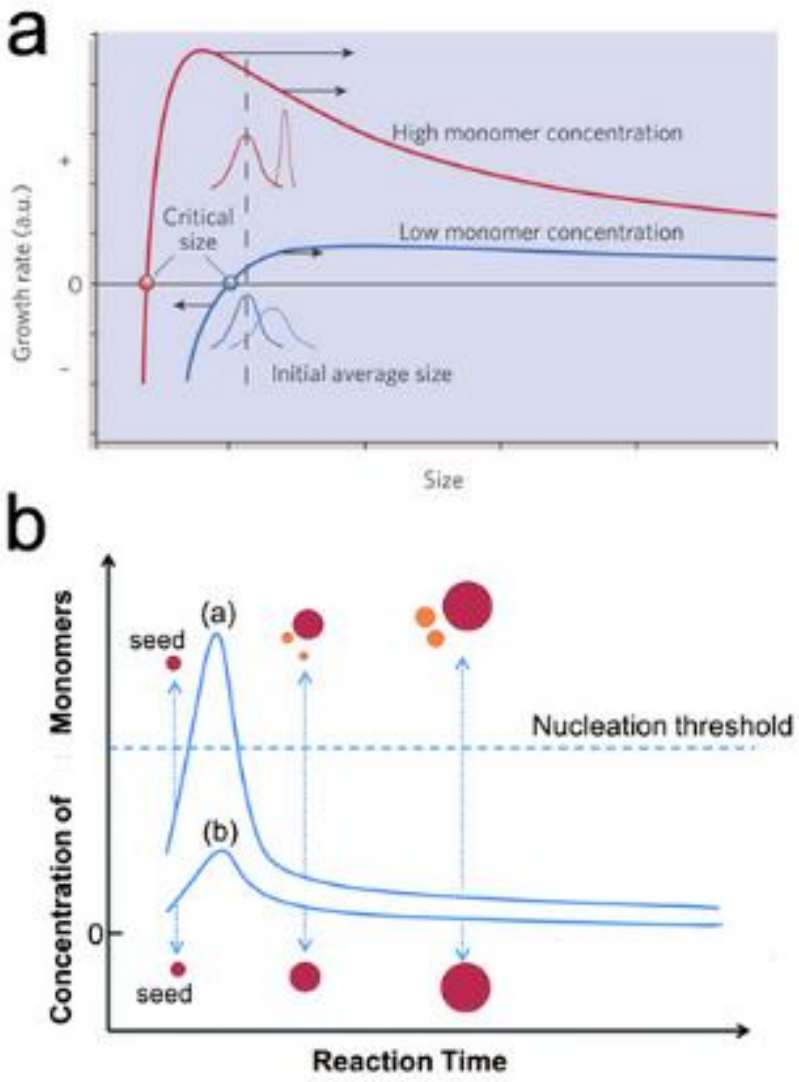

Figure 1.2 Schematic illustration of size control of nanocrystals by (a) size focusing and (b) seed-mediated growth. Adapted with permission from ref. 10 and ref. 33.

1.2.3 Strategies toward shape control in colloidal synthesis

The physiochemical properties of nanoparticles are also dependent on their shapes. For instance, anisotropic noble metal nanoparticles such as gold nanorods and silver nanoplates have distinctive optical properties from isotropic spherical particles due to the evolution of new plasmon resonance modes.[51, 52] Some metal and metal oxide nanocrystals with specific shape showed improved catalytic performance due to the expose of specific facets.[53, 54] As another example, some anisotropic semiconductor nanocrystals also show different photoluminescence properties from their spherical analogues.[55] Therefore, it is highly demanding to develop robust methods for shape control synthesis of nanocrystals.

In colloidal synthesis, recent developed methods have allowed effective synthesis of nanoparticles with shape control. Imagine if the growth of nanoparticle is infinitely slow, the final shape of the particle should be in its most thermodynamically stable form. In nanocrystal synthesis, the most thermodynamically stable structure should be its Wulff shape.[12, 56] The morphology of the nanocrystals can then be modified into different shapes by control the shape of the nuclei (or the seeds in seed-mediated growth) and the thermodynamics and kinetics of the growth process.

From the energy point of view, an efficient way to control the shape of nanocrystals is to add ligands which can change the surface energy. Typically, the binding of ligands on the nanocrystals has selectivity depending on the facets, which effectively lowers the surface energy of specific facets and results in a shape-directing effect during the nanocrystal growth.[11, 57, 58] Besides, the growth kinetics also has

significant effect on the shape control of nanocrystals. [10-12, 59, 60] At a low growth rate, although still in faceted shape, nanocrystals are typically in low aspect ratio after the synthesis. In contrast, at high growth rate, nanocrystals with higher aspect ratio can be obtained. This is most likely due to the elimination of high energy facets during the fast growth of nanocrystals, leaving the nanocrystals terminated by facets with slower growth rate. The elimination of fast growing facets can be understood as at high growth rate, the deposition of monomers on the high energy facets can be so fast that a second layer of atoms may have been capped on the first layer even the first layer may have not covered the original facet. In experiments, the choice of ligands is mostly empirical as there are no reliable methods to determine the exact binding energy between the ligands and the nanocrystal surface. One of the most classic examples for shape control nanocrystals synthesis by choosing appropriate ligands and kinetic control is the synthesis of cadmium chalcogenide nanocrystals with different shapes.[11, 61] In these syntheses, alkyl phosphoric acids were together added into the reaction solution with trioctylphosphine oxide, which is a classic surfactant for spherical CdSe quantum dot synthesis. As the results, cadmium chalcogenide nanorods were produced and it was revealed the phosphoric acids can selectively bind on the side facets of the nanorods. By manipulation of the reaction kinetics by methods such as multiple precursor injection, which can maintain the monomer concentration to be at a high level, the aspect ratio of the nanorods can be tuned. Meanwhile, a combination of manipulation on the phosphoric acids and the reaction kinetics can further allow the production of CdSe nanocrystals with higher complexity such as tetrapods and dendrite tetrapods.

Seed-mediated growth synthesis is also well-known for its capability in shape control of nanocrystals.[20, 48, 62, 63] Compare with one-pot synthesis, in addition to choice of ligands and manipulation of growth kinetics, the structure of the seeds can also direct shape control of the final nanocrystals since the overgrowth process need to accommodate with the shape and facets of the seeds. Although the structure of the seeds should have been predominantly determined by their crystal structure, it may possibly varies from one to another since there may exist defects in the structures such as twinning and stacking faults which may significantly affect the final morphology of nanocrystals after growth.[12, 64, 65] For example, in fcc metal nanocrystal synthesis by using seed-mediated growth method, the use of single crystalline seeds typically yield nanocrystals with polyhedron shape such as cube and octahedron. In comparison, if the seeds contain twinning or stacking faults, the nanocrystal may eventually evolved to the shape of rods or plates.[12, 66] Therefore, to ensure nanocrystals adopt uniform shapes after growth, it is important to engineer the shape of the seeds. In noble metal nanocrystal synthesis by seed-mediated growth, it has been demonstrated oxidative etching is an effective method to control the structure of the seeds.[20, 67] In this process, seeds with different structures will transform to a uniform shape, typically in energetically stable configuration, since the reactive seeds can be dissolved and reformed when etchants such as a combination of ligand and oxidants present in solution. Based on this seed refinement, nanocrystals with uniform shape can be obtained. In the case of silver nanoplates synthesis by seed-mediated growth, addition of hydrogen peroxide in the synthesis, together with citrate and polyvinylpyrrolidone which were ligands proven to be

effectively bind on (111) and (100) facets respectively, can effectively produce silver seeds with planner twinning by selectively etching those without planner twinning. By further growth on these seeds with the presence of ligands, 100% yield of silver nanoplates can be obtained.[20] Since seed-mediated growth separated the synthesis into multiple steps, it also provides flexibility for synthesis of nanocrystals with complex structures as the reaction conditions at each individual step can be separately controlled.

1.2.4 Template synthesis – an extension

The above mentioned colloidal syntheses have readily enabled production of different nanoparticles including metals, metal oxides and other semiconductors with well-defined size and shape. There are also approaches extend these syntheses one step further, to produce uniform nanostructures that cannot be obtain through direct synthesis. Different types of template synthesis are good examples in this case.

The general idea of template synthesis of nanoparticles in solution is to take pre-existing materials as templates and perform colloidal synthesis with the restriction from these templates.[68] The templates can be classified into two categories: physical and chemical templates. Physical templates majorly act as shape directing agents in colloidal synthesis. The requirements for physical templates typically include size and shape uniformity, cost-effectiveness and easiness to be removed after synthesis. Both hard and soft materials such as silica beads, shells or molecular micelles and vesicles can be adopted.[69-73] As an example, if a gold nanoparticle seed is encapsulated in a tubular silica template, the gold can be grown into nanorods as the shape is growth is restricted by the silica.[70] The advantage of this method is that it can be extended for synthesis of

several other metal nanorods which typically cannot be obtained from direct synthesis. The removal of the silica template is also convenient by simple base etching. In the case of chemical templating, the template nanostructures not only act as shape directing agents but also as the precursors for the products. The synthesis by chemical templating typically involves chemical transformation of template nanocrystals in the forms including ion exchange and galvanic replacement.[74-76] Synthesis via ion exchange enables production of compound nanocrystals and their derivatives which may not be easy to be produced by direct synthesis. In comparison, templating through galvanic replacement typically occurred in synthesis of metal nanostructures. The shape of the products synthesized through galvanic replacement is highly dependent on which of the template, and typically shows more complex structure such as cages, boxes and frames due to the volume change. By adjusting the reaction conditions, nanostructures with different compositions from pure metal to alloys can readily be produced in controlled manners.[76-78]

1.2.5 Challenges in Future Applications

Nanocrystals produced by colloidal synthesis have already demonstrated applications in various fields including catalysts, sensing, medicines etc.[79-82] There still exist challenges in the synthesis for the future development of colloidal nanocrystal-based applications. For example, the organic ligands which are effective tools for control the size and shape of the nanocrystals become noxious when the nanocrystals are used for applications such as catalysis and electronics since they may block the access of reagents and significantly affect the electron transport. Robust ligand exchange or removal

methods are highly demanded for these applications.[83, 84] To date, the yields of most of the delicate synthesis are still in the level of milligram scale, which also potentially limits the use of the colloidal nanocrystals in industry. Therefore, development of methods for scaling up the synthesis has also become a hot-spot in recent researches on colloidal synthesis. Strategies such as synthesis by flow reactors have been successfully demonstrated to be capable for production of high quality nanocrystals.[85, 86]

The major challenge for application of colloidal nanocrystals, however, is to develop reliable methods to integrate them into more complex structures and apply them in devices. The approaches towards integration of nanoparticles are different strategies towards self-assembly of colloidal nanoparticles, which will be discussed in the next section.

1.3 Self-assembly of colloidal nanoparticles

1.3.1 General introduction

Self-assembly refers to the process in which components (can range from microscopic molecules to macroscopic objects) spontaneously form ordered aggregates.[17, 18] In order to integrate colloidal nanoparticles which are produced through bottom-up synthesis methods into complex structures for further applications, self-assembly processes are preferred as they have many advantages over top-down fabrication methods. First, top-down methods have size-limitations. To date, in semiconductor industry, technology node has just passed 14 nm node and fabrication of devices below this size is still challenging.[87] However, the materials with size range

below 10 nm are important as they located in the size range where novel properties such as quantum confinement effect can evolve. Besides, the fabrication of ordered nanostructure assemblies typically is not cost-effective since it requires the use of expensive instruments and is difficult to scale up.[16] In contrast, self-assembly process can be achieved in the size range as small as molecular level. Meanwhile, the process is spontaneous and does not require high energy input which is capable to scale up with a low cost. [17] In addition, another interesting property for assembly of colloidal nanoparticles is the evolution of collective property of the materials which does not exist in isolated nanoparticles.[88] Therefore, by control of the assembly behavior of the nanoparticles, physical and chemical properties including optical, magnetic, electric properties can be tunable.

The most important issue which need to be considered for self-assembly process is the interactions among the assembly building blocks. Self-assembly occurs when attractive and repulsive interactions are balanced.[17] Either attractions or repulsions is overwhelmed than the other will cause permanent aggregation at first place or prevent the aggregation from happening. Only the interactions are balanced, the assembly process will be allowed to happen with the presence of reversibility and enable the aggregates self-adjust to an ordered structure (Figure 1.3). This indicates the environment for self-assembly process typically favors in solutions or at the interfaces since these environments can ensure the motion of the building blocks. Meanwhile, the interactions should be weak, non-covalent and the scale should be comparable to thermal fluctuations.

On molecular level, self-assembly has been realized in many different manifestations such as self-assembled monolayers[89], block copolymer assemblies[90], ionic layer-by-layer assemblies[91] and DNA-based assemblies[92]. These assemblies are enabled by different types of interactions. Self-assembled monolayers take advantage of steric interactions which direct the packing of molecules into ordered monolayer structures. Block copolymers can be assembled into ordered structures such as different shaped micelles and bicontinuous structure due to the hydrophobic interactions originated from their amphiphilicity. Layer-by-layer assemblies are allowed by interactions originated from the charges on different poly-ions which served as building blocks for these assemblies. By successive stacking of layers of poly-ions with opposite charges, assembly of poly-ions with controlled thickness, composition and ionic properties can be achieved. In the case of DNA-based assembly, the complementary nature of DNA base pairs provides programmable recognition codes for construction of assembly structures.

In self-assembly of nanoscale colloidal particles, the assembly is governed by interactions among the nanostructures, from both the cores and surfaces. In this case, the assembly behavior is majorly manipulated by engineering the nanoparticle surface such as surface modification of functional molecules and introduce interactions in molecular assemblies. In the next sub-section, nanoscale forces both originated from the nature of colloidal nanoparticles and the specific molecules grafted to the nanostructure surface will be discussed.

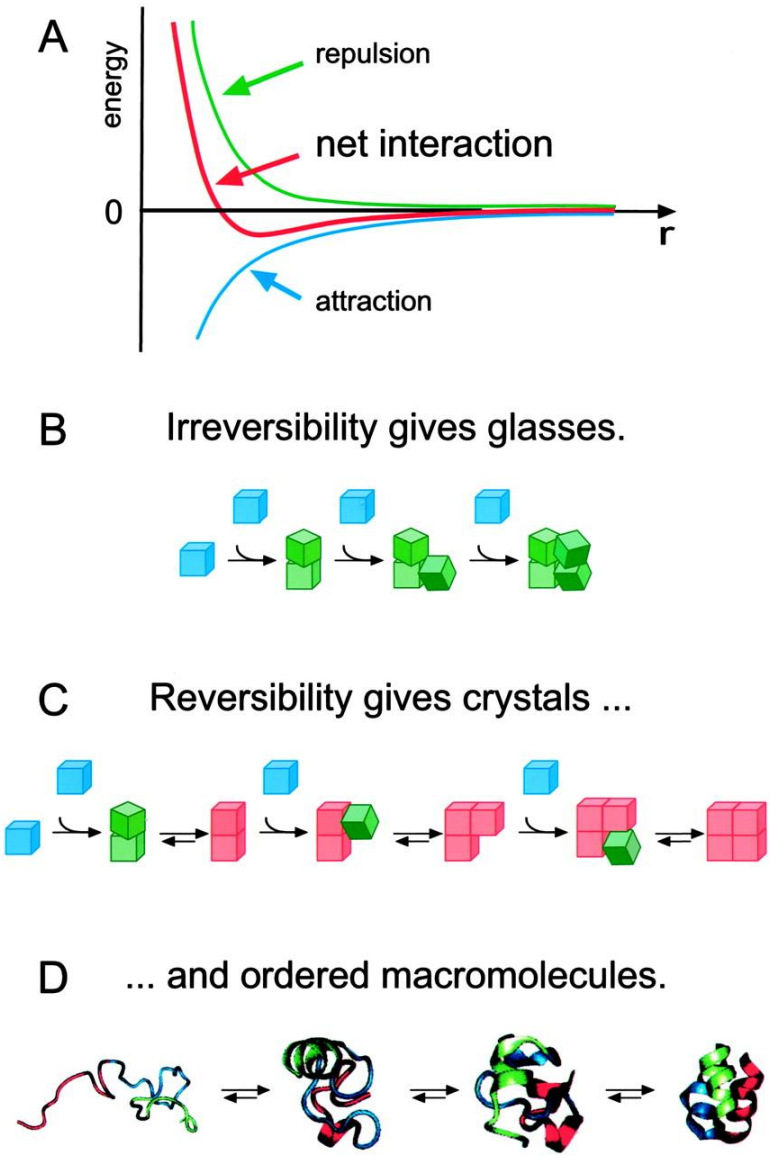

Figure 1.3 Schematic illustration of ideal self-assembly process. (a) the interaction energy requirement: a net attraction at equilibrium separation, overall a balance between attraction and repulsion. (b) irreversible assembly results in random aggregation. (c, d) reversible assembly enables building blocks self-adjust to ordered structures. Reprinted from ref. 18.

1.3.2 Colloidal interactions

Understanding of nanoscale forces is important for control the assembly behaviors of colloidal nanoparticles as they govern the motion of the colloidal nanoparticles and determined the thermodynamics of assembly structures.[93-96] These forces can be either attractive or repulsive, and may have different magnitudes and length scales. Their magnitude and length scales reflect their ability to assemble the nanostructures as they determined the interaction potential among the colloidal nanoparticles and also the ability to direct nanoparticle building blocks into ordered structures. Typically, a long-range attraction combined with a short-range repulsion favors the assembly as this combination is able to create an interaction potential well at a relatively short interparticle distance. A classic example is the Lennard-Jones potential which is used for description of interactions between spherical atoms:

$$V_{LJ} = 4\varepsilon\left[\left(\frac{\sigma}{r}\right)^{12} - \left(\frac{\sigma}{r}\right)^{6}\right] = \varepsilon\left[\left(\frac{r_m}{r}\right)^{12} - \left(\frac{r_m}{r}\right)^{6}\right] \qquad (1.9)$$

where ε is the depth of the potential well, σ is the finite-distance at which the interparticle potential is 0 and r_m is the finite distance at which the interparticle potential reaches minimum. In this case, the attractive van der Waals forces are in the length scale of r^{-6} while the length scale for repulsive exchange interactions is r^{-12}.[94]

In the past century, different types of colloidal interactions have been revealed, studied and been used for controlling the assembly of colloidal nanoparticles. As early as in 1920s, scientists have put efforts to understand the aggregation and dispersion properties of colloids in solution.[97] A remarkable achievement was the development of

the Derjaguin-Landau-Verwey-Overbeek (DLVO) theory in which the two fundamental interactions among colloids: van der Waals and electrostatic interactions were understood and quantitatively studied.

Van der Waals interactions are generally attractive in nature and are originated from the electromagnetic fluctuations caused from the random movement of the charges inside the materials and they are universally existed.[93, 94] They are consisted of several different types of forces including dipole-dipole force (Keesom force), which is originated from two permanent dipoles, induced-dipole force (Debye force), which is originated from a permanent dipole and an induced dipole and dispersion force, which is contributed from two instantaneously induced dipoles. The magnitude of van der Waals interactions typically range from several kT to hundreds of kT and the length scale is r^{-6}. To quantitatively analyze the van der Waals interactions between two colloidal nanoparticles, several approaches have been demonstrated. The most straightforward approach was known as Hamaker integral approximation[98]. The basic idea of this method is to pair-wise integrate the van der Waals interactions of every atom in the two colloidal particles. As an example, the van der Waals interaction energy between two spheres with radius of a_1, a_2 and interparticle center-to-center distance of r can be described as:

$$V_{vdW} = \frac{A}{3}\left[\frac{a_1 a_2}{r^2-(a_1+a_2)^2} + \frac{a_1 a_2}{r^2-(a_1-a_2)^2} + \frac{1}{2}\ln\left(\frac{r^2-(a_1+a_2)^2}{r^2+(a_1-a_2)^2}\right)\right] \quad (1.10)$$

in which A is the Hamaker coefficient which is determined by the composition of the interacting particles and their surrounding media. Theoretically, this method can be

applied to assess the van der Waals interactions between colloidal particles with arbitrary shape. However, there are several factors such as many-body effect and retardation effect, which also have effect on the van der Waals interactions, haven't been taken into considerations. Several other approaches such as the Dzyaloshinskii–Lifshitz–Pitaevskii (DLP) theory[99] and discrete coupled-dipole method (CDM)[100] have been developed to take the above-mentioned factors into considerations. Compare the Hamaker integral approximation with the DLP theory and CDM, the former is the mathematically simplest and also reliable. Therefore, practically, the Hamaker integral approximation is still the most widely used method to assess van der Waals interactions in colloidal systems.

Electrostatic interactions are originated from the interactions among the permanent charges on the colloids. They can be either attractive or repulsive depending on the nature of the charges on the interacting colloidal particles. Unlike van der Waals interactions which are typically "rigid" as the whole particle contributes to the interactions, electrostatic interactions are much easier to be manipulated as they rely more on the surfaces. They can be anisotropic if the surface charge distribution is not even.[101] They are also sensitive to the environment as factors such as ionic strength and pH have significant effect on tuning the surface charge density.[102] Quantitatively, the electrostatic interactions among colloidal particles can be described based on the diffuse electric double layer (EDL) model.[103, 104] In the EDL model, the net surface charge is contributed from a permanent charge layer which is bind the colloidal surface and a diffuse counter-ion layer. The distribution of the diffuse counter-ion layer highly dominates the net charge density on the colloidal particles and affects the electrostatic

potential of the particles, which can further affect the electrostatic interactions among particles. Typically, the electrostatic potential of an electric double layer system can be described by the Poisson-Boltzmann Equation and the electrostatic potential around a charged surface can be described as:

$$\psi = \psi_0 \cdot e^{-\kappa x} \quad (1.11)$$

where ψ_0 is the potential on the surface, x is the distance to the surface and κ is the inversion of the decay length (or Debye length) which is affected by the bulk concentration of the counter-ions c_0, dielectric constant of the solvent ε and temperature T. When two charged colloidal particle interact with each other, the electrostatic interaction potential energy can be derived and described as[97]:

$$V_{elec} = \frac{Q_1 Q_2}{4\pi\varepsilon_0\varepsilon(1+\kappa a_1)(1+\kappa a_2)} \cdot \frac{\exp[-\kappa(r-a_1-a_2)]}{r} \quad (1.13)$$

Van der Waals attraction and electric static repulsion are classified as DLVO interactions as the combination of effects from both interactions are used in the DLVO theory to understand the dispersion and aggregation behaviors of colloidal particles in solution. This understanding also pointed out the colloidal aggregation behavior can be controlled by change of ionic strength, solvent and temperature, which are expected to benefit for control of the nanoparticle assembly process.

Apart from DLVO interactions, there also exist non-DLVO interactions such as solvation force[105, 106], hydration force[107] and hydrophobic interactions[108] among colloidal particles which typically originated from the interfacial phenomena that the DLVO theory has not considered. These interactions are typically in short range and are

not capable to direct the assembly behavior. However, they are crucial to the reversibility of the assembly. Whether the short-range repulsions that colloidal particles experiences when they come to very close with each other can counter the attractions or not is the key to determine the reversibility of the assembly process.

In addition, by control of both the properties of the colloidal core and surface modifications. Additional interactions can be introduced for control the assembly process. Colloidal cores consist of specific materials such as metal chalcogenides or magnetic metal or metal oxides possess intrinsic electric dipole moment[109, 110] or magnetic dipole moment[111, 112] which can direct the assembly under appropriate conditions. Surface modification on colloidal particles which is typically realized by coordination or electrostatic adsorption of functional molecules can also bring in various additional interactions including molecular dipole interactions[113], specific recognition interaction from coordination or hydrogen bonding[114-116], steric repulsion between polymer brushes[117], attractive hydrophobic interactions among the alkyl chains[118] etc. In addition to interactions that enable self-assembly by taking advantage of the reduce of energy, other forces which can favors the ordering of the assembly driven by entropy change such as depletion force can also be considered for directing self-assembly of nanoparticles.[119, 120]

1.3.3 Self-assembly of nanoparticles at different dimensions

In this sub-section, examples for assembly of nanoparticles in one, two and three dimensions realized by control of a variety of colloidal interactions will be introduced. To obtain high quality assembly structures, in the assembly process, attractions and

repulsions are balanced, while long range packing forces are needed to direct the assembly and short range repulsion forces are needed to ensure reversibility of the assembly.

In order to assemble nanostructures into one-dimensional assembly, anisotropic interparticle interactions originated from electric and magnetic dipoles are employed to drive the assembly.[109, 121] For example, metal chalcogenides nanocrystals are known to have relative large permanent electric dipole. When peeling off the ligands on the nanocrystals, which provide repulsion forces for the nanocrystals, these nanocrystals can be assembled into one-dimensional chains driven by the dipole-dipole interactions.[109] Ferromagnetic nanoparticles can spontaneously assembled into one-dimensional chain or ring structures directed by magnetic dipole-dipole interactions.[121] Anisotropy in self-assembly can also be originated from the shape anisotropy or the anisotropy of chemical property of the assembly building blocks.[122] For example, under appropriate conditions, gold nanoplates preferred to assemble into face-to-face one-dimensional structure by depletion force as the face-to-face structure is energy favorable.[120] In an example for one-dimensional assembly of nanostructure induced by chemical anisotropy, faceted gold nanorods with special functionalization at the tip are responsible to assemble these gold nanorods into chain structure.[123] Besides, one-dimensional assemblies can also be achieved by direction of external field.[96, 124, 125] As an example, superparamagnetic nanoparticles can be assembled into one-dimensional nanostructures with orientation control by apply external magnetic field.[111, 125] When superparamagnetic nanoparticles are experienced with external magnetic field, magnetic

dipole moment will be induced and result in evolution of dipole-dipole interactions and field-dipole interactions in which the longer range field-dipole interaction is the packing force for the assembly. At the same time, repulsion forces, in most cases are electrostatic repulsion, provide counter forces to balance the interactions. The packing force can be tuned by control the external field strength and the structure such as the interparticle distance of the one-dimensional assembly becomes tunable and this property enable these assemblies applied for magnetic responsive photonic structures.

When nanoparticles experienced with additional interactions from substrate or interfaces to their interactions in solution, two-dimensional or three-dimensional assembly of colloidal nanostructures can be achieved.[126-129] To assemble colloidal nanoparticles into two-dimensional arrays, the surface of the nanostructures can be appropriately modified in order to allow them to preferentially stay at the interfaces including air-liquid and liquid-liquid interfaces.[126, 127] These assemblies can also be transferred to substrates by various methods for applications. When substrates are involved in the assembly process, other interactions such as capillary force during the evaporation can also direct the nanostructures to assemble into two-dimensional or three-dimensional colloidal crystals.[128, 129] In some early endeavors, these types of assembly are realized by mono-component sub-micron colloidal spheres and were demonstrated for applications such as photonic crystals.[130] Recently, two and three-dimensional assembly of colloidal nanocrystals with different sizes, shapes and multiple components have been realized by delicately control of the interparticle forces as well as the directing agent such as interfaces and substrates.[131] These assembly also have

showed potential to be applied in new generation of nanoscale devices such as field-effect transistors.[132]

1.4 The Scope of This Thesis

In the last two sections, the two fundamental issues about nanotechnology from bottom-up: synthesis and self-assembly have been discussed. Based on these theoretical understandings, in this thesis, case studies for both colloidal synthesis and self-assembly of nanomaterials will be presented. From the materials aspect, the focus of this thesis will be research on synthesis, self-assembly and applications of anatase TiO_2 nanocrystals and gold nanoparticles. Then, the thesis will be concluded by an outlook and plans for future work.

In **Chapter 2**, a systematic study on design and realization of shape control synthesis of anatase TiO_2 nanocrystals with various structures and their applications in photocatalysis will be discussed. Synthesis of anatase TiO_2 nanocrystals with controllable simple faceted structures will first be demonstrated by employing appropriate shape directing agent. In the next step, a general strategy to synthesis anatase TiO_2 nanocrystals with complex core-antenna structure will be demonstrated. In this study, core-antenna nanocrystals were synthesized by adopting seed-mediated growth method. In the synthesis, different faceted anatase TiO_2 nanocrystals were used as seeds. By careful control the growth condition, anatase TiO_2 nanorod antenna can be epitaxial grown on the seed nanocrystals with defined orientation. The morphology of the nanorod antennas including the thickness and length can further be controlled. In the last part of this chapter,

the photocatalytic activity of anatase TiO_2 nanocrystals with diverse morphology will be investigated.

In **Chapter 3**, the focus will be on design and realization of reversible assembly of charged gold nanoparticles and its applications. Theoretical considerations on how to realize reversible assembly of charged gold nanoparticles in solution will first be discussed. Then, experimental realization of the reversible assembly by change of temperature will be presented. In this case, the thermodynamics as well as the kinetics of the reversible assembly will be discussed in details. Finally, the reversibly assembled gold nanoparticle chains were demonstrated to be able to be transferred in to polymer films and the gold nanoparticle chain-polymer composite film showed stress responsive optical property due to the force disassembly of gold nanoparticle chains and can be applied as colorimetric pressure sensor.

Finally, in the **Chapter 4**, I will give a brief summary of the results presented in this thesis. An outlook for this research field will be briefly discussed as follows. Finally, a detailed plan for future work based on the current results will also be demonstrated.

Chapter 2

Shape Control Synthesis of Anatase TiO_2 Nanocrystals and Their Application in Photocatalysis

2.1 Introduction

In history, TiO_2 are widely used as pigments and also in sunscreens, ointment and toothpastes as they are chemically stable and the toxicity is low.[133] Their unique photoactive property was not realized until in 1972, Honda et al. discovered TiO_2 to be active for photocatalytic water splitting under UV irradiation.[134] TiO_2 is photocatalytic active since it is a wide band gap semiconductor and under UV irradiation, hole-electron charge separation can occur once it absorbs photons. Holes and electron then migrate to the surface and react with the chemical species at the interface by redox reactions (Figure 2.1c). Since then, tremendous efforts have been put on the study of its photoactive properties and how to use it in relevant applications such as photocatalysis and photovoltaics.[54, 135-141] In these studies, it is revealed that engineering TiO_2 materials into nanoscale with well-defined structure is desired and may benefit relevant applications as the property of TiO_2 becomes different from the bulk.

Recently, it has been realized that the structural factors of the TiO_2 nanomaterials including size, shape, crystallinity, hierarchy have significant effects on the performance in applications. For instance, it has been realized the photocatalytic activity of anatase TiO_2 crystals can be controlled by tuning the exposing facets[54, 142-147], while in our

group, we have revealed TiO_2 nanoshells can possess superior photocatalytic activity only when they have optimal crystallinity and surface area.[136, 137] As another example, Zheng et al. demonstrated TiO_2 nanorods with hierarchical nanowhiskers have better performance as electrodes for photoelectrochemical reactions.[148] There also exist examples that the performance of photovoltaic devices can be improved by tuning the shape and hierarchy of TiO_2 nanostructures.[140, 149-153] Therefore, it is highly desirable to develop synthetic methodologies for TiO_2 nanostructures in highly controllable manners.

Enormous methods have been utilized to produce and control the TiO_2 nanostructures. In colloidal synthesis, the most commonly used method is sol-gel synthesis method in which titanium molecular compounds can be converted to TiO_2 by a hydrolysis and condensation reaction.[154] Typically, classical sol-gel synthesis produces amorphous TiO_2 which are typically not favored for photocatalysis or photovoltaic applications. To overcome this drawback, crystalline TiO_2 materials can be obtained by either post-calcination of the amorphous TiO_2 materials or use extended sol-gel synthesis methods such as sol-gel synthesis at high temperature in organic solvents or at solvothermal conditions.[58, 155, 156] To accommodate the specific application, surface modification of the as-synthesized TiO_2 nanocrystalline materials may also be needed.

In particular for photocatalysis applications, anatase TiO_2 nanocrystals are more preferred than other polymorphs of TiO_2. Compared to rutile phase TiO_2, although anatase TiO_2 is thermodynamically metastable and have a relatively larger band gap (~3.2 eV for anatase and ~3.0 eV for rutile), it is favored in photocatalysis since the hole-

electron recombination rate is lower and at mean time, its surface shows better adsorptive affinity to reactive species such as organic molecules to be degraded.[157-159] As has been introduced, the size, shape and crystallinity of the nanocrystals have significant effect on the photocatalytic performance, colloidal synthesis methods which are capable to realize size, shape and crystallinity control are highly demanded. Anatase TiO_2 adopt a tetragonal lattice and under thermodynamic equilibrium, it adopts its Wulff shape which is truncated octahedron and the crystal is enclosed by two (001) facets and eight (101) facets (Figure 2.1b).[133, 160] In order to realize size and shape control in anatase TiO_2 nanocrystal, in the pre-existing synthesis methods, efforts have been put in developing methods for control of both thermodynamics and kinetics in the synthesis. For example, incorporation of fluorine in the nanocrystal synthesis is known to be effective to expand the high energy (001) facets.[54, 161] By controlling the kinetics in high temperature pyrolysis reactions, rod-shaped anatase TiO_2 nanocrystals can be obtained.[58, 162, 163] Apart from the above-mentioned examples, there also exists other types of high quality anatase TiO_2 nanocrystals including rhombic nanocrystals, nanoplates etc.[161, 164] However, most of the methods are still empirical and not capable to programmable produce nanocrystals in predictable manners. Meanwhile, empirical methods also limit their extension to produce nanocrystals with higher structural complexity, which is potentially beneficial for improving the photocatalytic performance. Thus, development of a robust method for rational synthesis of anatase TiO_2 nanocrystals with predictable and complex structures is still required.

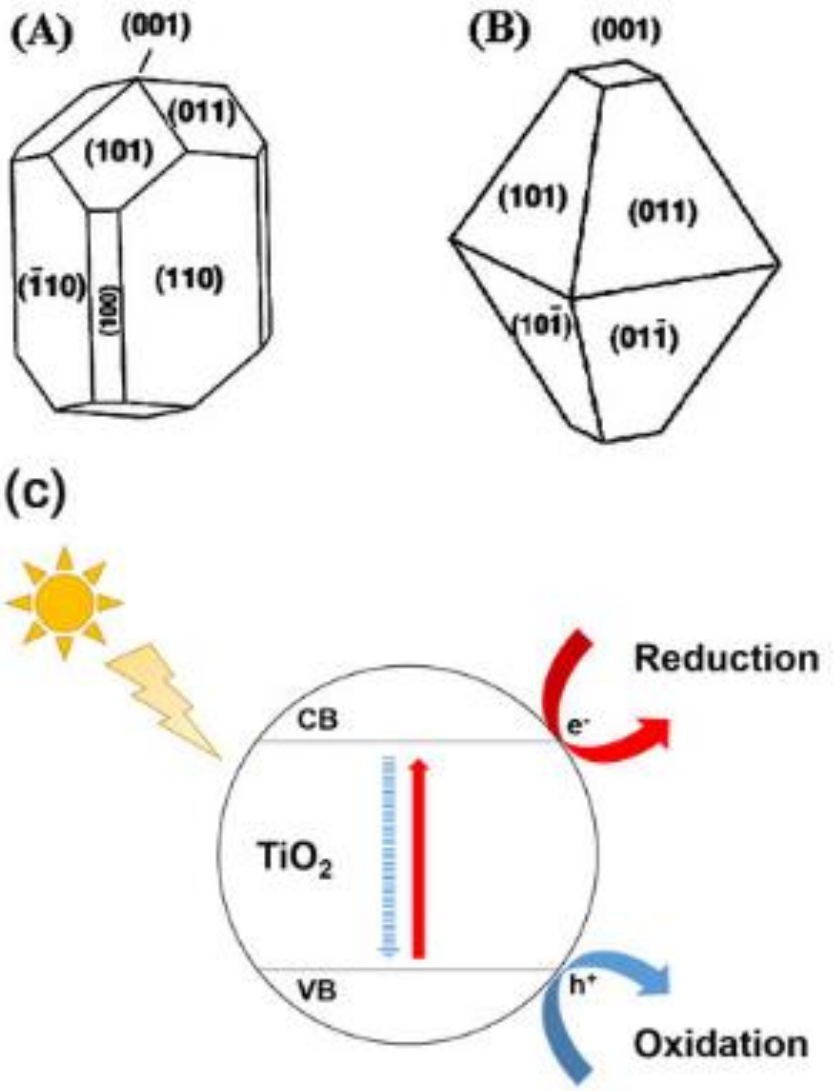

Figure 2.1 (a, b) Schematic illustrations of the Wulff shapes of rutile phase (a) and anatase phase (b) titanium dioxide. Adapted with permission from ref. 160. (c) Schematic illustration of the principle of photocatalytic reactions by using titanium dioxide as catalyst.

In this chapter, I will present a systematic study on design and synthesis of anatase TiO_2 nanocrystals with highly predictable complex structures. A systematic study on shape control of anatase TiO_2 nanocrystals with well-defined simple morphology by using fluorine ions as shape directing agent will first be discussed in **Section 2.3**. Then in **Section 2.4**, a study of design and synthesis of anatase TiO_2 nanocrystals with complex hierarchical structures by seed-mediated growth method will be presented. The photocatalytic performance of anatase TiO_2 nanocrystals with different shapes including those with complex structures is studied and presented in **Section 2.5**. Finally, this chapter will be concluded with a brief summary in **Section 2.6**.

2.2 Experimental Methods

2.2.1 Chemicals

Titanium butoxide 99% (TBOT), titanium isoproxide 98% (TTIP), titanium fluoride 99% (TiF_4), 1-octadecene 90% (ODE) were purchased from Acros. Sodium fluoride (NaF) was purchased from Fisher, and oleic acid 90% (OA), benzoic acid 99.5% (BA), oleylamine 70% (OAm), anhydrous toluene 99.8 %, tetramethyammonium hydroxide solution 25 wt. % in H_2O (TMAH) were purchased from Sigma-Aldrich. 1-hexadecanol 98% (1-HDOL) was purchased from Alfa Aesar. 200-proof ethanol was purchased from Decon Laboratories, Inc. All chemicals were used as purchased without further purification.

2.2.2 Syntheses

Unless stated, all the syntheses were carried out under standard Schlenk line operation.

Anatase TiO_2 nanorods

Anatase TiO_2 nanorods were synthesized by a heat-up method. In the synthesis, 22 mL of OA was vented at 150 ℃ to remove the low boiling point impurities. After cooling down to room temperature, 3 mL of TBOT was added into the purified OA. The mixture was then heated to 300 ℃ and kept for 3 hours. After the reaction mixture was cooled down, the nanorods were isolated by addition of 200-proof ethanol (1:1) and centrifugation (11,000 rpm/5 min). The precipitates were then repeatedly washed by first re-dispersed in 15 mL of anhydrous toluene, then precipitation by addition of 200-proof ethanol (1:1) and centrifugation (11,000 rpm/5 min) for two times. The nanorods were finally dispersed in 15 mL of anhydrous toluene.

Transformation of anatase TiO_2 nanorods into octahedral bipyramidal nanocrystals

Anatase TiO_2 nanorods were first synthesized by using the same chemicals and heating conditions as described above. After the reaction mixture was maintained at 300 ℃ for 3 hours, 2 mL of a mixture of purified OA and 0.105g NaF was injected to the reaction mixture. The reaction was then raised to 320 ℃ and kept for a certain period of time to ensure transformation. After cooling down to room temperature, the products were washed and collected by the same procedures as described for nanorods synthesis except change the centrifugation speed from 11,000 rpm to 10,000 rpm.

One-pot synthesis of truncated octahedral bipyramidal (TOB-shaped) nanocrystals

24 mL of purified OA, 3 mL of TBOT and 0.105g of NaF were first added into a three-neck flask and mixed by gentle magnetic stirring at room temperature. Simultaneously, gentle flow of N_2 was introduced to purge the reaction mixture for 30 min. Then the reaction mixture was brought to 270 ℃ and kept for 3 hours. After the reaction was cooled to room temperature, TiO_2 nanocrystals were washed and collected by the same procedures for octahedral bipyramidal nanocrystals synthesis. The nanocrystals were finally dispersed in 15 mL of anhydrous toluene.

Synthesis of square-shaped nanoplates

In a typical synthesis of square-shaped nanoplates, 0.248 g of TiF_4, 3 mL of OA and 7 mL of ODE were mixed to serve as precursor stock solution in an argon-filled glovebox. To ensure thorough dissolution of TiF_4, the mixture was stirred and gently heated under argon atmosphere for 1 hour. In a three-neck flask, 7.33 g of 1-hexadecanol, 10 mL of ODE and 0.5 mL of OA were mixed, purged with N_2 for 30 min at 120 ℃, then cooled down to 60 ℃. Upon the addition of 1.5 mL of precursor stock solution, the mixture was heated to 290 ℃ and kept for 10 min for seeding. Afterwards, 8.0 mL of precursor stock solution was pumped into the reaction mixture at the rate of 0.3 mL/min. After pumping in all the stock solution, the reaction mixture was cooled to room temperature followed by addition of 5 mL of anhydrous toluene. The nanocrystals were isolated by centrifugation at 6000 rpm for 5 min. After removing the supernatants, the nanocrystals were repeatedly washed by redispersing precipitates in 10 mL of anhydrous

toluene, sonication, addition of 200-proof ethanol (1:1) and centrifugation (8000 rpm/5 min) for two times. The final product was dispersed in 10 mL of anhydrous toluene.

Synthesis of fluorine-free rhombic nanocrystals

Rhombic-shaped nanocrystals were synthesized based on a solvothermal method. In the synthesis, 5.0 mL of BA, 2.0 mL of OAm and 0.25 mL of TTIP were first mixed in a 10 mL autoclave. After stirring at room temperature, the autoclave was sealed and then kept at 180 ℃ for 24 hours. After cooling to room temperature, the nanocrystals were isolated and washed by the same procedure described for TOB nanocrystals. The final product was dispersed in 5 mL of anhydrous toluene.

Seed-mediated growth on TOB-shaped nanocrystals

The seed-mediated growth process was also carried out under standard Schlenk line operation. TOB-shaped nanocrystals were chosen as the typical seeds for investigating the growth behavior. In a typical growth, 2.5 mL of toluene solution of TOB seeds was first mixed with 24 mL of OA by gentle magnetic stirring, then purged with N_2 at 130 ℃ for 30 min. Afterwards, the mixture was heated to 270 ℃, and 1.0 mL of TBOT was pumped into the mixture with the speed of 4.0 mL/h. After introducing all the precursor, the system was cooled to room temperature. The product was isolated, washed and finally dispersed by the same procedure described for TOB-shaped nanocrystals. To investigate the reaction mechanism and control the growth process, a series of control experiments are carried out. In order to investigate the effect of reaction time on the product, a synthesis was conducted under the same condition as described for typical seed-mediated growth except for keeping the reaction mixture at 270 ℃ for one more

hour after finishing the addition of TBOT. Aliquots were taken from the reaction mixture by glass syringe at 0.5 mL each time and quenched immediately by 1.5 mL of 200 proof ethanol. To investigate the effect of TBOT amount, the syntheses were conducted under the same condition as described for typical seed-mediated growth except for changing the TBOT amount to 0.5 mL and 2.0 mL. Syntheses with different TBOT introduction rate were also conducted. In these syntheses, seed-mediated growth reactions with TBOT amount at 2.0 mL were performed as described for typical seed-mediated growth except that the TBOT introduction rate was adjusted to 1.0, 2.0, 3.0, 6.0 mL/h. The synthesis was also carried out by quick injection of TBOT, followed by keeping the reaction at 270 ℃ for another 20 min before removing the heating mantle. After the syntheses, the products were washed and collected by the same procedures for the TOB-shaped nanocrystals. Seed-mediated growth reactions were also performed by using other types of faceted nanocrystals including nanorods, fluorine-free rhombic nanocrystals and square-shaped nanoplates as seeds. These syntheses were conducted similarly as described for typical seed-mediated growth with TBOT introduction rate at 2.0 mL/h.

2.2.3 Structural Characterizations

Transmission electron microscopy (TEM) studies were carried out using a Tecnai 12 microscope with an accelerating voltage of 120 kV, and high resolution transmission microscopy (HRTEM) images were obtained on a Hitachi H9000-NAR microscope with an accelerating voltage of 300 kV. All the TEM samples were prepared without any purification steps. Lengths and diameters were statistically measured by random selection of 50 particles in TEM images of appropriate magnifications. X-ray diffraction (XRD)

measurements were conducted on a Bruker D8 Advance Diffractometer with Cu Kα radiation (λ = 1.5406 Å). UV-vis absorption spectra were collected by testing a solution of nanocrystal on a fiber optic spectrometer (Ocean Optics, USB2000). Zeta potential measurements were carried out by testing a dilute aqueous solution of nanocrystals on Beckman Coulter Delsa Nano C Zeta Potential Analyzer. FTIR spectra were collected by testing a small amount of nanocrystal powders by Bruker ALPHA FTIR Spectrometer.

2.2.4 Photocatalysis

Phase transfer of nanocrystals

In the protocol of phase transfer of nanocrystals from toluene to water, TMAH was used as a phase transfer agent as it is known to be efficient in replacing the hydrophobic ligands on the surface of nanocrystals.[164, 165] Typically, a toluene solution containing approximately 0.2 g of nanocrystals was first transferred into a centrifuge tube. Nanocrystals were then precipitated from toluene solution by adding ethanol and centrifugation. Upon removal of the supernatant, 15 mL of ethanol and 5 mL of TMAH solution (25 wt% in H_2O) were added. The mixture was then subjected to sonication until the sample was fully dispersed without any notable insoluble solids. To ensure complete ligand exchange, the mixture was transferred into a 50 mL Erlenmeyer and stirred for another 3 days at room temperature. The hydrophilic nanocrystals were then collected from the colloidal suspension by centrifugation at 11000 rpm for 5 min. To remove remaining TMAH, 20 mL of ethanol was added to wash the precipitated nanocrystals by sonication followed by centrifugation at 11000 rpm for 5 min. The

washing process was repeated twice. After the final centrifugation, the as-obtained product was dried under vacuum at 75 ℃ overnight.

Photocatalytic activity test

The photocatalytic activity of the anatase TiO_2 nanocrystals was evaluated by their capability to degrade Rhodamine B (RhB) under UV light irradiation. After phase transfer, the nanocrystal powders were first dispersed in MiliQ water to make a 0.2 mg/mL stock solution. To carry out photocatalysis tests, 25 mL of the catalyst stock solution and 50 μL of RhB aqueous solution (10^{-5} M) were added to a quartz tube in a photoreactor (Xujiang XPA-7). To ensure homogeneous dispersity and sufficient adsorption, the solution was stirred in dark for 30 min. Thereafter, the solution was irradiated by a 300W Hg lamp with a 365 nm band-pass filter. The extent of RhB degradation at different irradiation time was determined by UV-Vis absorption measurement (HR2000CG-UV-NIR, Ocean Optics) of the solution after removal of catalyst by centrifugation at 14500 rpm for 5 min.

2.3 Shape control of anatase TiO_2 nanocrystals by addition of fluorine ions[166]

Our first strategy towards shape control synthesis of anatase TiO_2 nanocrystals is to add shape directing agent into the reaction mixture. Recent researches have revealed fluorine ion is an effective shape directing agent for anatase TiO_2 synthesis as they can selectively bind to and passivate the (001) surface of anatase TiO_2. As the result, anatase TiO_2 exposed with a larger percentage of (001) surfaces can be synthesized.[54, 161] During the syntheses, fluorine ions were also possible to be doped in anatase TiO_2, which

was reported to be beneficial for visible light photocatalysis applications. Herein, we propose by taking advantage of the shape directing capability of fluorine ions, anatase TiO_2 nanocrystals with controllable exposing facets can be synthesized. In our design, inorganic fluoride salt can be used as the fluorine source and by adding them into the TiO_2 nanocrystal synthesis reaction mixture under high temperature, the shape control can be realized.

2.3.1 Transformation of anatase TiO_2 nanorods

To start with, sodium fluoride was first added to an anatase TiO_2 nanorods-oleic acid suspension at high temperature. We expect a combination of oleic acid and sodium fluoride was expected to be able to assist the chemical transformation. From the literature, syntheses of anatase TiO_2 nanorods have been reported by several different methods.[58, 162, 163] The common feature of these syntheses is all of them are nonaqueous sol-gel syntheses with the presence of long carbon chain carboxylic acids. It is believed long carbon chain carboxylic acids can effectively bind to some facets of the anatase TiO_2 and orient the nanocrystals grow into rod structure.[58] By adapting a nanorods synthesis recipe reported by Hyeon et al, we are able to produce high quality anatase TiO_2 nanorods.[162] The typical TEM image of the anatase TiO_2 nanorods are shown in Figure 2.2a. The nanorods are typically 40 to 50 nm in length and 2 to 3 nm in diameter. From the high resolution TEM image (Figure 2.2a, inset), the nanorods were revealed to grow along the <001> direction. This method can be sorted as a typical sol-gel pyrolysis synthesis of anatase TiO_2. In the synthesis, a combination of titanium alkoxides and carboxylic acids at high temperature results in an esterification elimination reaction

which produces Ti-O species, similar to the hydrolysis process in conventional sol-gel reactions. Then, TiO_2 nanocrystals can be formed from these "monomers" via a nucleation and growth process. Long carbon chain carboxylic acids also play the role of ligands and direct the growth of nanocrystals into rod structure.

After the nanorods were synthesized, if NaF was added to the reaction mixture, it was found the shape of the nanorods can be gradually transforms to octahedral bipyramidal structure. From the TEM images, after addition of NaF and maintain the reaction temperature at 320 ℃ for 30 minutes (Figure 2.2b), the rod shape of the nanocrystals disappears and there exist both large and small nanocrystals with larger diameters. When the reaction was extended to 2 hours (Figure 2.2c), the larger nanocrystals exhibit a faceted octahedral bipyramidal structure and the amount of small nanocrystals significantly reduced. From both Figure 2.2b and 2.2c, it is observed the contrast for large nanocrystals is not even, with the inner part with a rod shape to be darker and the lengths of the nanocrystals are similar to those of nanorods. Meanwhile, the final shape of the nanocrystals also proved the nanocrystals still adopt the anatase phase. These results clearly indicate this reaction is a shape-directed isomerization process enabled by a ripening process. During this process, smaller nanorods were first dissolved and then re-deposited on larger nanorods. According to our understanding, the combination of fluorine ions and carboxylic acid at high temperature can accelerate the dissolution-redeposition process by producing hydrofluoric acid, which is a strong etchant for TiO_2. The etching process resulted in an increase of the concentration of titanium molecular species and consequently enabled the shape reconfigurations.

However, the growth direction of re-deposited TiO_2 did not yield to OA, which should help the nanocrystals maintain at rod structure. Therefore, it is believed with the existence of fluorine ions, the shape of the newly deposited TiO_2 will be dominated by fluorine ions. This synthesis proved by adding inorganic fluoride salt such as NaF into nonaqueous synthesis reaction, the shape directing effect of fluoride is significant and can be regarded as an effective method to allow shape control in synthesis of faceted anatase TiO_2 nanocrystals.

2.3.2 One-pot synthesis of fluorine doped TOB-shaped nanocrystals

We further improved this shape control synthesis strategy by addition of NaF at the beginning of the anatase TiO_2 nanorod synthesis. In the previous synthesis, the shape directing is only effective during the ripening process and the size of the nanocrystals is highly dependent on the original nanorods and there is a lack of control on the uniformity. However, by adding NaF into the reaction mixture at the beginning, the shape directing can happen during the nucleation and growth, which is expected to enable production of faceted anatase TiO_2 nanocrystals with better size control. Figure 2.3a to 2.3f are the representative low magnification TEM images of the nanocrystals taken from the aliquots of the synthesis reaction with addition of NaF at the beginning. From these images, it is revealed at the initial stages, short nanorods were formed. However, as the reaction time increased, the nanorods were not significantly elongated. Instead, their shape transformed to truncated octahedral bipyramidal (TOB) structures and their size kept increasing. The size uniformity of the nanocrystals is improved compared to those synthesized by chemical transformation. From the HRTEM images (Figure 2.3g, h), the TOB-shape

nanocrystals are in anatase phase and are enclosed by {001} and {101} facets. Although the {101} facets are still dominant, the size of the {001} facets considerably increased compared to nanorods. The corresponding FFT pattern of the HRTEM image also confirmed the nanocrystals were single crystalline.

In addition to shape directing during the synthesis, fluorine ions were also found to be doped into TiO_2 during the synthesis. From the XRD spectra of the aliquots (Figure 2.4a), it revealed during the reaction, the TiO_2 kept at anatase phase and the grain size kept increased within the increase of reaction time as the diffraction peaks got sharper. It was also found that NaF was nearly fully consumed at the first 10 minutes of the reaction. UV-vis absorption measurements and XPS measurements provided further evidence for fluorine doping in the anatase TiO_2. Compared to commercial P25 which is in white color, the synthesized anatase TiO2 nanocrystals were in light blue color. From the UV-vis absorption spectra (Figure 2.4b), the synthesized nanocrystals also showed enhanced absorption in visible region compared to P25. This is a clear hint for doping as the change of absorption profile cannot be ascribed to adsorption of the colorless fluorine ions. XPS measurements (Figure 2.4c-e) also provided evidence for doping as Ti 2p, O 1s and F 1s are all detected in the purified nanocrystal sample.

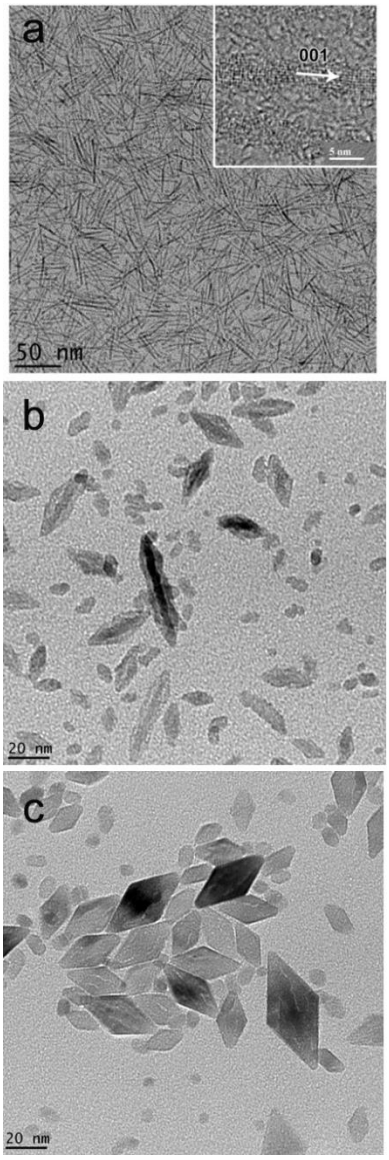

Figure 2.2 Transformation of nanorods to bipyramidal nanocrystals. TEM images of (a) as-obtained TiO_2 nanorods; (b-c) after adding NaF for (b) 30 min; and (c) 2 hours. Reprinted from ref. 166.

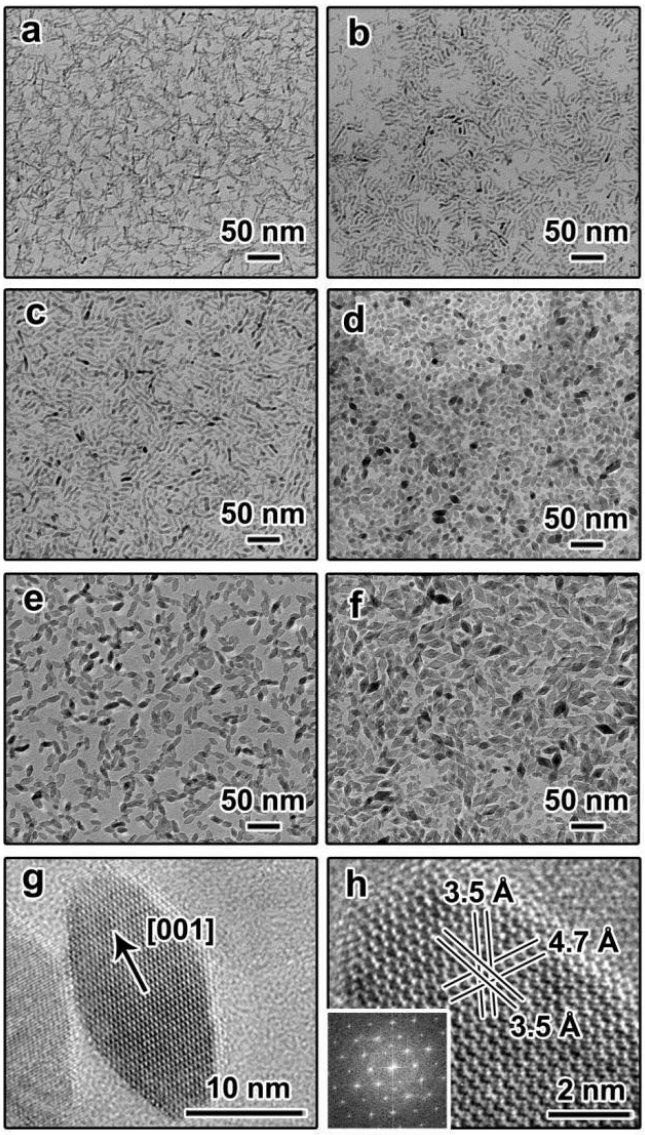

Figure 2.3 TEM images showing the evolution process of TiO_2 nanocrystals with TOB shape in one-pot synthesis. (a-e) TEM images of the as-prepared nanocrystals by taking samples from the reaction system at (a) 250 °C and after reacted at 270 °C for (b) 1 min; (c) 5 min; (d) 10 min; (e) 30 min; and (f) 180 min. The HRTEM images (g) and (h) show the crystal structure of the as-obtained nanocrystals. Reprinted from ref. 166.

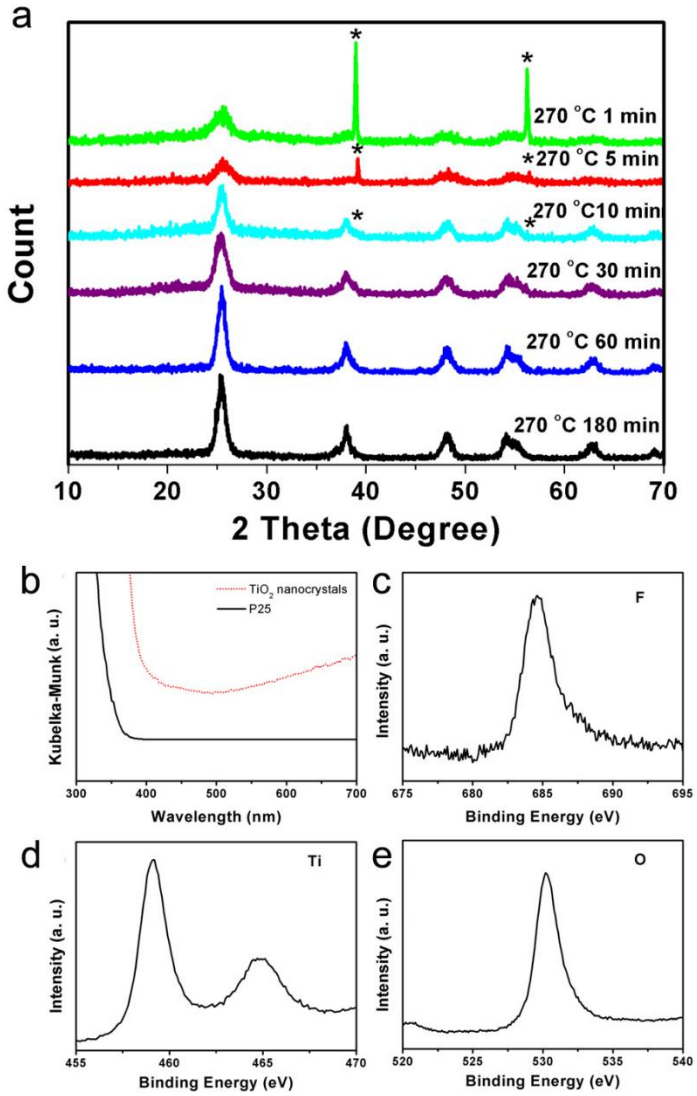

Figure 2.4 (a) XRD characterization of the aliquots during the synthesis. It proved a successful dissolution of NaF and a continuous growth of anatase TiO_2. (b-e) UV-vis absorption spectra (b) and XPS measurement confirmed the fluorine doping in the product nanocrystals (c-e). Reprinted from ref. 166.

2.4 Seed-mediated growth of anatase TiO_2 nanocrystals with core-antenna structures[167]

Although shape control synthesis of anatase TiO_2 nanocrystals has been realized by addition of shape directing agent such as fluorine ions, to construct nanocrystals with high complexity structures in predictable manners, seed-mediated growth synthesis strategy was considered to be appropriate to adopt. Solution-based seed-mediated growth has been regarded as a reliable method for the production of various types of nanostructures with tightly controlled size and size/shape uniformity since the existence of seeds can minimize self-nucleation which otherwise may cause inhomogeneity, and the well-defined shape of seeds can also direct the growth of the resultant nanocrystals. In addition, the formation of seeds and their after-growth can be carried out separately under different conditions, thus allowing a high degree of control over the complexity of the final structures. In this work, we demonstrate that seed-mediated growth of anatase TiO_2 nanorods onto TiO_2 nanocrystal seeds pre-synthesized with different shapes can produce complex core-antenna structures with high uniformity. By controlling the reaction kinetics during the growth stage, we have been able to not only avoid the self-nucleation but also control to the number, diameter, and length of nanorod antennas.

2.4.1 Synthesis of broom-like core-antenna nanocrystals

We first chose the TOB-shape nanocrystals as seeds to produce broom-like core-antenna nanocrystals. As shown in the typical TEM images (Figure 2.5a, b), the seed nanocrystals are elongated particles with average length of 14.5 nm (ranging from 8 to 30 nm) and diameter of 8.0 nm (ranging from 5 to 15 nm). To synthesize anatase TiO_2

nanocrystals with core-antenna morphology, the seed-mediated growth was carried out under a reaction condition similar to that of standard anatase nanorods synthesis, but in the presence of TOB nanocrystals and with a reduced reaction temperature from 300 ℃ to 270 ℃. In this case, titanium precursor (TBOT) was introduced dropwise to the mixture in order to minimize self-nucleation. OA was used as the solvent, hydrolysis agent as well as ligand binding to the nanocrystal surfaces. In a typical synthesis, the amount of TBOT was 1.0 mL and its feeding rate was 4.0 mL/h. After the introduction of TBOT, the heating source was removed immediately and the resultant nanocrystals were washed and characterized. Figure 2.5c is a TEM image showing the broom-like core-antenna morphology of the resultant nanocrystals synthesized through the typical condition. The core of the resultant nanocrystal is in cuboids morphology and there exist two antenna nanorods, one on each end of the core with clear orientational correlation. A small portion of them have multiple antennas. The length (average at 19.5 nm, ranging from 15 to 30 nm) and diameter (average at 9.8 nm, ranging from 8 to 15 nm) of the cores are slightly larger than that of the original TOB seed nanocrystals, indicating certain degree of overgrowth of the seeds. The length of the antenna rod is 33.6 ± 5.2 nm and diameter is 3.0 ± 0.4 nm. According to the HRTEM image of a core-antenna nanocrystal (Figure 2.5d), the {101} facets were no longer the major exposing facets of the core. Instead, {001} facets at the original tip sites and {100} side facets are evolved. Besides, the growth of antenna rods can be indexed towards <001> direction and there was no obvious defect at the junction between the core and the antenna rods. The corresponding FFT pattern along [100] zone axis of the HRTEM image further confirmed the single

crystalline nature of the core-antenna nanocrystals (Figure 2.5d, inset). XRD analysis also indicated that the resultant nanocrystals were still in pure anatase phase (Figure 2.5e). Compared to the XRD patterns of the original TOB seeds, the (004) peak is more profound than the (200) peak for the core-antenna nanocrystals, which is consistent with the fact that nanocrystals experienced a directional growth along <001>.[58]

2.4.2 Formation mechanism of core-antenna nanocrystals

Based on the structural characterization, we propose that the core-antenna TiO_2 nanocrystal formation follows a seed-mediated epitaxial growth process. As discussed in the last section, in typical synthesis of TiO_2 nanocrystals via nonaqueous sol-gel pyrolysis reaction, a combination of titanium alkoxide and carboxylic acids at high temperature results in an esterification elimination reaction which produces Ti-O species.[162, 163] Then, nanocrystals were formed through the nucleation and growth process by consumption of these “monomers”. In the current case, preexisting TOB seeds were present at the initial stage of the synthesis, which were however not observed after the completion of the reaction. The final product only contained uniform core-antenna structures. Thus, we believe under our reaction conditions, although Ti-O molecular species can be produced through the hydrolysis process, their nucleation into new nanocrystals was inhibited. All the newly formed Ti-O species were deposited onto the existing TOB seeds. Moreover, since the resultant nanocrystals were single crystalline and no free particles of other morphologies could be found, it can be concluded that the growth adopted epitaxial growth pathway rather than oriented attachment of the TOB seeds and self-nucleated particles.

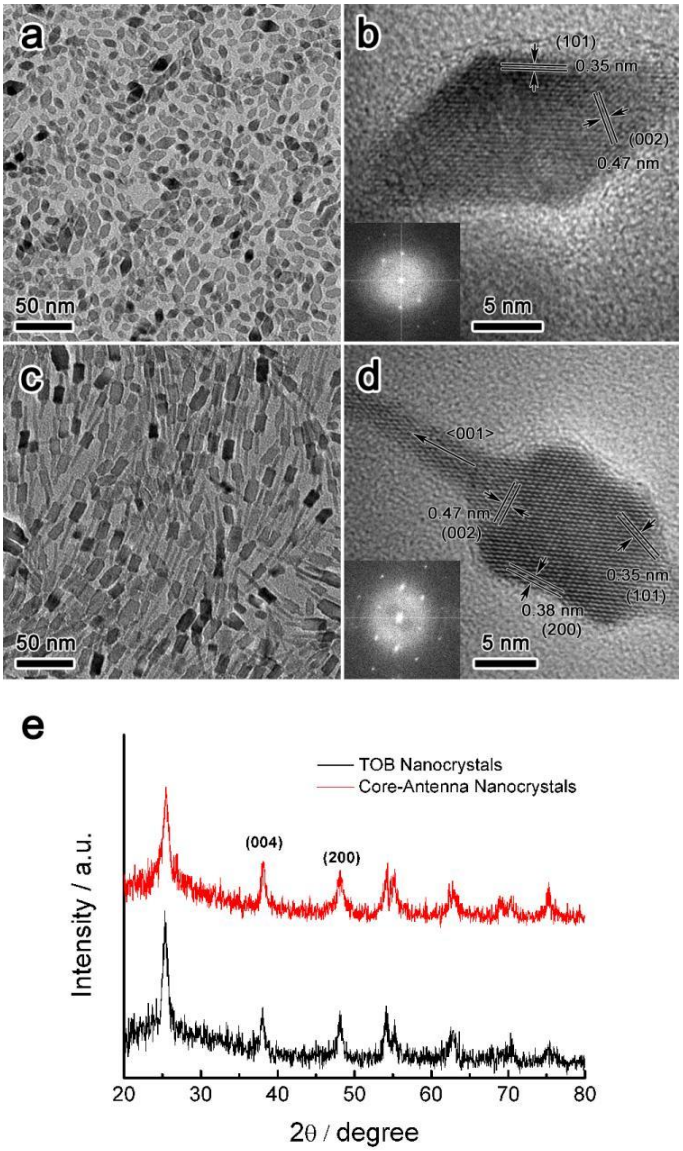

Figure 2.5 Structural characterization of TOB nanocrystal seeds and core-antenna nanocrystals after seed-mediated growth. (a, c) Low magnification TEM image of TOB and core-antenna nanocrystals. (b, d) Typical HRTEM images of TOB and core-antenna nanocrystals. Insets in (b) and (d) are the corresponding FFT patterns (along [100] zone axis). (e) XRD patterns of TOB and core-antenna nanocrystals. Reprinted from ref. 167.

The synthesis was repeated under the same condition but with extended heating at 270 ℃ for 1 hour after the complete introduction of TBOT. The morphology of the products taken at different stages showed similar core-antenna structure (Figure 2.6a, b). Statistical analysis on the antenna rods obtained at different stages shows no obvious change in length (Figure 2.6c), indicating that the seed-mediated growth reaction was completed right after the addition of TBOT, and the ripening process which may cause shape transformation after epitaxial growth did not occur substantially within the duration of one hour.

We further carried out syntheses with different TBOT introduction amount in order to reveal the pathway of surface deposition. Figure 2.7a is a TEM image that illustrates the morphology of the resultant nanocrystals when introducing 0.5 mL TBOT rather than 1.0 mL in the typical synthesis. In this case, less TBOT was used and TiO_2 growth was less extensive compared to the typical case. As the result, only nanocrystals with ellipsoids and cuboids can be observed. The HRTEM image and corresponding FFT along [100] zone axis (Figure 2.7b) further confirmed the nanocrystals were single crystalline with anatase structure. These results indicate that the first stage of growth is the development of the cores. When the TBOT introduction amount changed from 1.0 mL to 2.0 mL, the resultant nanocrystals exhibited core-antenna morphology with two or three antenna rods at each end of the cuboidal shaped cores (Figure 2.7c). While the average diameter of the cores remained similar to that of the typical core-antenna nanocrystals synthesized with 1.0 mL TBOT, the lengths of the rods on each core varies, suggesting that they were grown at different stages. The HRTEM image taken at the

junctions of the core and antennas of a typical such nanocrystal (Figure 2.7d) revealed the newly formed nanorods were also epitaxially grown on the core, while the corresponding FFT pattern confirmed the core-antenna nanocrystal still maintained single-crystallinity.

The seed-mediated growth can be divided into three steps: (1) formation of Ti-O molecular species by sol-gel esterification reaction; (2) diffusion of the as-formed Ti-O species to the nanocrystal-solvent interface; and (3) deposition reaction of the Ti-O molecular species to the surface of TOB seed nanocrystals. The crystal growth pathway should be described as a successive <001> unidirectional growth process with several stages (Figure 2.8). In the early stage, the <001> advancement took place primarily by epitaxial growth on {101} facets and resulted in the formation of ellipsoidal and cuboidal cores. Typically, large seed nanocrystals appeared to be ellipsoidal as the overgrown TiO_2 was relatively small so the seed nanocrystals did not vary significantly from their original TOB shape, while smaller seeds experienced more significant overgrowth and tended to transform to cuboidal structures. While the fast growing {101} facets were gradually consumed due to overgrowth, monomers produced by further introduction of TBOT were subsequently deposited to the secondary fast growing {001} facets, and therefore caused the surface nucleation and evolution of nanorods. The reaction condition, which was adapted from pure nanorod synthesis, supported preferential one-dimension growth of TiO_2 into nanorod antennas. Consistent with the classic anisotropic nanocrystal growth governed by kinetic control and selective ligand adhesion,[10] the diameter of the as-formed nanorods was found to be in the same range of as that of the pure TiO_2 nanorods prepared under similar reaction condition. When the precursor concentration was

relatively low, the area of {001} tips of the overgrown TOB nanocrystals was considerably small which could support the growth of only one nanorod. Under the condition where extensive overgrowth was possible, the areas of the {001} tips were larger so that two or more nanorods could be formed on one tip.

Although according to the law of Donnay and Harker,[168, 169] {001} facets of anatase TiO_2 have higher surface energy than {101}, such a rule is only valid for crystals with clean surfaces. For colloidal nanocrystals, they are covered with organic ligands which can dramatically change the relative surface energy of the crystal facets. In the standard reaction for growing anatase nanorods, OA molecules as capping ligands can selectively adhere to some facets and reduce their tendency of growth.[58] It was believed that the growth of the side facets of the nanorods was inhibited, although the details of these side facets was not clearly identified in previous reports.[163] Base on literature and our own HRTEM studies, there appears to be no well defined facets on the sides of the nanorods, making us believe that the sides are covered with a combination of very small facets that are stabilized by the capping ligands. This however remains to be an interesting topic for further in-depth studies.

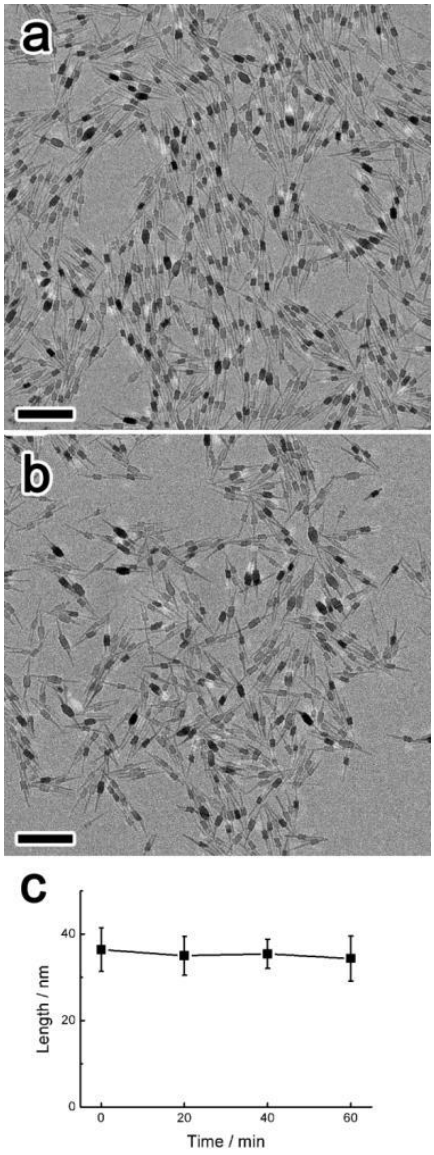

Figure 2.6 The effect of heating time on the morphology of the core-antenna nanocrystals. (a, b) TEM images of the core-antenna nanocrystals synthesized (a) right after the complete addition of precursor solution and (b) with 1 hour of additional heating at 270 ℃. Scale bar = 100 nm. (c) Plot showing the dependence of the length of antenna nanorods on additional heating time. Reprinted from ref. 167.

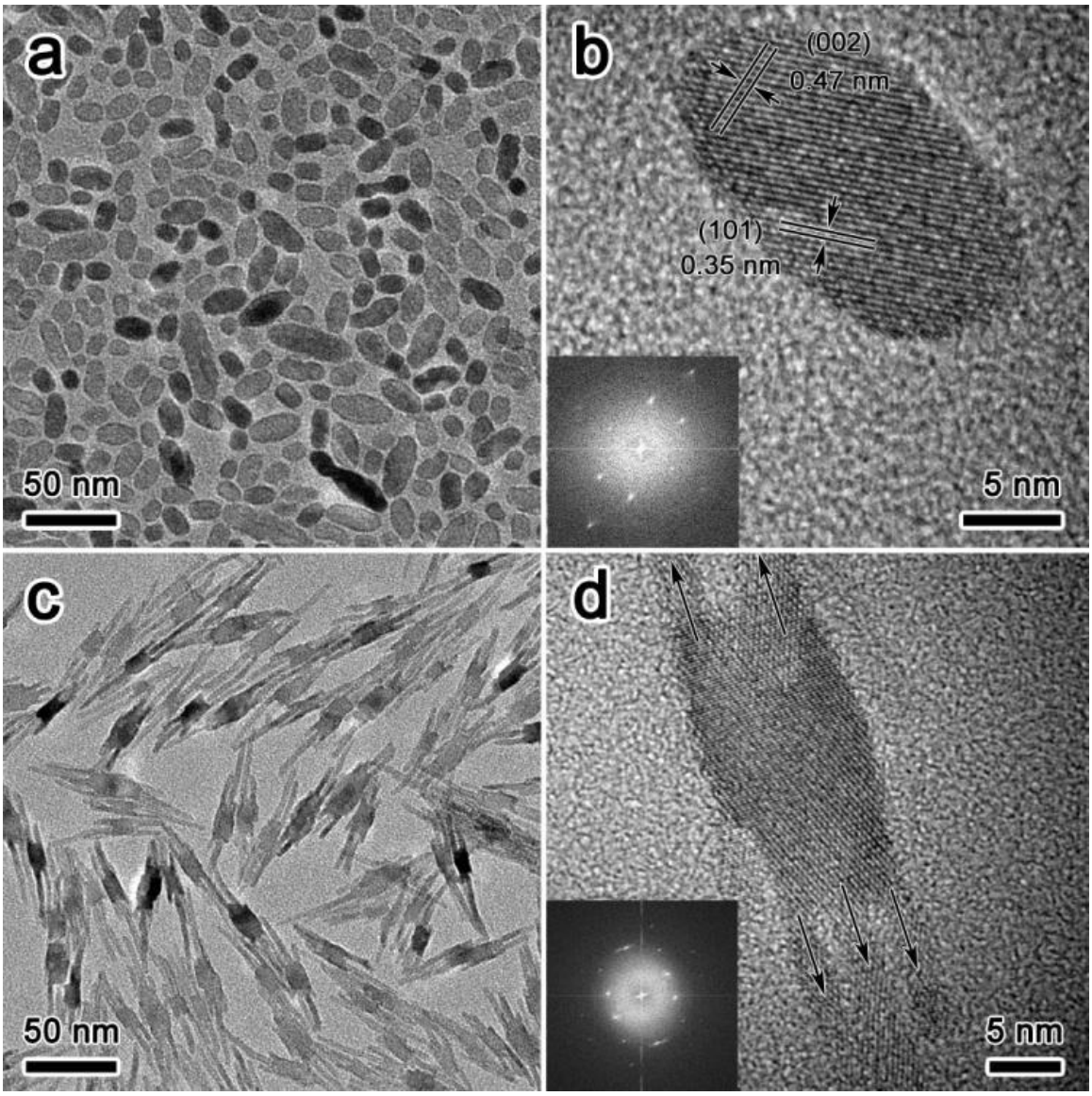

Figure 2.7 TEM and HRTEM images of nanocrystals synthesized with (a, b) 0.5 mL and (c, d) 2.0 mL of TBOT under the typical conditions. Insets in (b) and (d) are the corresponding FFT patterns (along [100] zone axis). The arrows in d) indicate the <001> direction. Reprinted from ref. 167.

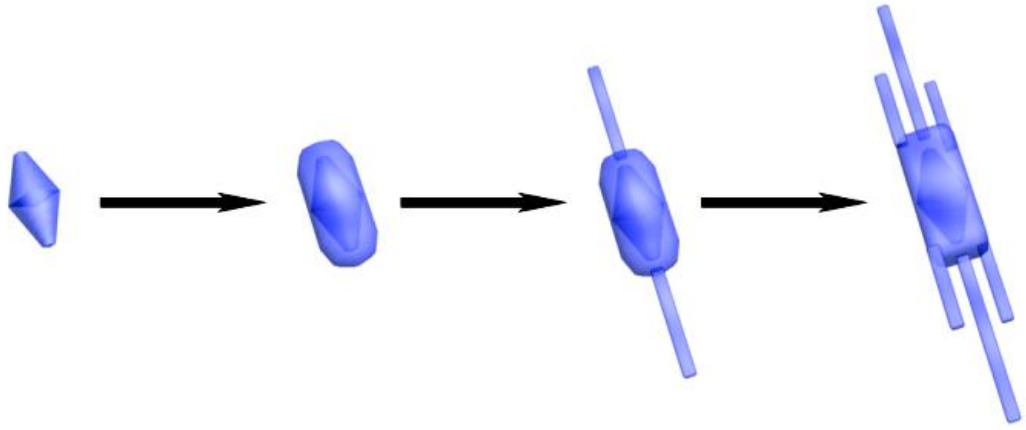

Figure 2.8 Schematic illustration showing the growth pathway of core-antenna nanostructures from TOB-shaped seeds. Reprinted from ref. 167.

During the initial overgrowth stage in the current synthesis, {101} facets actually grew faster so they quickly varnished, leaving the nanocrystals covered with relatively lower energy side facets and {001} tip facets — a condition similar to that of pure nanorod synthesis. Further growth on such seed crystals can only occur on the {001} faceted tips, producing the core-antenna structures. The <001> advancement from TOB seed nanocrystals started from deposition of Ti-O molecular species on both {001} and {101} facets and caused shape transformation of the seeds from TOB to ellipsoids or cuboids. When {101} facets were eliminated and sufficiently large {001} were produced, dominant growth would be along <001> direction and therefore formed nanorod antennas.[170]

To rule out the possible effect of the fluorine doping in the TOB seeds to the seed-mediated growth reaction, rhombic anatase TiO_2 nanocrystals were synthesized via a solvothermal reaction in nonpolar solvent without the presence of fluorine and then used as the seed nanocrystals.[164] This type of nanocrystals was chosen since they have similarity to the typical TOB nanocrystals. Firstly, they were both synthesized in nonpolar solvent and possess hydrophobic surfaces. Second, they were similar in morphology, both in size and shape. Figure 2.9a is a typical TEM image for the anatase TiO_2 nanocrystals synthesized without fluorine. The nanocrystals were clearly enclosed by well-defined facets with a rhombic shape. The average length of the nanocrystals is 18.7 nm (ranging from 12 to 25 nm) and the average diameter is 7.4 nm (ranging from 5 to 10 nm). High resolution images (2.9b, c) further confirmed that the nanocrystals were mainly enclosed by {001} and {101} facets. The seed-mediated growth was performed

under the same condition as for the typical TOB seed nanocrystals. OA was still used as both the solvent and the capping agent. According to the TEM and HRTEM images of the resultant nanocrystals (Figure 2.9d-f), the products also adopted the core-antenna morphology and the growth is along the <001> direction, consistent with the growth behavior with the TOB seeds. There were slight differences in morphology, including the shape of the core, the number and the diameters of antenna rods, between the nanocrystals synthesized from the rhombic seeds and TOB seeds, mostly due to the differences in the size and shapes of the seed nanocrystals and the precursor/seed ratio. Nevertheless, the formation of nanorod antennas through unidirectional growth along <001> direction is a consistent growth behavior for both the TOB nanocrystals and the fluorine-free rhombic seed nanocrystals, so it can be concluded fluorine does not make major contributions to the seed-mediated growth process.

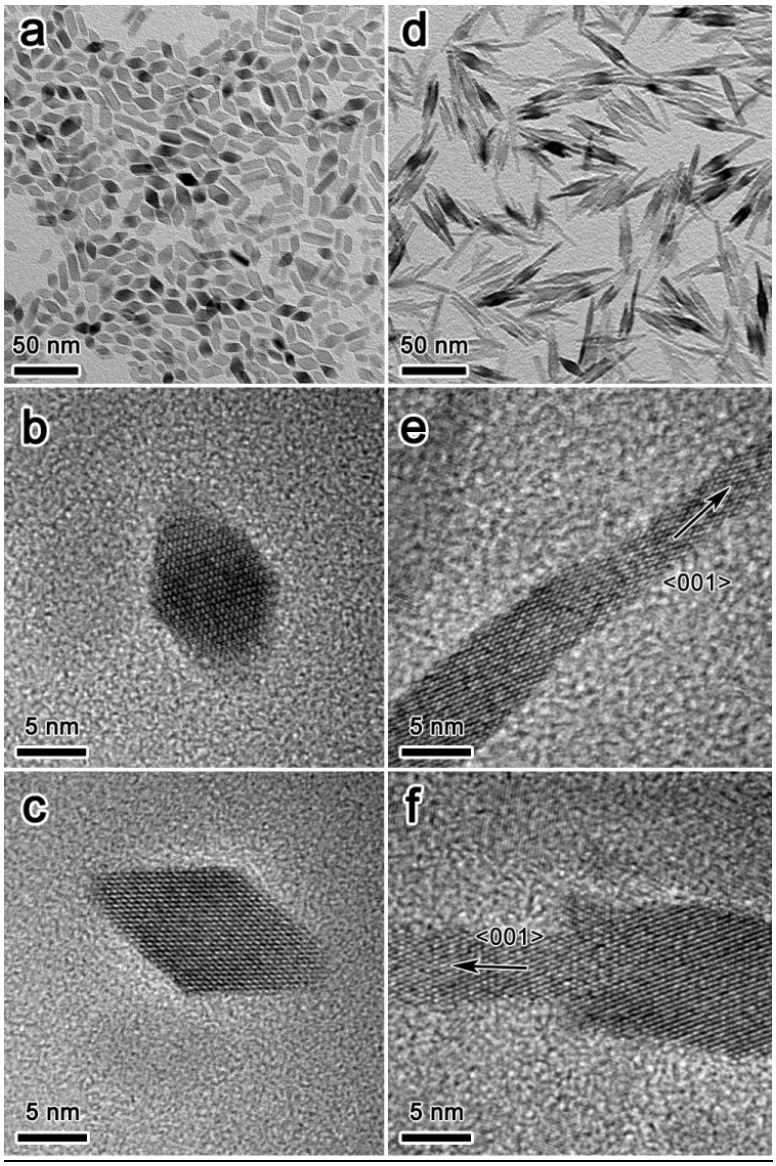

Figure 2.9 TEM and HRTEM images of (a-c) rhombic anatase TiO_2 nanocrystal seeds and (d-f) the resultant nanocrystals after seeded growth. Reprinted from ref. 167.

2.4.3 Control the growth by manipulating the growth kinetics

As with many colloidal pyrolysis syntheses, the kinetics plays an important role in determining the exact morphology of the final products. Hereby, we realized control over reaction kinetics by changing the TBOT introduction rate. As the diffusion of Ti-O molecular species to the nanocrystal surface is the rate-limiting process, the introduction rate of TBOT determines the concentration of monomer species, which has proven to be crucial for the growth behavior of other nanorods in prior studies.[171] A higher concentration of Ti-O monomers is therefore expected to promote the anisotropic growth of the nanorods.

Figure 2.10 illustrates the morphology of the nanocrystals produced with 2.0 mL TBOT at the introduction rate varying from the typical 4.0 mL/h to 1.0 mL/h (Figure 2.10a), 2.0 mL/h (Figure 2.10b), 3.0 mL/h (Figure 2.13a), 6.0 mL/h (Figure 2.10c), and instant injection (Figure 2.10d). As shown in Figure 2.10a,b and 2.13a, when decreasing the TBOT introduction rate, the nanorods grown on the core exhibited a decrease in anisotropy since the diameter of the nanorod increased (4.4 nm in Figure 2.10a, 3.6 nm in Figure 2.10b and 3.2 nm in Figure 2.13a compare to 3.0 nm in Figure 2.7c) while the length decreased (the average length of the longest rod on the core decreased from 33.6 nm in Figure 2.7c to 20.1 nm in Figure 2.10a, 26.2 nm in Figure 2.10b and 31.4 nm in Figure 2.13a). At the same time, it can be observed that there were only one or two nanorods on each end of the core of nanocrystals demonstrated in Figure 2.10a, while in both Figure 2.10a and 2.10b, most of the cores have been fully developed into cuboids structure. In contrast, an increase in TBOT introduction rate will result in increase in

anisotropy of the growth. The nanocrystals synthesized with the TBOT introduction rate of 6.0 mL/h showed three or more antenna rods on each end of the core (Figure 2.10c), with the length of the nanorods increased (the average length of the longest rod increased to 50.1 nm) and the diameter decreased (the average diameter was 2.8 nm) compared with samples made with lower TBOT introduction rates. Meanwhile, the cores majorly remained as bipyramidal morphology instead of fully developing into cuboids. Figure 2.10e summarized the influence of TBOT feeding rate on the lengths and diameters of the antenna rods and the plot clearly proved the kinetic effect on the morphology control in the seed-mediated growth. In the case of quick injection of TBOT, since the Ti-O concentration got too high, self-nucleation occurred so that free nanorods were the major products. Nevertheless short nanorod antennas could still be observed on each bipyramidal core (Figure 2.10d).

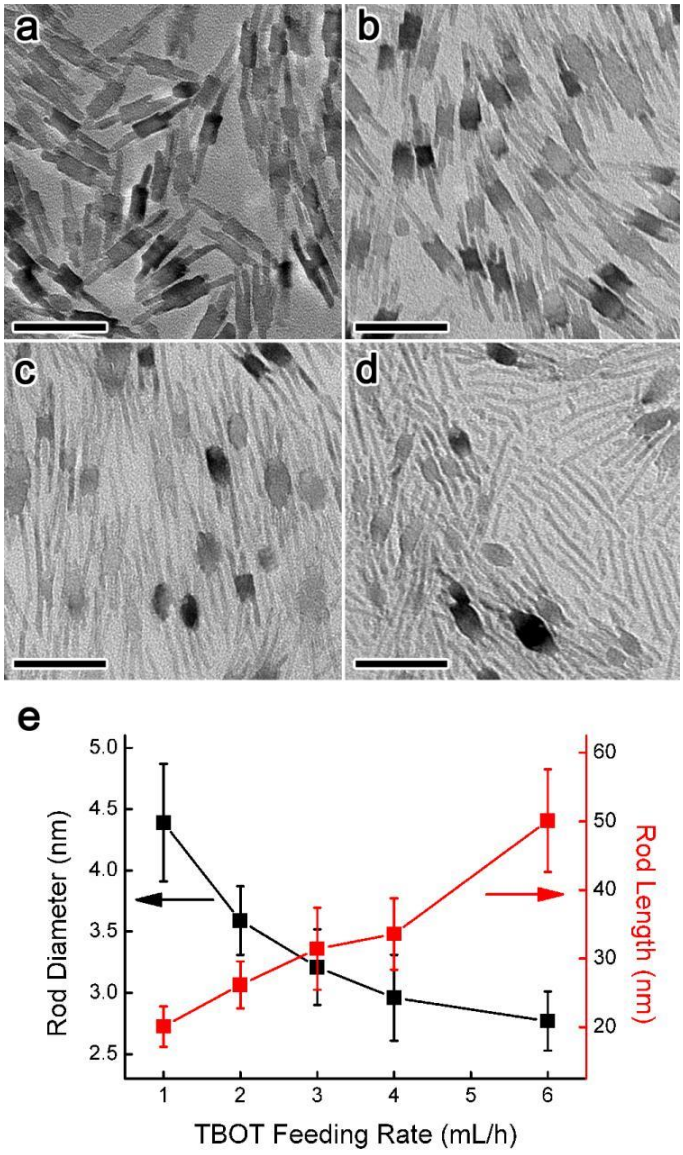

Figure 2.10 The effect of TBOT feeding rate on the growth behavior. (a-d) TEM images of resultant nanocrystals with introduction rate at (a) 1.0 mL/h, (b) 2.0 mL/h, (c) 6.0 mL/h, and (d) quick injection. Scale bar = 50 nm. (e) Change of length, diameter of the longest antenna nanorods with the change of the TBOT feeding rate. Reprinted from ref. 167.

This series of experiments proved that the extent of rod growth can be controlled by changing TBOT introduction rate, which significantly affected the monomer concentration, and was reflected on the anisotropy of the antenna nanorods as well as the shape of the cores. The anisotropy of the rods decreased with the reduction in TBOT introduction rate and vice versa. The cores tended to develop into cuboids when the introduction rate was low while remained as bipyramidal shape when the rate was high. This is consistent with our general understanding of the growth behaviors: at a low monomer concentration, the {101} facets can grow more extensively to change the shape of the cores as the driving force for nanorod formation was low, while a high monomer concentration could drive the epitaxial growth of nanorods at a much earlier stage when no significant deposition has occurred on the core surface. These results clearly demonstrate the advantage of the seed mediated growth process in controlling the number, length and diameter of the antenna rods of the core-antenna nanocrystals.

2.4.4 Growth on seeds with different shapes

The above-demonstrated syntheses have indicated the directional epitaxial growth of nanorods on seeds along the <001> direction. As the growth is limited by how large the {001} surface of the seed nanocrystal is, it is expected by enlarging or shrinking the {001} surfaces of seed nanocrystals, tunable amount of aligned nanorod antennas can be fabricated and core-antenna nanocrystals with complex morphology could be created. Here we choose two types of nanocrystals to represent the two extreme cases of seeds with small and large {001} surfaces – anatase TiO_2 nanorods and square-shaped nanoplates.[161, 162] Both of them were synthesized from nonaqueous sol-gel pyrolysis

methods according to previous reports and therefore possessed hydrophobic surfaces and could accommodate the seed-mediated growth at later stages.

Figure 2.11a shows the TEM images of the original nanorod seeds, which are 43 ± 8 nm in length and around 3 nm in diameter. As described in the last section, the longitudinal direction of the nanorods was <001>.[151, 162] This represents the case with an extremely small {001} surface area (maximum of 3×3 nm^2) as compared to TOB nanocrystals whose possible {001} surface area is at the scale of 8×8 nm^2. As no extensive overgrowth can occur from the sides, the epitaxial growth on each small {001} tip is expected to produce only one nanorod antenna, which is effectively elongating the original nanorod. This is confirmed by the TEM images of the nanocrystals after growth (Figure 2.11b). Overall, the nanocrystals after the growth were still in rod morphology and the length of these nanorods significantly increased to 95 ± 21 nm, which clearly proved that the overgrowth of TiO_2 adopted the <001> directional seed-mediated growth pathway.

An opposite case to a nanorod seed is a TiO_2 nanoplate which can provide much larger {001} surfaces for antenna rod growth. The square-shaped nanoplates were synthesized by pyrolysis of TiF_4 in the existence of oleic acid and long carbon chain alcohol. In addition to fluorine, long carbon chain alcohol can further assist the expansion of {001} surfaces of anatase TiO2. Thus, the product nanocrystals exhibit nanoplate morphology with major exposing facet to be {001}. As shown in Figure 2.12a, b, the square-shaped nanoplates are with an edge length of 40 ± 5 nm and a thickness around 3 nm. Therefore, in this case, the {001} surface area could reach as large as 40×40 nm^2.

Compared to TOB nanocrystals, the nanoplates have a much larger {001} surface. As shown in Figures 2.12c, d, an array of antenna nanorods were formed on each side of the nanoplates after performing seed-mediated growth, producing a brush-like morphology. Most of the brush structures appear to stand on the edge of the original nanoplates because the side became effectively larger after the overgrowth of antenna nanorods and subsequently more stable in terms of gravitational potential energy. It was found that the thickness of the nanoplate cores slightly increased to around 5 nm, indicating certain amount of overall deposition on the {001} facets. Similar to the previous broom-like case, the density and length of nanorods on the nanoplates could be tuned by controlling the amount of TBOT introduced to the seed-mediated growth reaction. When a small amount of TBOT (0.5 mL) was used, as shown in the TEM image of the resultant nanocrystal in Figure 2.12c, e, the antenna nanorods were loosely packed on the nanoplates with a relatively short length. With 1.0 mL TBOT, both the density and length of the antennas increased (Figure 2.12d). Since the antenna rods were vertically standing on the surface of the nanoplates, which correspond to the {001} facets, it can be determined the antenna nanorod also kept <001> growth direction.

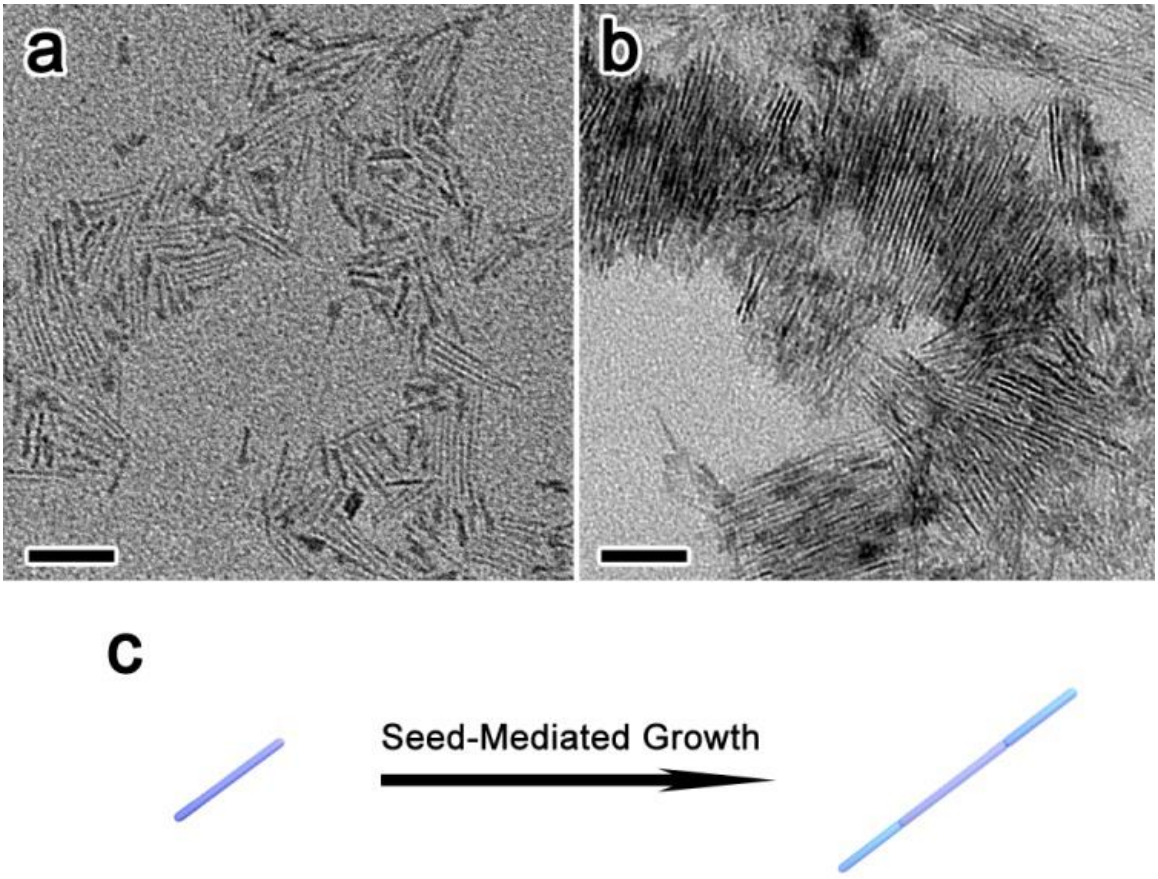

Figure 2.11 Growth of TiO_2 nanorods on nanorod seeds. (a) TEM image of anatase TiO_2 nanorod seeds. (b) TEM image of the elongated nanorods after seeded growth. Scale bar = 50 nm. (c) Schematic illustration of the growth behavior. Reprinted from ref. 167.

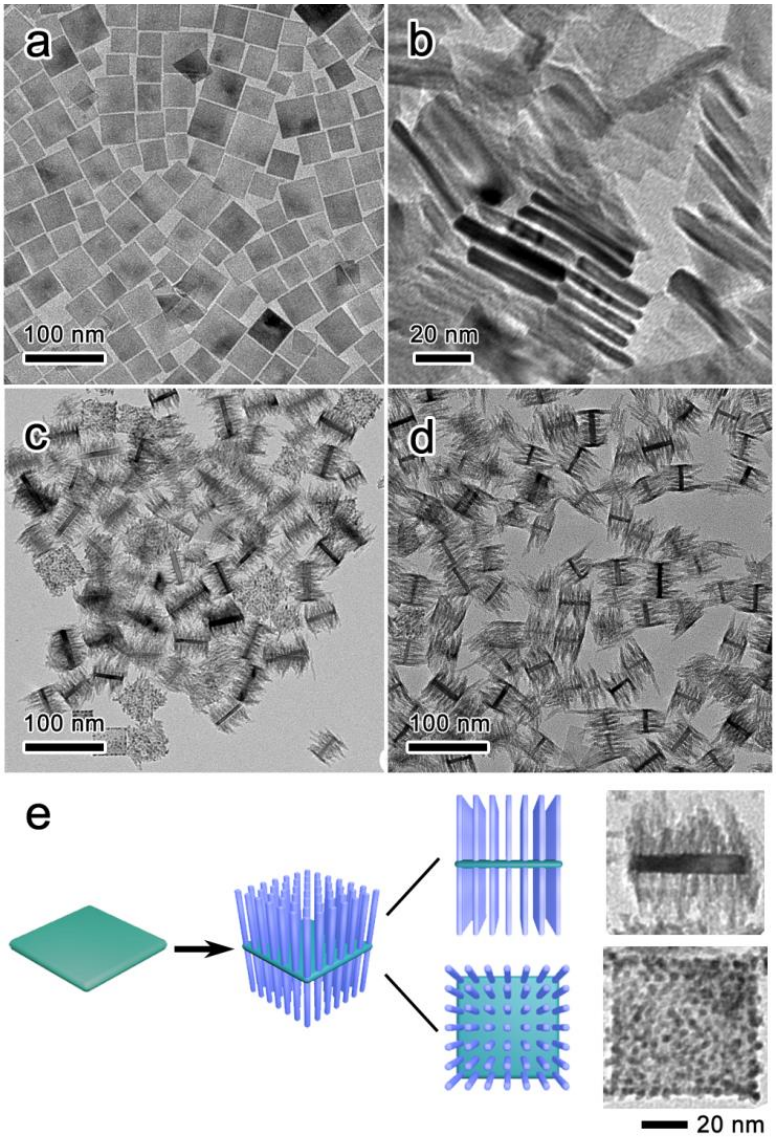

Figure 2.12 Seed-mediated growth of TiO_2 nanorods on square-shaped nanoplates. (a, b) TEM images of nanoplate seeds horizontally lying (a) and vertically stand (b) on the grids. (c, d) TEM images of brush-like nanocrystals produced by addition of 0.5 mL (c) and 1.0 mL (d) of TBOT. (e) Schematic illustration of the growth behavior and representative brush-like nanocrystals imaged at different orientation. Reprinted from ref. 167.

2.5 Photocatalytic performance of anatase TiO_2 nanocrystals with different shapes[167]

The seed-mediated epitaxial growth has the advantage of high flexibility and predictability in designing complex nanostructures with desired configuration, thus allows convenient optimization of their properties. As a demonstration, we systematically investigated the photocatalytic performance of anatase TiO_2 nanocrystals with different shapes by using photocatalytic oxidation of rhodamine B by irradiation of UV light as a model system. We revealed that the core-antenna structures can be optimized to achieve high photocatalytic activities, significantly better than individual simple shape nanocrystals.

2.5.1 Phase transfer of nanocrystals

Different types of anatase TiO_2 nanocrystals were first transferred from non-aqueous solvents to water by a pre-established method, in which TMAH was used as phase-transfer agent to make nanocrystals dispersible in water.[164, 165] As a strong base, TMAH slightly etches the surface of TiO_2 nanocrystals and render it a relatively high density of hydroxide groups. The core-antenna morphology of the nanocrystals remained after phase-transfer. As an example, Figures 2.13a,b demonstrate the morphology of the typical broom-like core-antenna nanocrystals prepared with addition of 2.0 mL TBOT at the rate of 3.0 mL/h before and after phase transfer, proving that the phase transfer process did not significantly disturb the core-antenna morphology. Comparing the FTIR spectra of the nanocrystals before and after phase transfer (Figure 2.13c), it is clear that the peaks from $–CH_2-$ asymmetric and symmetric stretching modes (2926 cm^{-1} and 2850

cm^{-1}) and $–COO^-$ symmetric and antisymmetric vibration modes (1520 cm^{-1} and 1430 cm^{-1}) disappeared after phase transfer, which proved the removal of oleic acids capping layer. The FTIR spectrum for the sample after phase transfer also display an extra peak at 1487 cm^{-1}, which corresponds to asymmetric deformation of $-CH_3$ in TMA^+, suggesting the presence of TMAH molecules around the nanocrystals.

2.5.2 Photocatalytic activities of nanocrystals with different shapes

Figure 2.14a demonstrated the photocatalytic activities of anatase TiO_2 nanoplates, nanorods and brush-like core-antenna nanocrystals. When pure original nanoplates or nanorods were applied as catalysts, after 25 min of UV-light illumination, only 40% and 30% of the dye was degraded. In comparison, the brush-like core-antenna nanocrystals derived from nanoplates with different amounts of TBOT addition showed consistently improved performance: For catalysts synthesized with increasing amount of TBOT from 0.2 mL to 1.5 mL, the percentage of dye degradation increased from 66% to 91% after 25 min of UV-light illumination. The photocatalytic activities of TOB nanocrystals and broom-like nanocrystals are also shown in Figure 2.14b. The performance of TOB nanocrystals was found to be superior to pure nanorods and nanoplates and the broom-like nanocrystals grown from TOB nanocrystal seeds displayed higher catalytic performance than brush-like nanocrystals. Comparing the performance of broom-like nanocrystals grown from different conditions, it is found the best performance was given by the one synthesized under the moderate TBOT introduction rate (3 mL/h), which is slightly better than that of the commercial P25. After light illumination for 5 min, this broom-like nanocrystal catalysts decomposed 73% of the dye compared to 66% by the

commercial P25, while both catalysts were able to completely decompose the dye within 25 min. Broom-like nanocrystals synthesized under higher or lower TBOT introduction rate are less powerful in the degradation reaction, but all of them showed improved performance than the seed TOB seed nanocrystals.

As is well known, the photocatalytic activity of anatase TiO_2 nanocrystals is governed by factors including their crystallinity, surface area and exposed facets. Our previous study has revealed the size of the anatase TiO_2 crystal grain as well as the surface area has a significant effect on the photocatalytic activity of mesoporous TiO_2 shells.[136, 137] With the increase of the grain size from 4.3 to 12 nm, the catalytic activity monotonically increases, which indicates an optimal size of crystal grain is desired for obtaining the best photocatalytic activity of anatase TiO_2. Regarding the facet effect on photocatalytic performance, although still under debating, it is generally accepted that the photocatalytic activity of the {100} facets are higher than that of the commonly produced {101} and {001} facets.[143, 147]

Pure nanorods are one-dimensional nanocrystals with lateral dimensional less than 3 nm. This size limitation prevents them to be optimal for photo-oxidation. This problem may also limit the square-shaped nanoplates as their thickness is around 3 nm as well. Besides, the major exposing {001} facets of square-shaped nanoplates are not beneficial for high photocatalytic activity. These limitations however were relieved in brush-like core-antenna nanocrystals. When TiO_2 nanorods were vertically grown onto the nanoplates, the lateral dimension of the nanocrystal significantly increased since not only the thickness of the core increased but there existed vertical standing nanorod which

can further change the dimension. On the other hand, the growth of nanorod decreased total area of the {001} facets in the nanocrystals. In addition, the formation of nanorod antenna array on the nanoplate was expected to increase the surface area of the system, which was reflected by the charge density of the nanocrystals as the surface was covered by hydroxide groups resulting from TMAH etching. Compared to the pure nanoplates, brush-like nanocrystals have a higher zeta potential (-53 to -68 mV for brush-like nanocrystals and -49 mV for nanoplates). These advantages of the brush-like core-antenna nanocrystals are consistent with their higher photocatalytic activity than that of the pure nanoplates and nanorods.

TOB-shaped nanocrystals have a better catalytic performance over nanorods and nanoplates as their size in all the dimensions is between 8.0 to 14.5 nm while the exposed facets are a combination of {001} and {101} facets. Thus, it provides a better platform for improving photocatalytic activity by further seed-mediated growth. After seed-mediated growth, broom-like nanocrystals were produced. According to our analysis, the shape transformation resulted in increase of the size of the core to the range from 9.8 to 19.5 nm and the elimination of {101} facets as well as formation of reactive {100} facets. Similar to the case of brush-like nanocrystals, the epitaxial growth of antenna nanorods also increased the surface area of the nanocrystals and was reflected by the decrease of zeta-potential from -45 mV for TOB nanocrystals to -51 to -57 mV for broom-like nanocrystals. Thus, it is reasonable that the transformation of the core and the evolution of antenna synergistically improved the photocatalytic performance of the nanocrystals in exceeding the performance of commercial P25. From our results, it is also concluded the

best photocatalytic performance can only be achieved when antenna nanorods were in optimized dimensions. When the antenna nanorods were thick and short, the increase of surface area was not extensive. In contrast, when the antenna nanorods were thin and long, it is expected part of the antenna nanorods behaved similar to pure nanorods in photocatalysis since the end of the antenna rods was far from the core-antenna junction, thus decrease the photocatalytic activity.

These results clearly demonstrated that the seed-mediated growth method could provide great opportunities to rationally craft the morphology of TiO_2 nanocrystals into complex core-antenna structures. The dramatically improved photocatalytic activity compared to the nanocrystals with simple structures also proved the significance of the synthetic methodology developed in this work.

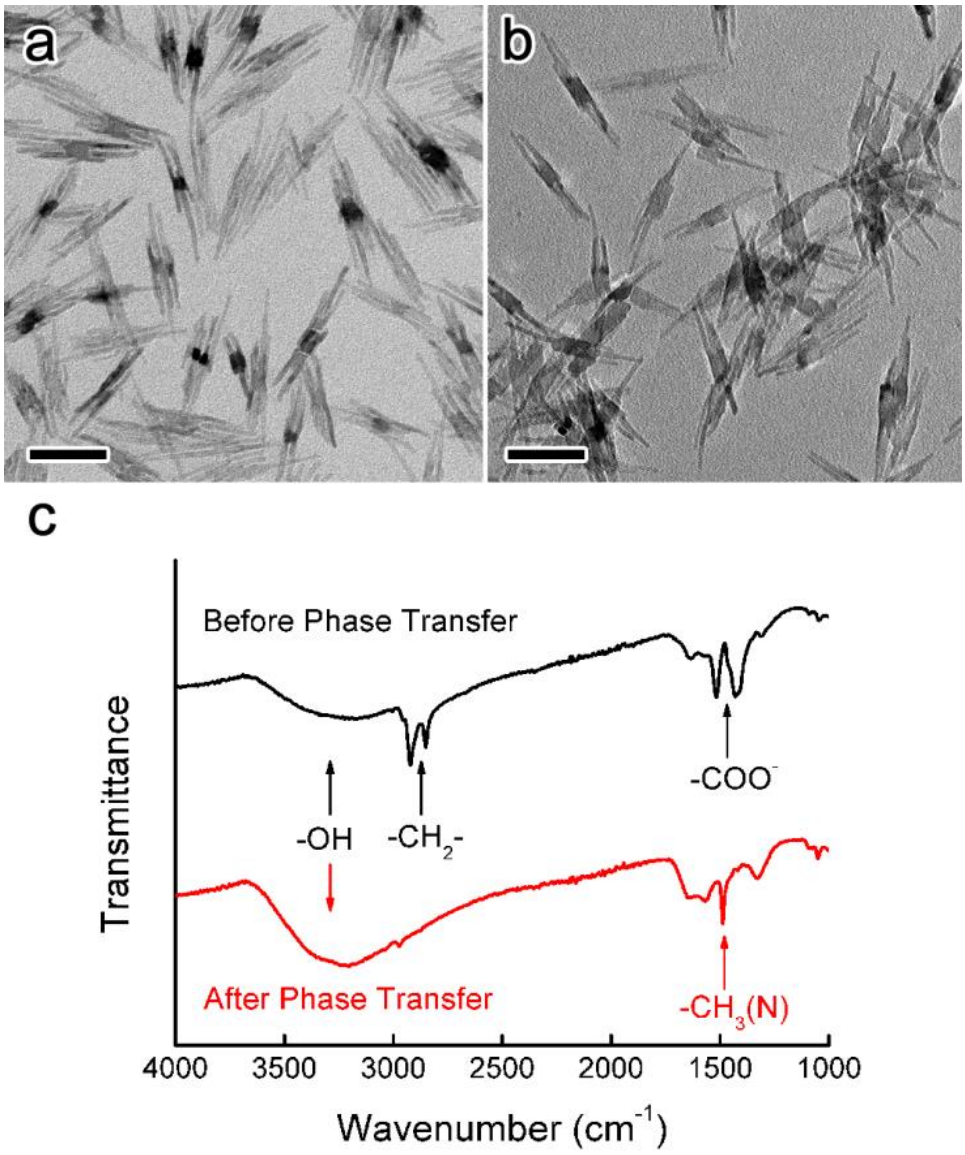

Figure 2.13 Phase transfer of core-antenna nanocrystals (a) TEM image of the typical broom-like nanocrystals prepared with addition of 2.0 mL TBOT at the rate of 3.0 mL/h. (b) TEM image of broom-like nanocrystals after phase transfer to water. Scale bar = 50 nm. (c) FTIR spectra of nanocrystals before and after phase transfer. Reprinted from ref. 167.

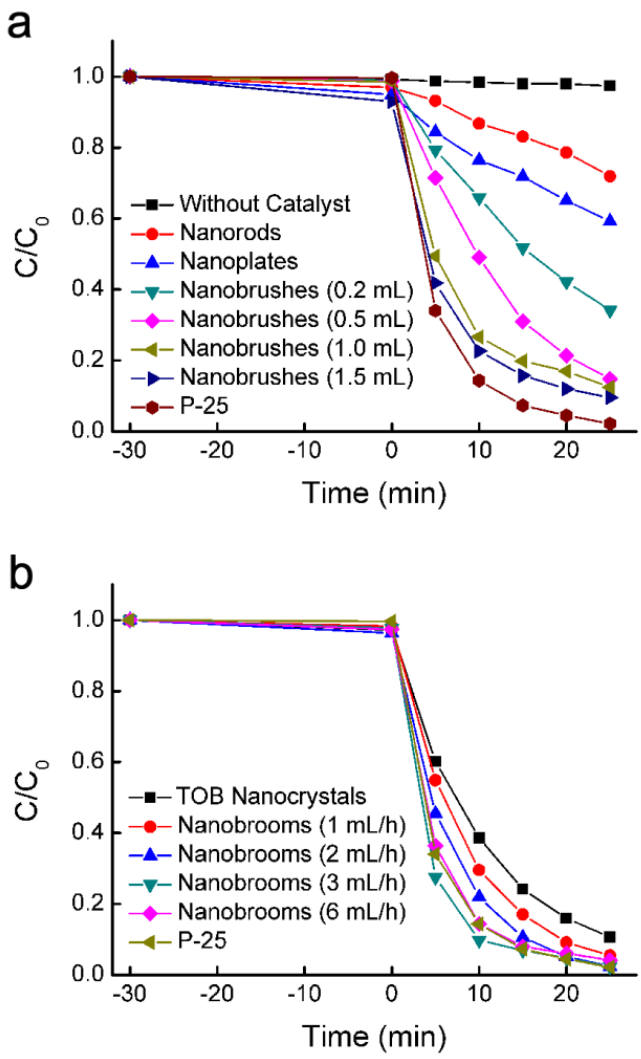

Figure 2.14 The photocatalytic activity of anatase TiO_2 nanocrystals with different morphologies. (a) Change of RhB concentration versus UV irradiation time when nanorods, nanoplates, brush-like TiO_2 nanocrystals synthesized by addition of different amount of TBOT and commercial P25 were used as the catalysts. (b) Change of RhB concentration versus UV irradiation time when TOB nanocrystals, broom-like TiO_2 nanocrystals synthesized by addition of 2 mL of TBOT at different addition rate and commercial P25 were used as the catalysts. Reprinted from ref. 167.

2.6 Conclusions

In summary, a systematic study on shape control synthesis of anatase TiO_2 nanocrystals and their application in photocatalysis has been demonstrated in this chapter. We first realized synthesis of nanocrystals with TOB shape by use of fluoride ions as shape directing agent. With the presence of NaF in the nanorods suspensions in OA, the anatase nanorods can be transformed to faceted octahedral bipyramidal nanocrystals. The crystallinity of the nanocrystals after chemical transformation remained as anatase TiO_2. An etching-redeposition is believed to provide the pathway for the chemical transformation. A combination of NaF and OA at high temperature is expected to produce HF which is capable to etch smaller TiO_2 nanorods and produce titanium molecular species. As the concentration of these molecular monomers increases, they can be redeposited on the larger nanorods and form faceted nanocrystals under the direction of fluorine ions. Fluorine ions can also be employed as shape directing agent during the nucleation and growth of TOB-shaped nanocrystals. In this case, NaF was added to the reaction mixture at the beginning of the synthesis. As the result, TOB-shaped nanocrystals with better size uniformity and larger high energy {001} facets can be produced. The presence of fluorine ions also led to doping of fluorine in anatase TiO_2, which was confirmed by XRD study of the aliquots during the synthesis as well as the characterizations of the products by UV-vis absorption and XPS measurement of the products. The fact of fluorine doping is potentially helpful for improving the photocatalytic activity of the synthesized anatase TiO_2 under visible light irradiation.

In order to create anatase TiO_2 nanocrystals with higher structural complexity in controllable manners, a synthesis strategy based on seed-mediated growth method was developed. In this synthesis, faceted anatase nanocrystals with different shapes were first prepared as seeds. Then, the growth reaction adopted a reaction condition similar to nanorods synthesis but at a lower temperature with the existence of seeds. By using this synthesis method, anatase TiO_2 nanocrystals with core-antenna structures can be synthesized. Structural analysis revealed the growth to be a seed-mediated epitaxial growth along <001> directions and the growth kinetics can further be controlled by changing the reaction parameters such as TBOT introduction rate. By changing the shape of the seeds from TOB-shape to nanorods or nanoplates, the final product of the synthesis can also changes accordingly to elongated nanorods or brush-like nanocrystals. Therefore, theoretically, core-antenna nanocrystals can be tuned to arbitrary morphology by control the shape of seeds and the reaction conditions during the overgrowth.

The developed synthesis strategies towards shape control of anatase TiO_2 nanocrystals enabled production of anatase TiO2 nanocrystals with predictable structures and allowed convenient optimization of their photocatalytic properties. Nanocrystals with different shapes were first transferred to aqueous phase and their photocatalytic performances were evaluated by use photocatalytic oxidation of rhodamine B under UV irradiation as model reaction. It was found the nanocrystals with core-antenna structure showed superior performance than individual cores and antennas and core-antenna nanocrystals synthesized from TOB-shaped seeds and appropriate lengths and diameters showed the best performance which is slightly better than the commercial P25.

We believe our study on the shape control synthesis of anatase TiO_2 nanocrystals could further benefit other TiO_2 nanocrystal-based energy applications such as hybrid and dye-sensitized solar cells by rational design and production of TiO_2 nanostructures with desired morphologies and structural configurations.

Chapter 3

Reversible One-Dimensional Assembly of Charged Gold Nanoparticles and Its Applications

3.1 Introduction

Nobel metal colloidal nanostructures such as gold and silver attracted intensive research interests because of their unique optical properties caused by localized surface plasmon resonance (LSPR).[6, 80, 172-174] Surface plasmon resonances are coherent oscillations of the surface conduction electrons excited by electromagnetic radiation (Figure 3.1a). In the case of light-metal particle interactions, when incident light interacts with particles much smaller than the light wavelength, the conduction electrons can only oscillate locally with a certain frequency known as LSPR due to the confinement of the materials. Consider the optical property of a spherical plasmonic nanoparticle by the classical Mie theory, in the electrostatic dipole regime, the extinction cross section of a metallic particle can be described as[80]:

$$E(\lambda) = \frac{24\pi^2 N a^3 \varepsilon_m^{3/2}}{\lambda \ln(10)} \frac{\varepsilon_i(\lambda)}{(\varepsilon_r(\lambda) + \chi\varepsilon_m)^2 + \varepsilon_i(\lambda)^2} \qquad (3.1)$$

where ε_r and ε_i are the real and imaginary parts of dielectric constant of the particle, ε_m is the dielectric constant of the medium, and a, χ are the size of the particle and shape factor respectively. It is clear that the optical property of plasmonic nanoparticles is strongly

dependent on not only the dielectric properties of both the particles themselves as well as the surroundings, but also the size and shape of the particles.

Noble metal nanostructures with tunable plasmonic properties can benefit various applications. The most widely studied application topics for them include chemical sensing and photothermal therapy.[172, 174, 175] As an example, plasmonic nanoparticles are known to be beneficial for chemical sensing by Raman spectroscopy due to the electromagnetic enhancement of Raman signal.[80, 172, 176, 177] In order to optimize the enhancement effect, plasmon tuning of the nanostructures are needed. It was reported if the LSPR wavelength of the plasmonic nanostructure can be tuned to fall between the Raman excitation and scattering wavelengths, the enhancement can get maximized.[172, 178] In general, there are two types of strategies that can efficiently control the plasmonic properties of noble metal nanostructures – control the size, shape, composition of the nanostructures, or control the assembly of the nanostructures.

Manipulation of plasmonic properties by tuning of the size, shape and composition of noble metal nanostructures has been intensively studied. Gold and silver nanoparticles with controllable size in a large range have been synthesized with different methods and demonstrated tunable UV-vis absorption property.[33, 34, 39] The shape of the nanostructure is even more sensitive than the size change. When the shape of the nanostructures is anisotropic, the surface plasmons are unevenly distributed and the resonance splits into multiple modes.[179, 180] For nanorods, the plasmon resonance splits to a transverse mode and a longitudinal mode. In the case of nanoplates, there exist in-plane and out-of-plane dipolar and quadrupolar modes. Practically, the synthetic

strategies towards these nanostructures have been readily developed and enable production of noble metal nanostructures with controlled plasmonic properties.[20, 48, 70] Naturally, the composition of the plasmonic nanostructures also play an important role in control their plasmonic properties. Recenty, development of synthesis has enabled production of plasmonic nanostructures with multi-component such as core-shell nanostructures and alloys. These nanostructures exhibit novel plasmonic properties that nanostructures with single component cannot be achieved.[181, 182]

Another type of plasmon tuning of noble metal nanostructures is to control the assembly of these nanostructures into ordered structure. As introduced in **Section 1.3**, assembly of nanoparticles into ordered structures will induce collective properties. Particularly for plasmonic nanoparticles such as gold and silver, assemblies of these nanoparticles show distinctive optical properties from individual nanoparticles due to the near field coupling of adjacent particles including shift of plasmonic peaks and generation of "hot-spots" for enhanced Raman scattering.[176, 183-186] Consider the simplest case of two interacting plasmonic nanoparticles. The two nearby dipoles will get coupled and the interaction energy V is depend on the magnitude of dipoles of the two particles p_1, p_2 and the interparticle distance r:[184]

$$V \propto \frac{p_1 p_2}{r^3} \qquad (3.2)$$

When the interparticle distance is small, the interaction energy will be strong and affect the plasmon resonance frequency. When the two dipoles are longitudinally aligned, it corresponds to the lower energy resonance mode and result in the evolution of a strong red-shifted plasmonic peak. When there are more than two interacting particles, the

plasmon coupling becomes more complicated. Theoretically, by control the assembly structure, the optical property of the plasmonic nanoparticles can be manipulated.[184, 187]

Of particular interest is the reversible assembly of such plasmonic nanostructures, which is expected to enable dynamic tuning of the surface plasmon coupling in response to the external stimuli, and therefore produce active optical materials for applications such as color signage, bio- and chemical detection, and environmental sensing.[113, 114, 188-190] However, in spite of extensive studies in the nanoparticle assembly [95, 185, 191-195], it remains a great challenge to develop stimuli responsive assembly and disassembly of colloidal metal nanostructures with reversibly tunable plasmonic properties. In the few available reports for gold nanoparticles (AuNPs), some are designed to respond to pH, [186, 196-198] while others involve thermoresponsive polymers so that the systems are sensitive to temperature variation.[188, 199-201]

From the structural point of view, one-dimensional assembly of nanoparticles is preferred for plasmon tuning as the high anisotropy can amplify the coupling effect and avoid cancelling out of coupling which may happens in isotropic assemblies. As the consequence, a strong coupling plasmon peak can be involved and will enable significant alternation of optical properties.[185, 202-205] In general, the magnitude of coupling gets strong when interparticle distance decreases and chain length increases (Figure 3.1b).[205] Compared to two and three-dimensional assemblies, [206-209] one-dimensional assemblies of isotropic nanoparticles are still only realized in limited cases and the formation mechanism is also not totally clear. It is due to the difficulties arising from

their preparation, which stem from the perception of the isotropic structure and spherical morphology of AuNPs. In the previous cases of one-dimensional assembly of AuNPs, although is still under debate, it is mostly accepted that the linear assembly is the result of a thermodynamic balance between various interparticle attractive and repulsive forces, such as van der Waals attraction and electrostatic repulsion, and it is mainly promoted by the relatively weaker electrostatic repulsion experienced by a AuNP during end-on attachment to an existing nanochain than that of side attachment.[202] The chain length of the assembly can be well controlled by manipulating the electrostatic repulsion through ionic strength and the dielectric constant of the surrounding aqueous media. We also reported recently that when AuNPs capped with bis(p-sulfonatophenyl)-phenylphosphine (BSPP), the one-dimensional assembly process becomes reversible.[210] The linear chain structures of AuNPs form in a solution of water/ethanol mixture and addition of salt, and dissociate after the dilution or evaporation of ethanol. However, the mechanism of the reversibility was not clear until I start the following work on improving the understanding of the process of reversible assembly of charged AuNPs.

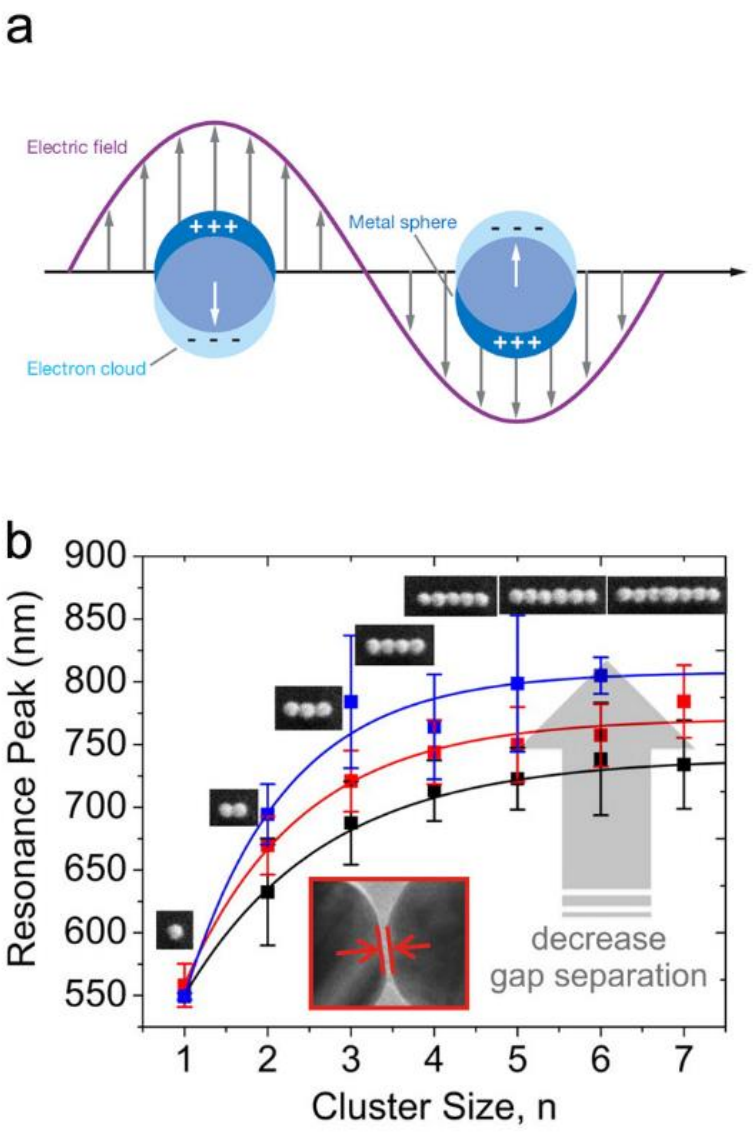

Figure 3.1 (a) Schematic illustration of interactions between light and plasmonic nanoparticles and induced localized surface plasmon resonance (LSPR). (b) The relationship between interparticle distance, chain length and plasmon coupling peak position in one-dimensional assembly of plasmonic nanoparticles. Adapted with permission from ref. 80 and ref. 205.

In this chapter, I will demonstrate a systematic study on theoretical and experimental realization of reversible one-dimensional assembly of charged gold nanoparticles and applications. In **Section 3.3**, I will discuss our theoretical understanding on the thermodynamics and kinetics of the one-dimensional assembly of charged AuNPs capped by BSPP by using thermoresponsive assembly and disassembly of these nanoparticles as a model system. In **Section 3.4**, an example of applications of the reversible assembly of AuNPs will be presented. In this study, gold nanoparticles chains are blended with polymers to form composite films. These films can be used as colorimetric stress memorable sensors as stress can induce the disassembly of the nanoparticle chains in the polymer. A brief summary will be made in **Section 3.5** as the conclusion for this chapter.

3.2 Experimental methods

3.2.1 Chemicals

Chloroauric acid trihydrate ($HAuCl_4 \cdot 3H_2O$, 99.9+ %) was purchased from Acros Organics. Sodium citrate tribasic dihydrate (99%), bis (p-sulfonatophenyl) phenylphosphine dihydrate dipotassium salt (BSPP, 97%), and polyvinylpyrrolidone (PVP360, average mol wt 360,000) were purchased from Sigma-Aldrich. Sodium chloride (NaCl, 99%), Agarose, PEG-400 were from Fisher Scientific. 200-proof ethanol was purchased from Decon Laboratories, Inc. All chemicals were used as purchased without further purification. All solutions were prepared in deionized water (DI water, 18 MΩ·cm) from a Milli-Q water purification system.

3.2.2 Synthesis and ligand exchange of AuNPs

AuNPs were synthesized by following the classic Turkevich method with slight modifications.[211] Briefly, 95 mL of hydrogen tetrachloroaurate trihydrate solution (0.02%, w/w) was heated to reflux with magnetic stirring, followed immediately by addition of 5 mL of fresh trisodium citrate solution (1%, w/w). The aurate-citrate solution was allowed to reflux for approximately 20 min accompanying color change of the solution from pale yellow to wine red. The ligand exchange process was performed after the synthesis. In brief, after the AuNPs solution was cooled down to room temperature, 0.5 mL of 40 mg/mL BSPP aqueous solution was added to the AuNPs solution and then gentlely stirred for overnight. Finally, the AuNPs were washed and collected by centrifugation and redisperse in deionized water. The concentration of the AuNPs solutions was kept at 10 times or 100 times (will be denoted as 10x and 100x AuNPs solution) of the original solution depending on the following experiments. Transmission electron microscopy (TEM) studies were carried out using a Tecnai 12 microscope with an accelerating voltage of 120 kV.

3.2.3 Thermoresponsive assembly and disassembly of AuNPs

Before the reversible assembly process, AuNPs were first mixed with agarose sol. To prepare the AuNP/gel sample, a solution containing 10x AuNPs (100 μL) was mixed sequentially with a BSPP solution (50 μL, 40 mg/ml), an 1 mL of agarose sol with various concentrations preheated at ~70°C, and then a NaCl solution (100 μL) with various concentrations. The mixture was transferred to a plastic cuvette after ensuring the homogeneity. The temperature-controlled reversible assembly and disassembly process

was performed in a temperature-controllable Varian Cary 500 double beam scanning UV-Vis-NIR spectrophotometer using cuvettes with 1 cm optical length. UV-visible (UV-Vis) spectra measurements of samples at different temperature were also collected. The samples were stabilized at defined temperatures (variation < 0.2 ℃) for 10 minutes before each measurement. Zeta potential measurements were performed using Delsa Nano C Particle Analyzer, with sample temperature being stabilized for 10 minutes before each measurement.

3.2.4 Kinetics study

The preparation of AuNPs-agarose mixture was similar as described in 3.2.3 except that the concentration of agarose maintained at 0.05% and the NaCl concentration maintained at 0.09 M. To prepare the sample with different initial stage, for all the experiments, the first step is to treat AuNPs at 40 °C for sufficient time to ensure the AuNPs were fully isolated, and subsequently cooled down to 5 °C with a rate of 2 °C/min and maintained for 5 min. Then, the assemblies were then partially dissociated to by heating the sample at to a desired temperature at the rate of 2 °C/min to obtain the initial stages. The final stage of the path dependent assembly was obtained by re-cooling the sample to 5 °C at the same rate and maintained for another 5 min.

3.2.5 Studies on AuNPs-polymer composite films

Assembly of AuNPs in water-enthanol mixture Assembly of AuNP chains was performed according to our previous work with slight modification. Typically, 3 μL of 1.0 M NaCl aqueous solution and 900 μL of 200 proof ethanol were sequentially added

into a 100x AuNPs stock solution (100 μL). After gentle shaking, the suspension was allowed to stand for 1 h to enable the formation of AuNP chains.

Fabrication of AuNPs-polymer composite films Typically, PVP (0.10 g, M.W. = 360,000) and a desired amount of PEG were carefully mixed with the AuNP chain suspension (1 mL) to form a homogeneous mixture. The mixture was then drop cast onto a polydimethylsiloxane (PDMS) substrate and placed in a vacuum desiccator for 24 hours to allow the evaporation of ethanol. Solid films were then peeled off from the substrate and cut into small pieces of 3 mm^2 with circular shapes using a homemade puncher.

Compression tests Samples were loaded into a pressing die and constant forces were applied onto the die by using a compressor with a force gauge. The pressure applied on the sample was then calculated by dividing the force by the initial sample area.

Characterizations of the composite film Optical absorption profiles of the films were measured using a Varian Cary 50 UV-Vis spectrophotometer. The area change of the sample was determined by taking digital images of the sample before and after the compression test with a ruler to reference the scale followed by measuring the size of the sample from the images. The thickness of the sample was measured using a micrometer.

3.3 Theoretical study on reversible assembly of AuNPs

In this section, the studies on improving the understanding on how to realize reversible assembly of AuNPs and their behaviors will be discussed. As introduced in Chapter 1, the major factor that governs the assembly behavior is the colloidal interactions. Herein, we will start with analysis of the colloidal interactions among

AuNPs. Based on this understanding, design and realization of thermoresponsive assembly and disassembly of AuNPs through the manipulation of the electrostatic interactions by temperature variation, and further show dynamic and reversible tuning of the surface plasmon coupling by controlling the temperature of the solution will be demonstrated. In addition, we will also present our study on the kinetics of the assembly process, which showed uniqueness of the kinetics in reversible assembly compared to those in irreversible ones. We believe we improved the understanding of the process of assembly and disassembly of AuNPs and enabled dynamic tuning of the surface plasmon coupling which is an important step towards the development of functional optical devices based on the interesting surface plasmon resonance of metal nanostructures.

3.3.1 Thermodynamics of reversible assembly of AuNPs[212]

As introduced in **Section 3.1**, although still under debate, it is generally accepted that the one-dimensional assembly of AuNPs is a result of competition of van der Waal attractions and electrostatic repulsions. Under certain circumstances, AuNPs will experience with a weaker electrostatic repulsion during end-on attachment to an existing nanochain than that of side-on attachment. The claim that most likely only the DLVO forces were involved in this case is because there is no direct evidence that AuNPs possess a permanent electric or magnetic dipole. Typically, AuNPs are in isotropic nature and Au-ligand interactions are not likely to break the isotropic symmetry of AuNPs as there is no evidence that the distribution of ligands is uneven.

While the van der Waals attraction mainly depends on the properties of nanoparticles themselves such as density, shape and volume, the electrostatic interaction

depends on not only the surface properties of nanoparticles but also the properties of surroundings such as dielectric constant of solvent, ionic strength, pH, and temperature.[93, 195, 202] By disperse AuNPs in a NaCl aqueous solution with an appropriate concentration, it is expected the nanoparticles assembly and disassembly can be realized by control of temperature as the charge dissociation of divalent BSPP ligand is expected to be dependent on temperature.

Experimentally, negatively charged AuNPs covered with BSPP ligands were synthesized by using the classic citrate reduction method followed by a ligand exchange process. According to the TEM image of AuNPs (Figure 3.2a), the average diameter of the monodispersed AuNPs is 15 nm. Then the AuNPs were dispersed in an aqueous mixture of 0.09 M NaCl and 2 wt% agarose at 70 ℃. Cooling the sample down greatly increased the viscosity of the system and eventually converted the solution into a hydrogel when the temperature is below 40 ℃. By sweeping the temperature in the range of 40-5 ℃, AuNPs can be assembled or disassembled, and show temperature dependent optical properties (Figure 3.3a). The sample at high temperature appeared ruby red, indicating a disassembled state, while at low temperature it turned to dark blue, suggesting a linear chain structures as described in earlier reports.[185, 202, 204, 210] As shown in the temperature dependent extinction spectra in Figure 3.3b, c, when temperature was lowered from 40 ℃, the plasmonic peak originally at ~525 nm gradually decreased in intensity, while a shoulder at longer wavelengths started to develop and eventually evolve into a distinct peak at ~685 nm when the temperature reached 5 ℃. This new peak represents a 1D longitudinal plasmon coupling between AuNPs, revealing

the chain structure of the assemblies.[185, 210, 213] The red-shift of the original 525 nm peak to about 560 nm is most likely because of the irregularity of the chain-like aggregates which results from the high salt concentration in our system.[214] The TEM image of the AuNPs assembly at low temperature prepared by freeze drying (Figure 3.2b) also confirmed the formation of chain structure. When the same sample was heated from 5 ℃ back to 40 ℃, the extinction spectra gradually change to the opposite direction and fully recover the single isotropic surface plasmon band, suggesting the disassembly of the chains into isolated nanoparticles (Figure 3.3c). It should be noted that the assembly and disassembly processes also occur to the AuNP solution containing no agarose. The presence of the agarose hydrogel network, however, helps to limit extensive chain growth, prevent precipitation of the assemblies, and ensure uniform distribution of the AuNPs in the sample, so that a consistent optical tuning can be achieved and recorded.[215, 216]

To investigate the stability and reversibility of the system, a similar sample was prepared and cycled 9 times between 5 ℃ and 40 ℃. As shown in Figure 3.4a, the recorded spectra essentially show two bands of nearly-overlapped curves correspond to extinction profiles at high and low temperatures respectively. Figure 3.4b plots the peak positions of the coupled surface plasmon band at 5 ℃ and the isotropic surface plasmon band at 40 ℃, further demonstrating the complete reversibility of the thermoresponsive optical switching. Compared to the pH-responsive assembly systems, our system shows an impressive reversibility and reproducibility.[196, 198]

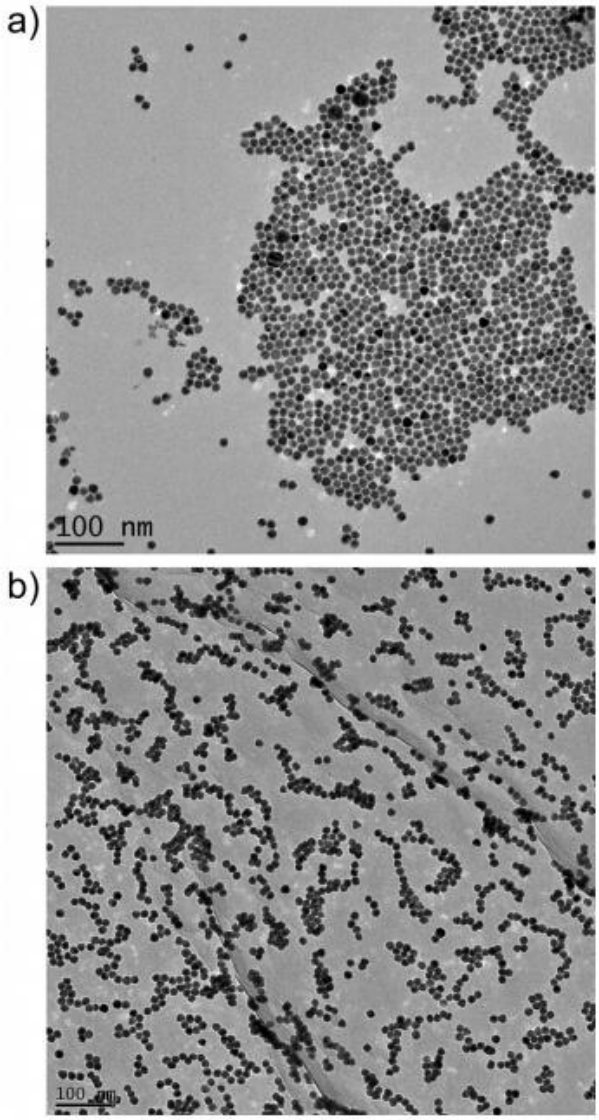

Figure 3.2 TEM images of (a) the as-synthesized charged AuNPs and (b) the chain-like AuNP assemblies prepared at 5°C in the presence of salt. To prepare the TEM sample of (b), a drop of AuNP assembly solution was supported on a carbon coated copper grid and then freeze-dried at a low temperature achieved using dry ice. Reprinted with permission from ref. 212.

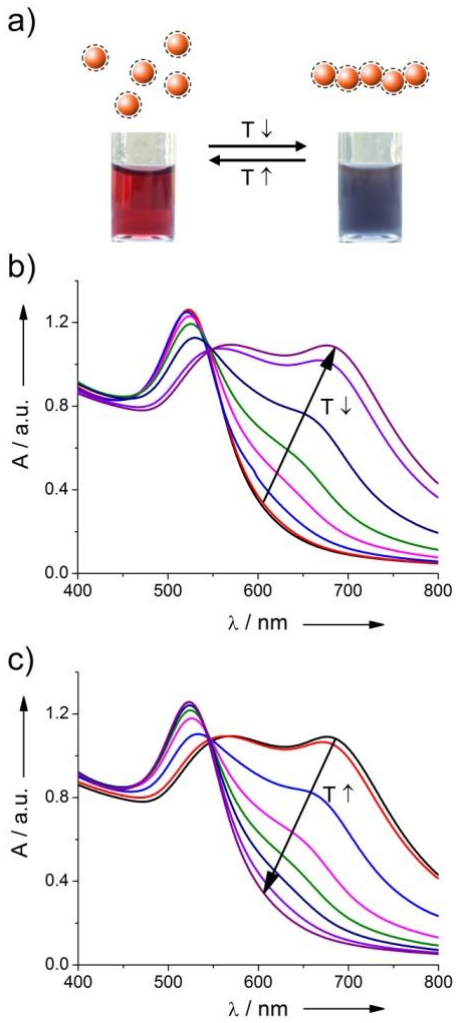

Figure 3.3 The thermoresponsive tuning of plasmonic properties of charged colloidal AuNPs: (a) schematic illustration and photos showing AuNPs switching between the disassembled and assembled states in response to temperature changes, (b) the extinction spectra of a typical AuNP dispersion when cooled from 40 ℃ to 5 ℃, and (c) the extinction spectra of the same sample when heated from 5 ℃ back to 40 ℃. There is a 5 ℃ temperature difference between each neighboring spectrum. Reprinted with permission from ref. 212.

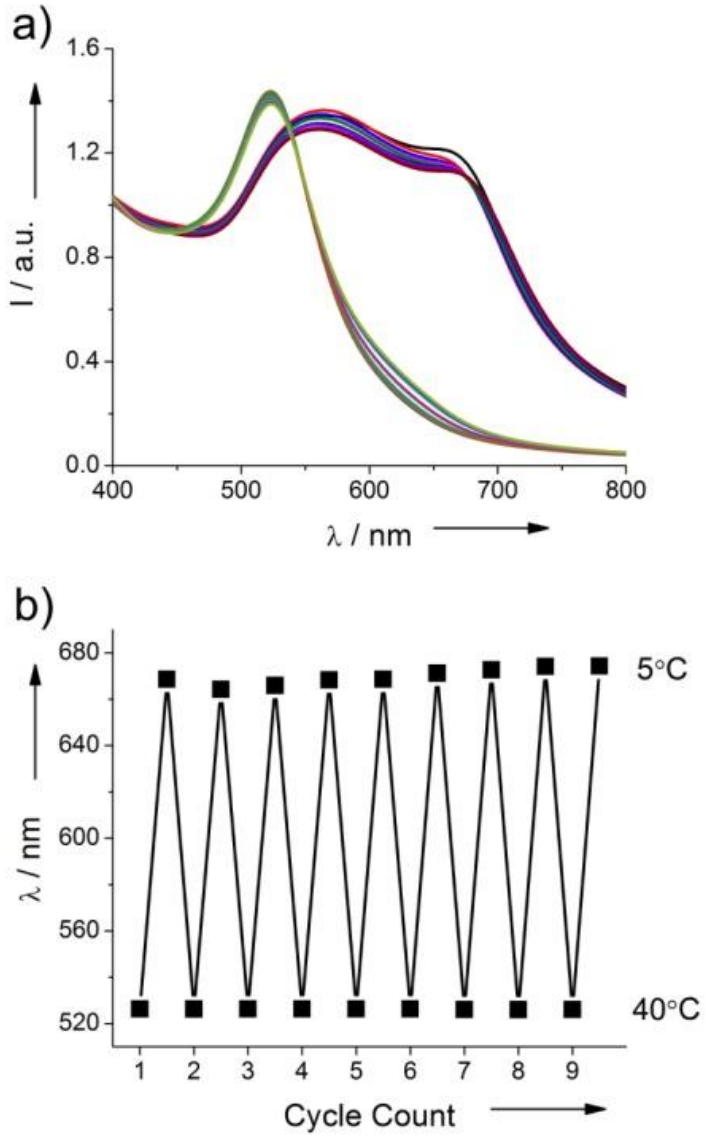

Figure 3.4 (a) The extinction spectra of a typical AuNP dispersion during 9 cycles of repeated heating (at 40 ℃) and cooling (at 5 ℃). (b) The repeated switching of plasmonic peak positions (isotropic peak at 40 ℃ and coupling peak at 5 ℃) for nine cycles. Reprinted with permission from ref. 212.

Theoretically, whether nanoparticles are in assembled or disassembled states as well as the reversibility of nanoparticle assemblies should be determinable by examining the interparticle energy diagrams under specific conditions. If the interparticle energy minimum appears at a short interparticle distance, the assembled state is thermodynamically preferable; otherwise, the disassembled state is preferred.[93, 217] In this case, the total interaction energy of two interacting nanoparticles is the sum of electrostatic energy V_{elec}, van der Waals potential energy V_{vdW} and short-range repulsion energy V_{SR}.[93, 202, 218]

$$V_{TOT} = V_{elec} + V_{vdW} + V_{SR} \qquad (3.3)$$

If we assume the particles are spherical, and consider the surface layer (ligand layer as well as hydration layer) with an average thickness of d, then the electrostatic interaction energy should be:

$$V_{elec} = 2\pi\varepsilon_s\varepsilon_0(a+d)\psi_0^2(T)\ln(1+\exp(-(r-2a-2d)\kappa)) \qquad (3.4)$$

where $\varepsilon_s\varepsilon_0$ is the dielectric constant of the solvent, a is the the radius of the nanoparticle core, ψ_0 is the surface potential of the particle, T is absolute temperature, r is the distance between the neighboring particle centers.κ^{-1} is the Debye length which can be described as:

$$\kappa^{-1} = \frac{\varepsilon_s\varepsilon_0 k_B T}{2000\, e^2 N_A I} \qquad (3.5)$$

The van der Waals attraction should include 1) gold-gold, 2) gold-surface layer and 3) surface-surface interactions, in which the last two parts can be neglected if the surface layer is relatively thin.

$$V_{vdW} = V_{Au-Au} + 2V_{Au-Sur} + V_{Sur-Sur} \approx V_{Au-Au} \quad (3.6)$$

$$V_{Au-Au} = -\frac{A_{Au-H_2O-Au}}{6}\left(\frac{2}{R^2-4} + \frac{2}{R^2} + \ln\frac{R^2-4}{R^2}\right) \quad (3.7)$$

$A_{Au-H_2O-Au} = 3\times10^{-19}\,J$ is the Hamaker coefficient of interacting gold nanoparticles in water[219] and $R = r/a$.

Combining the two major interactions commonly considered in the Derjaguin–Landau–Verwey–Overbeek (DLVO) theory results in a net potential that is predicted to approach a value of negative infinity upon particle contact.[93, 218] Apparently, such an infinitely deep primary minimum is not consistent with the reversible assembly observed in this study.[220] Consider the sterically bulky structure of the BSPP ligands as well as the hydration force experienced by the interacting AuNPs, it is reasonable that short range repulsive interactions cannot be neglected when nanoparticles are begin to contact with each other and prevent the formation of infinitely deep primary minimum in the energy diagram.[221]. Without referring to the precise details of the short-range forces, we find it convenient to resort to the mean Born potential formulation developed previously for the examination of reversible coagulation or adsorption phenomena, as shown in Equation (3.8)

$$V_{SR} = 4A_S\left(\frac{\sigma_c}{a}\right)^6\left(\frac{4!}{10!}\right)\frac{1}{R}\left(\frac{R^2-14R+54}{(R-2)^7} + \frac{-2R^2+60}{R^7} + \frac{R^2+14R+54}{(R+2)^7}\right) \quad (3.8)$$

in which σ_c is the collision diameter with a typical value of 0.5 nm[218, 222] and A_S is the Hamaker coefficient of interacting surface layer in water and is assumed to be the same as the Hamaker coefficient of a typical hydrocarbon polymer: polystyrene in water

which is $1.3\times10^{-20}\,J$. The contribution from the gold-gold interactions can be neglected in this type of interactions due to the short range nature.

According to Equation 3.4 and 3.5, electrostatic interaction is mainly affected by temperature, Debye length, dielectric constant of the solvent and particle surface potential. The first three parameters can be directly obtained or derived, while the particle surface potential in solutions with defined ionic strength and temperatures can be measured. Figure 3.5a shows the zeta potential values for AuNPs dispersed in a 0.09 M NaCl solution at four different temperatures, which was found to change from -64.3 mV to -43.3 mV with the decrease in temperature from 40 ℃ to 10 ℃. The nearly linear increase in the magnitude of zeta potential with temperature is consistent with the results reported in literature, and it is often attributed to the changes in surface adsorption/desorption equilibrium, charge dissociation equilibrium, and the diffuse double-layer thickness.[223-226] Our calculation shows that the change in zeta potential with temperature leads to a prominent change of electrostatic energy. With an assumed ligand layer thickness of 0.5 nm, Figure 3.5b plots the total interaction energy vs. interparticle distance, as calculated according to Equations 3.3 – 3.8. The energy diagrams show obvious differences for cases at different temperatures. The primary energy maximum, which plays a role as an energy barrier for the assembly process, gradually vanishes with decreasing temperature. At the same time, an energy well at ~1.3 nm gradually evolves, which is in favor of a stable assembled state. This result is in agreement with experimental observations that a disassembled or isolated state is energetically favored for AuNPs at higher temperatures such as 40 ℃; while at low

temperatures such as 10 ℃ or lower, AuNPs can stay in the assembled state due to the presence of the well-defined energy well. Meanwhile, the considerably shallow energy well at low temperatures (< 4 kT) is critical for the reversible assembly-disassembly processes.[227]

As the ionic strength of the solution has a profound effect on electrostatic interactions, it is expected the salt concentration plays an important role in governing the particle interaction energy and therefore the assembly behavior. Figure 3.6 compares the extinction spectra of the samples with lower (0.05 M) and higher (0.13 M) NaCl concentrations relative to the typical value (0.09 M) that we tested. At a low salt concentration, no extensive assembly of AuNPs occurred, resulting in a coupling absorption band that appeared only as a shoulder even at 5 ℃. At a high salt concentration, assembly of AuNPs was difficult to prevent, with a coupling absorption band prominent even at high temperatures such as 40 ℃. The zeta potential of the nanoparticles dispersed in these two different salt concentrations at different temperatures also changes accordingly. When NaCl concentration was at 0.05 M, the value of zeta potential of the nanoparticles slightly increased compared to the typical case, ranging from -44 mV to – 66 mV between 10 ℃ and 40 ℃. In contrast, when NaCl concentration increased to 0.13 M, the value of zeta potential of the nanoparticles decreased compared to the typical case, ranging from -39 mV to – 58 mV between 10 ℃ and 40 ℃. Calculation of the particle interaction energy for the case of low salt concentrations by using the measured zeta potential values suggests that even though distinct energy wells form throughout the entire temperature range, the overall positive interaction energy and

the high primary energy maximum make it difficult to form assemblies (Figure 3.6c). In the case of high salt concentrations, a small interparticle distance is energetically preferable, as suggested by the considerably deep energy wells in the calculated particle interaction energy diagram in Figure 3.6d, suggesting a significantly higher tendency to assemble.

The concentrations of both nanoparticles and agarose have been found to affect the extent of the AuNP assembly and consequently the plasmonic properties (Figure 3.7). When other parameters are fixed, the variation in the concentration of AuNPs changes the average size of the assemblies, as expected from the mass action kinetic analysis.[228] When assembled at 5 ℃, the coupled plasmonic peak red shifts more and show continuously increasing intensity at higher AuNP concentrations. The concentration of agarose does not significantly affect the optical property of the AuNPs in the disassembled form at high temperatures, however, it changes the average chain length during the assembly of AuNPs because the gel density determines the local availability of AuNPs. As a result, the coupled plasmonic peak shifts to longer wavelengths when the particles are assembled at 5 ℃ in a diluted agarose solution. Because a higher agarose concentration is beneficial to maintaining the stability of AuNP assemblies against precipitation from the solution, we found 2 wt% to be a good compromise between the plasmon shift and the stability against precipitation.

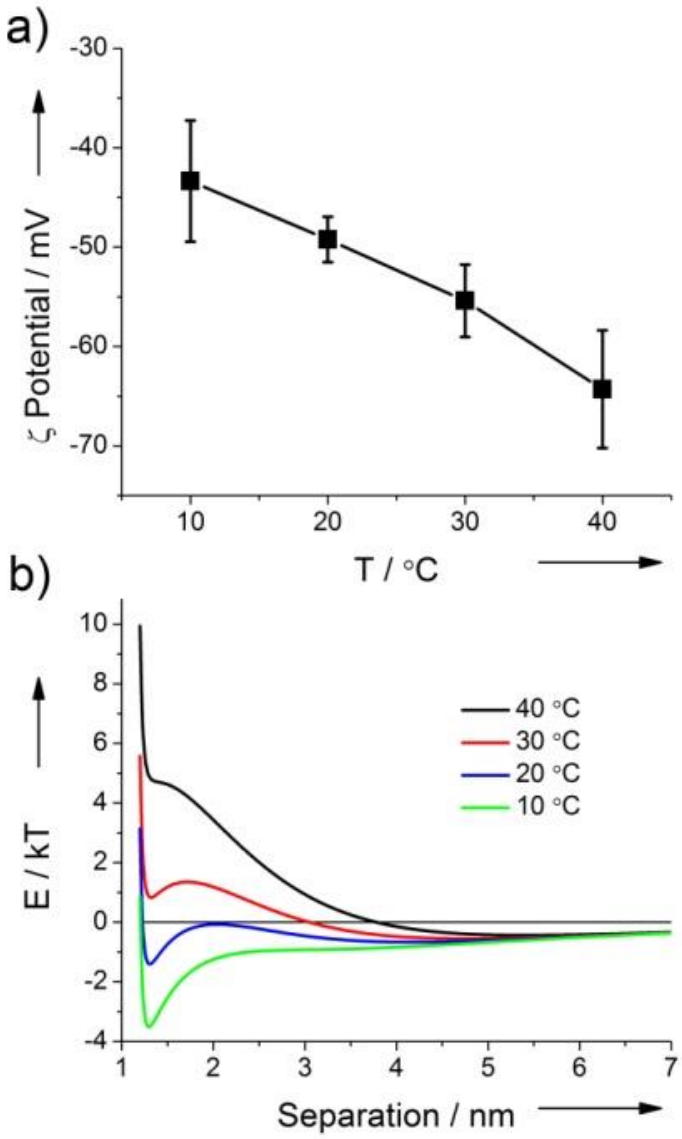

Figure 3.5 (a) Zeta potential vs. temperature plotted for colloidal AuNPs in 0.09 M NaCl aqueous solution. (b) Interparticle energy vs. interparticle distance plot of AuNPs in 0.09 M NaCl aqueous solution. Reprinted with permission from ref. 212.

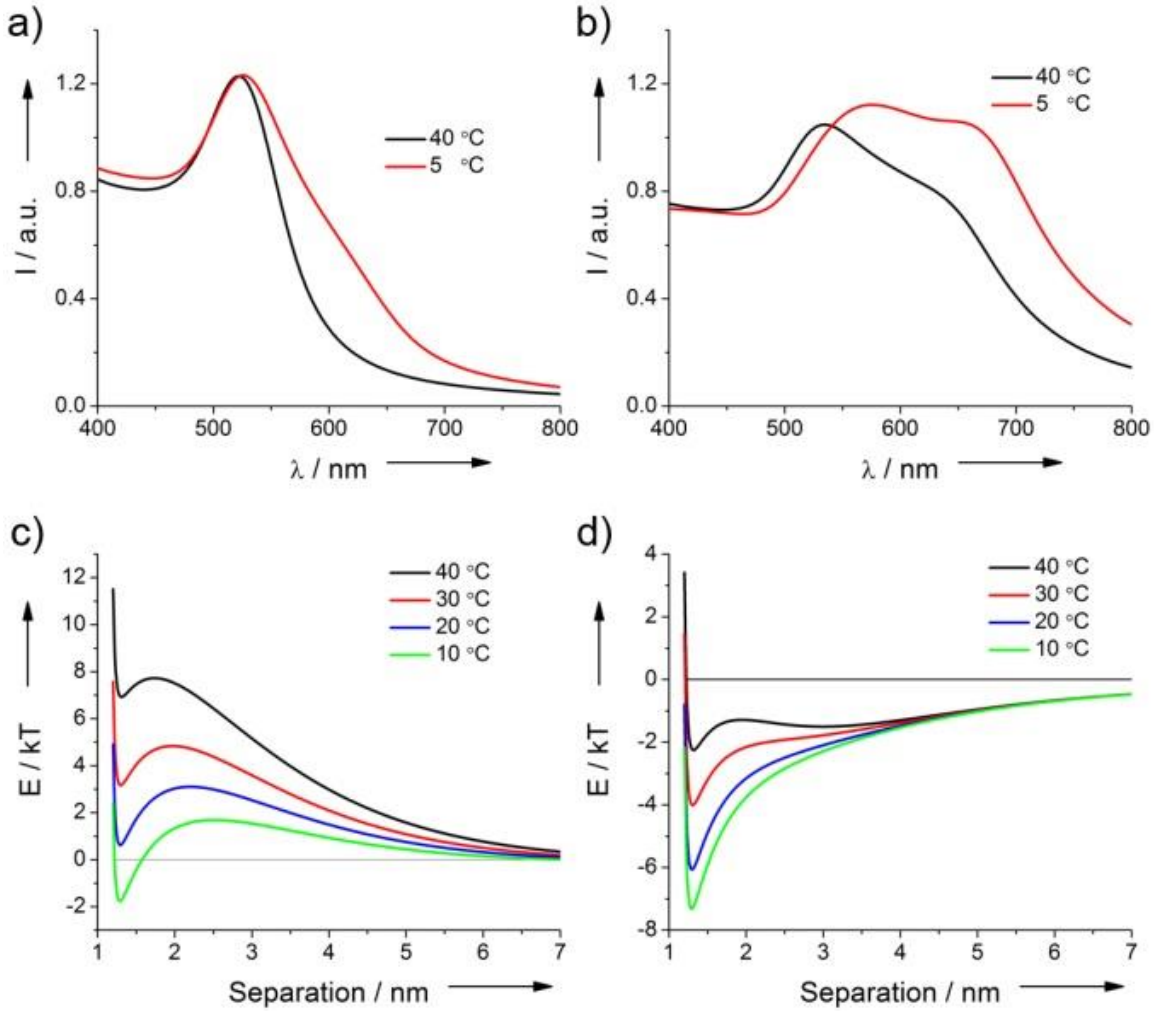

Figure 3.6 The extinction spectra measured at 40 ℃ and 5 ℃ for AuNP dispersions containing (a) 0.05 M and (b) 0.13 M of NaCl, and the plots showing the interparticle energy vs. separation calculated for various temperatures for AuNP dispersions containing (c) 0.05 M and (d) 0.13 M of NaCl. Reprinted with permission from ref. 212.

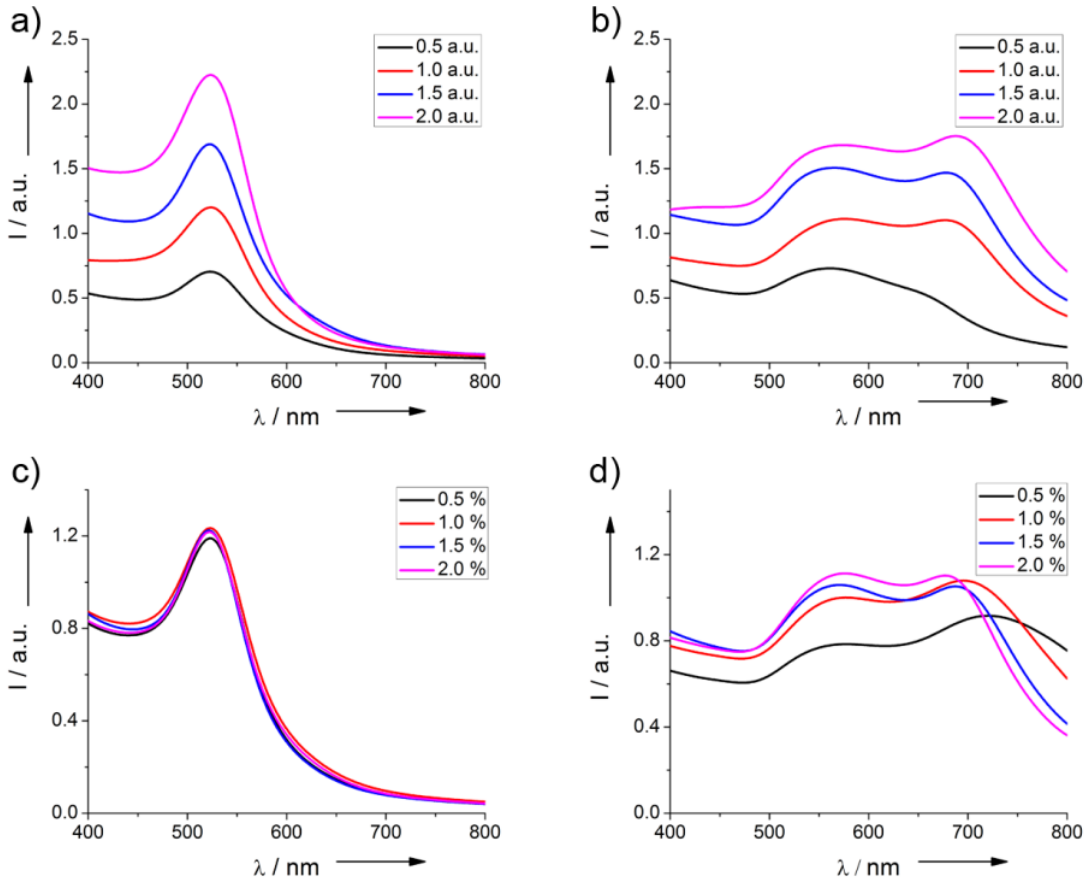

Figure 3.7 (a, b) The extinction spectra of samples with different AuNPs concentration at (a) 40 ℃ and (b) 5 ℃. (c, d) The extinction spectra of samples with different agarose concentration at (c) 40 ℃ and (d) 5 ℃. Reprinted with permission from ref. 212.

3.3.2 Kinetics of reversible assembly of AuNPs[229]

Due to the reversibility of the assembly process, the assembly kinetics is also unique compared to irreversible assemblies. Typically, the kinetics of irreversible one-dimensional assembly of colloidal nanoparticles is comparable to step-growth or chain growth of linear polymer.[123, 230] However, we found the kinetics of reversible assembly is comparable to the kinetics of nucleation and growth of nanocrystal. In this case, isolated AuNPs are acting as the monomers in the nanocrystal synthesis, while assembled structures can be analogue to the nuclei.

To experimentally investigate the kinetics of the assembly process, AuNPs were reversibly assembled and disassembled in designed pathways. When agarose concentration decreased to a low level, the optical property of the nanoparticle assemblies shows temperature path dependent property. Under this condition, assembly of AuNPs was not significantly limited by the agarose matrix, and it is expected AuNPs would not stick to one nanoparticle chain during the reversible assembly process and macroscopically, there should exist path dependent optical property due to the reconfiguration of nanochains during the process.

In the experiment, heating and cooling were used to drive the assembly and disassembly kinetics. When the assembly was starting from fully isolated AuNPs (continuously decrease temperature from 40 ℃ to 5 ℃ at a constant rate), the optical absorption of the final assemblies show a strong coupling peak at 775 nm. By sweeping the temperature from 40 ℃ to 5 ℃ for several cycles, it is confirmed the optical properties of the assemblies at 5 ℃ kept as the same (Figure 3.8b). However, if the

assembly process was started from partial disassembled states (first partially disassemble the assemblies at 5 ℃ by increasing the temperature to a moderate value and restart the assembly process by cooling down the sample to 5 ℃ again), the optical properties of the AuNPs assembly are different from each other depend on to starting temperature (Figure 3.8c). This is due to the different amount of "monomers" and "nuclei" at the initial state. When concentration of isolated AuNPs is low (e.g. start assembly from 20 ℃), at the final stage, the absorption of the AuNP assembly showed a red-shift of the coupling peak (810 nm) compared to the typical assembly starting from fully isolated AuNPs (775 nm), which indicate an increase in average chain length of the assembly.[187] In comparison, at a relative higher "monomer" concentration (e.g. start assembly from 26 ℃ or 32 ℃), after extensive assembly, the absorption spectrum showed a blue shift of the coupling peak (735 nm and 755 nm for assembly start from 26 ℃ and 32 ℃ respectively) while the peak also became asymmetric. It indicated under this condition, the average chain length of the nanoparticle assembly decreases and there exist more than one peak in the size distribution. We also use dynamic light scattering measurements to qualititively estimate the average chain length of the assembly and the results were consistent with the conclusion made from the interpretation of the optical absorption spectra. The assembly produced by decreasing temperature from 40 ℃ showed a single distribution peak with an average at 350 nm, the assembly started from 20 ℃ also showed one peak with the average at 617 nm. However, the assembly prepared by decreasing temperature from 26 ℃ showed two distribution peaks with peak position at 47 nm and 330 nm.

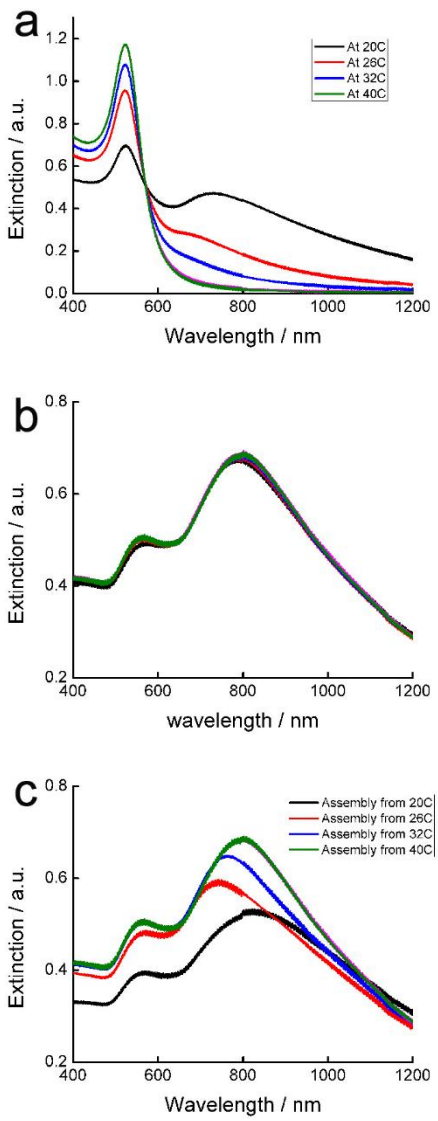

Figure 3.8 Temperature path-dependence in thermoresponsive assembly. (a) The initial state of the assembly process. Initially, nanoparticles are at different temperatures. At higher temperature, more isolated particles and fewer aggregates and vice versa. (b) Final states of the assembly repeatedly start from 40 °C, show nearly identical optical properties. (c) Final states of the assembly started from different temperature, show distinctive different optical properties. Reprinted from ref. 229.

These results provided us clear hint on the kinetics of both the assembly and disassembly processes. When the assembly is starting from a homogeneous suspension of isolated AuNPs, the products should be one-dimensional assemblies with a finite chain length distribution, which is similar to nucleation and growth of nanocrystals in which the products are nanocrystals with a finite size distribution. During the disassembly process, it is expected smaller assemblies are easier to dissociate due to a weaker attractions compared to larger assemblies. When there is only a slight increase in temperature, small assemblies are disassembled first and results in the co-existence of larger assemblies and a relative small amount of isolated AuNPs. If the assembly process is started from this condition, isolated particles are more likely to attach to existing assemblies due to the low concentration and finally produce assemblies with larger size. As the result, the coupling peak of the AuNPs assemblies shows a red shift compared to the typical case. This process is comparable to the ripening process in the nanocrystal synthesis.[15] In the ripening process, nanocrystal growth is under a low monomer concentration during which self-nucleation is inhibited. As the consequence, growth of nanocrystals is enabled through dissolution small nanoparticles and redeposition of the monomers on larger particles. If the temperature goes to a higher degree, a larger extent of disassembly will occur which will not only destroy small assemblies but also lead to the dissociation of larger assemblies. Starting the assembly process from a higher isolated AuNPs concentration and smaller assemblies, the size distribution of the final assembly should show two peaks as isolated AuNPs have a higher tendency to self-assembled to smaller assemblies due to the high “monomer” concentration and a lower tendency to attach to

existing assembled due to the reduced amount of assemblies, which results in the evolution of a new peak in size distribution and also the blue shift of the coupling peak.

3.4 Colorimetric stress memory sensor based on disassembly of gold nanoparticle chains[231]

In the last section, we have demonstrated our understanding on the mechanism of reversible one-dimensional assembly and disassembly of charged AuNPs by systematically investigated the thermodynamics and kinetics of this process. In this section, we will present use of this reversible assembly process in practical applications by taking advantage of the ability of disassembly which is not possible to be realized in typical plasmonic nanoparticle assemblies. In particular, we here demonstrate an AuNP chain–polymer composite film which shows a colorimetric response to mechanical forces and can "memorize" the stress it has experienced. Our design takes advantage of the intensity and time dependent viscous flow of polymeric materials in response to mechanical stress.[232] Such deformation leads to the disassembly of embedded AuNP chains and causes a shift of the plasmonic band, which can be correlated to the applied mechanical stress.

Figure 3.9 illustrates the working principle. AuNP chains are first homogeneously mixed with a polymer solution and then cast in a solid composite film. After being subjected to sufficient pressure for a certain period of time, the composite film is irreversibly deformed. By treating viscoelastic polymers as governed by the Kelvin-Voigt Model and regarding the viscous component as an ideal dashpot which

obeys Newton's law of viscosity, we obtain the relationship between the stress and irreversible viscous deformation:

$$\varepsilon(t_0) = \int_0^{t_0} \frac{\sigma(t)}{\eta} dt \qquad (3.7)$$

in which the extent of deformation ε is proportional to the intensity of applied stress σ and its duration time t_0, and is inversely proportional to the viscosity of the material η. During film deformation, the homogeneously embedded AuNP chains are stretched accordingly, resulting in an increase of the interparticle distance, a weakening of the plasmon coupling, and a change in the overall color of the film. The recorded position of the plasmon band can be then correlated to the extent of film deformation, which is proportional to the stress that has been applied, thus producing a stress memory colorimetric sensor.

Figure 3.10a outlines the procedure for fabricating the AuNP chain-polymer composite film. Citrate-capped AuNPs with a size of about 15 nm were still synthesized by a slightly modified Turkevich method. A ligand exchange process was then performed to introduce bis(p-sulfonatophenyl)-phenylphosphine (BSPP), a stronger ligand compared to citrate, to the surface of the AuNPs. BSPP-capped AuNPs were then assembled into linear chains in ethanol by adding a trace amount of NaCl, changing the solution color from ruby red to blue. NaCl addition increased the ionic strength of the solution, resulting in the screening of the electrostatic repulsion between particles and triggering the assembly. Polyvinylpyrrolidone (PVP, M.W. = 360,000) was then dissolved in the solution of AuNP chains to form a viscous suspension, which was finally cast onto a

glass substrate to produce a composite film after slow removal of the solvent by evaporation. PVP with high molecular weight was chosen as the polymer matrix due to its high solubility in water and ethanol, low optical absorption in visible range, and its ability to form good films. It also acts as an additional capping agent for the AuNPs and ensures their homogeneous dispersion in the matrix without significant disturbance to the chain structure.[33, 57] More importantly, as discussed later, the adhesion arising from the coordinate bonding between pyrrolidone groups and the Au surface facilitates the disassembly of the AuNPs during the deformation of the PVP matrix.

Similar to solutions of AuNP chains, the AuNP-PVP composite film displays a deep blue color. Its visible light absorption spectrum presents a strong coupling peak at 650 nm, which demonstrates that the AuNPs maintain the chain structure in the composite (Figure 3.10b). The films were very stable, as the color and the optical extinction profile remained nearly unchanged after 30 days of storage at 4 ℃ at 50% humidity. To perform compression test, composite films were first cut into small pieces with circular shape by using a home-made puncher. These pieces of films have a same initial area of 3 mm^2 and initial thickness of 0.25 mm. Samples were then loaded into a pressing die and constant forces were applied onto the die by using a compressor with a force gauge. The initial pressure applied on the sample was then calculated by dividing the force by the initial sample area. After applying a strong pressure (i.e. 1.6×10^5 psi) to the film for 1 min, its color clearly changed from blue to ruby red. The visible extinction spectrum of the composite film after pressing displays a single absorption peak with a small shoulder at around 530 nm, which corresponds to the transverse mode of the

plasmon resonance (Figure 3.10b). To exclude the effect resulting from the shape change of AuNPs during pressing, we compared the extinction profile and morphology of the AuNPs recovered from the films before and after pressing, by first dissolving the films in water and then taking optical and TEM measurements. The extinction profiles of the AuNPs recovered from both films are nearly identical and show a characteristic absorption peak for isolated AuNPs at around 520 nm (Figure 3.10c), while the TEM images also confirm the unchanged morphologies of AuNPs after pressing. In addition, we also performed pressing tests on films containing only isolated AuNPs and found no change in the position of the plasmon band before and after pressing.

As indicated in Equation 1, at a fixed viscosity, which is determined intrinsically by the polymer matrix, the irreversible viscous deformation of the composite film is expected to increase with respect to an increase in the intensity and duration of the applied stress. Accordingly, disassembly of AuNP chains should occur due to the considerably strong adhesion between PVP and the AuNPs, leading to a color shift of the film in response to the changes in these two parameters. To verify this assumption, we first applied different pressures (7×10^3, 1.6×10^4, 4.3×10^4, 8.6×10^4, and 1.6×10^5 psi) to a batch of composite films for the same period of time (1 min). After pressing, the change in optical property and the deformation of the films were investigated. As expected, the plasmon coupling band generally blue-shifted and dampened with increasing applied pressure (Figure 3.11a). Under a relatively high pressure, the coupling peak became indistinguishable and overlapped with the isotropic plasmon band of isolated AuNPs at around 530 nm. To unambiguously measure the changes in the plasmon band positions,

we analyzed the spectra by virtue of continuous wavelet transform (CWT, details not shown), which has been demonstrated to be a powerful and reliable method for analysis of overlapping signals.[233] By applying the transformation, the spectra reveal a clearer trend in the optical change of the films (Figure 3.11b). As shown in Figure 3.11c, the area of the film expanded with increasing pressure to become 61% greater than originally, while the thickness decreased by 42%. As a result, the density of the film was enhanced slightly (< 8%) upon the application of a small amount of pressure, but remained nearly unchanged at higher pressures. The initial density increase may be primarily attributed to the elastic deformation of the polymer film under a mild pressure. Figure 3.11d plots the dependence of the coupling peak position on the pressure applied on the film for fixed amounts of time. In general, the extent of the blue shift and dampening of the coupling peak increase with greater film deformation, which is consistent with our theoretical considerations: more deformation causes a larger displacement of the AuNPs and enhances the interparticle separation, which promotes a larger plasmon band shift. Interestingly, however, it is noted that when a mild stress is applied for a relatively short period of time (e.g. 7×10^3 psi for 1 min), the coupling peak surprisingly red-shifts from 649 nm to 664 nm. We attribute this red-shift to compression of the nanoparticle chains, which occurs at the early stages of pressing as the polymer deformation shows more significant vertical compression (-3.7% change in thickness) and less lateral expansion (2.4% change in area). The compaction of the film reduces the average interparticle distance and at the same time enhances the degree of one-dimensional order within each AuNP chain, leading to stronger coupling at longer

wavelengths.[234] As discussed in Section 3.3, BSPP is a bulky capping ligand which binds to the surface of AuNPs strongly and prevents their permanent aggregation through electrostatic repulsion. When the film is initially compressed, the AuNPs within each chain move closer to each other due to a combined effect of elastic and inelastic deformation, as countered by the increased electrostatic as well as steric interactions. At higher pressures, inelastic deformation dominates so that the band attributed to plasmonic coupling continues to blue shift as more polymer flow occurs in the lateral dimension. It is worth noting that the band at ~530 nm also slightly red shifts, indicating the formation of an increasing number of isolated AuNPs after compression at higher pressures. When keeping the applied pressure constant and prolonging the stress application time from 1 min to 5 min, we found that the coupling peak blue shifts more significantly, as shown in Figure 3.11d. Even under a mild constant pressure, a large band shift and consequently dramatic color change can be observed. These observations are all consistent with our theoretical considerations.

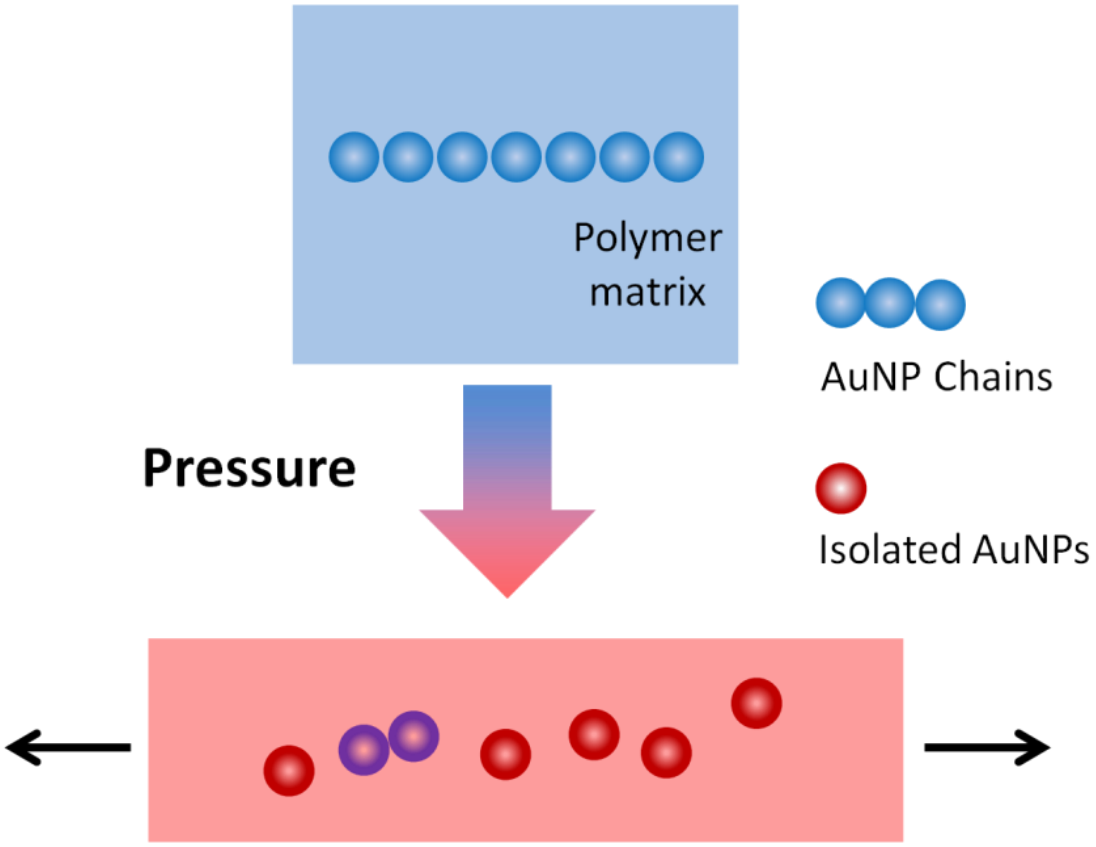

Figure 3.9 Schematic illustration of the design of the stress-responsive colorimetric film based on disassembly of gold nanoparticle chains in a polymer flow. Reprinted with permission from ref. 231.

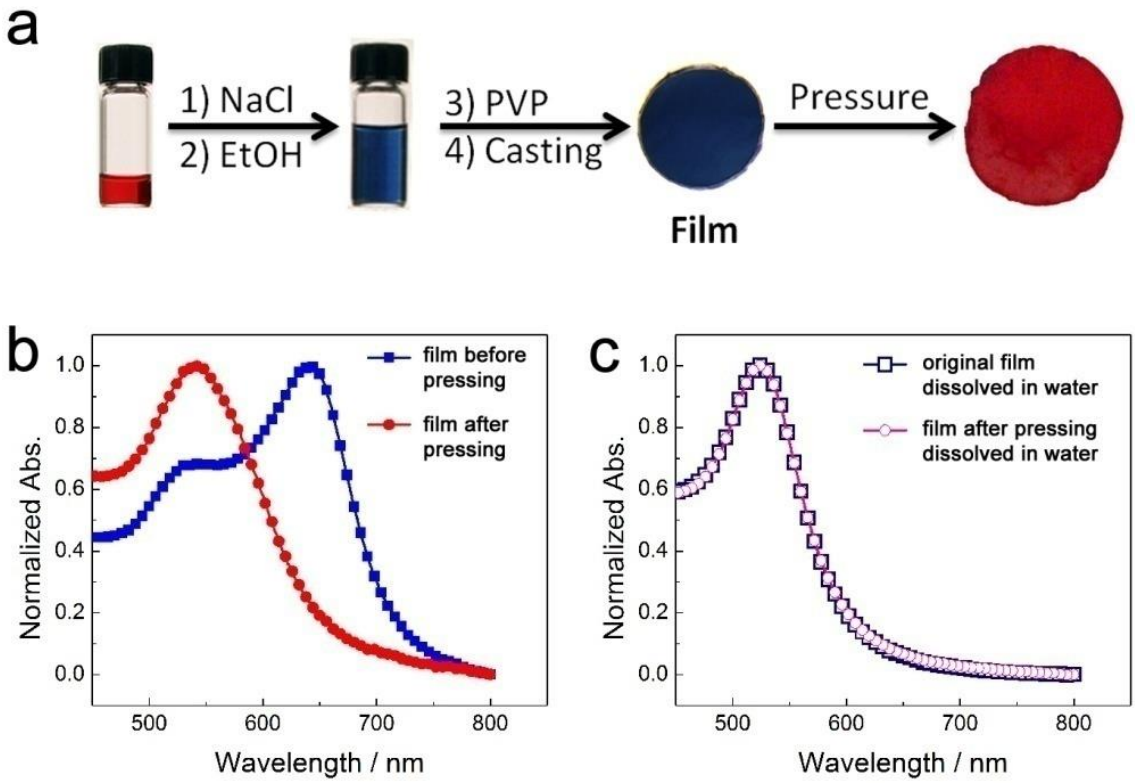

Figure 3.10 Fabrication of the composite film and its pressure-responsive color switching performance. (a) Illustration of film fabrication procedure and compression test results. (b, c) Normalized UV-Vis extinction profiles for films before/after pressing (b) and the nanoparticle suspensions recovered from both films (c). Reprinted with permission from ref. 231.

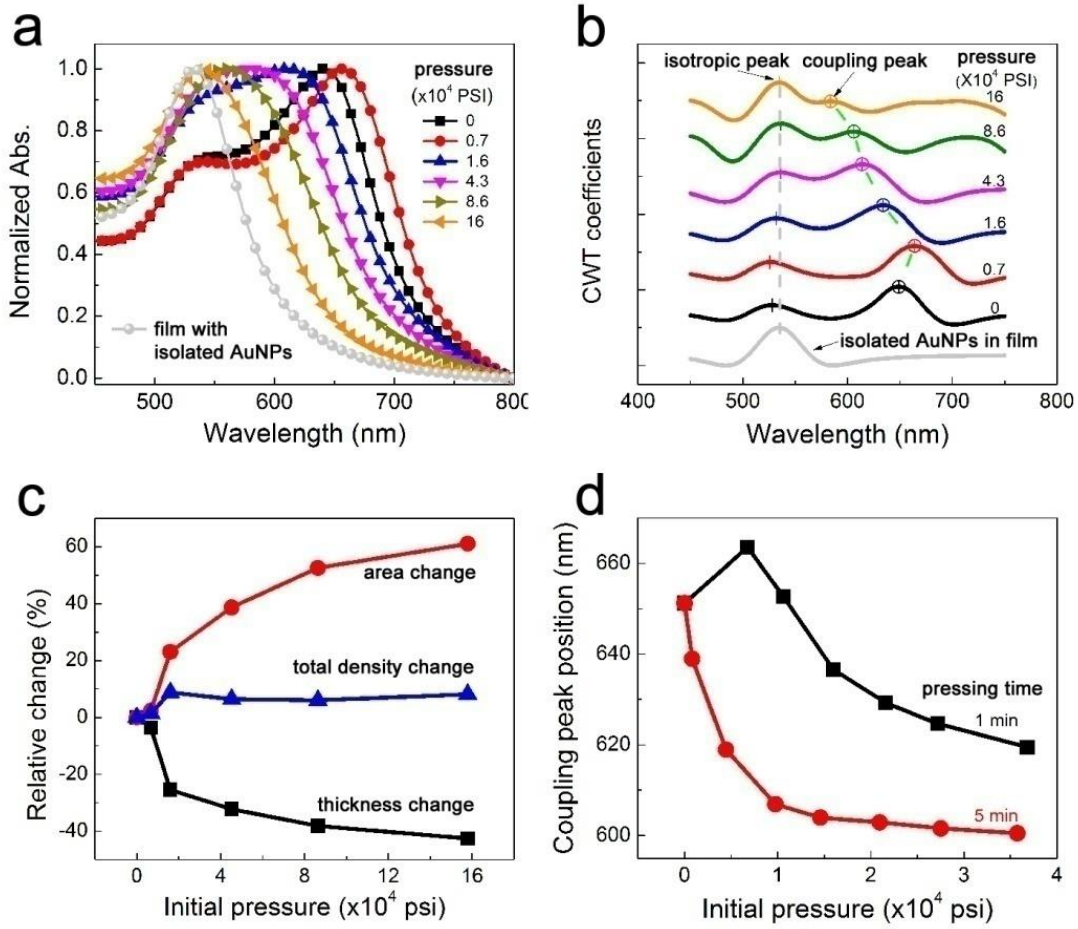

Figure 3.11 (a) The UV-Vis extinction spectra of a typical composite film after experiencing different pressures for a fixed application time (1 min). (b) The CWT of the spectra in (a). (c) Physical deformation profiles of the film after being subjected to various pressures for 1 min. (d) Plot of coupling peak position shift for films experiencing different pressures and application times (1 min and 5 min). Reprinted with permission from ref. 231.

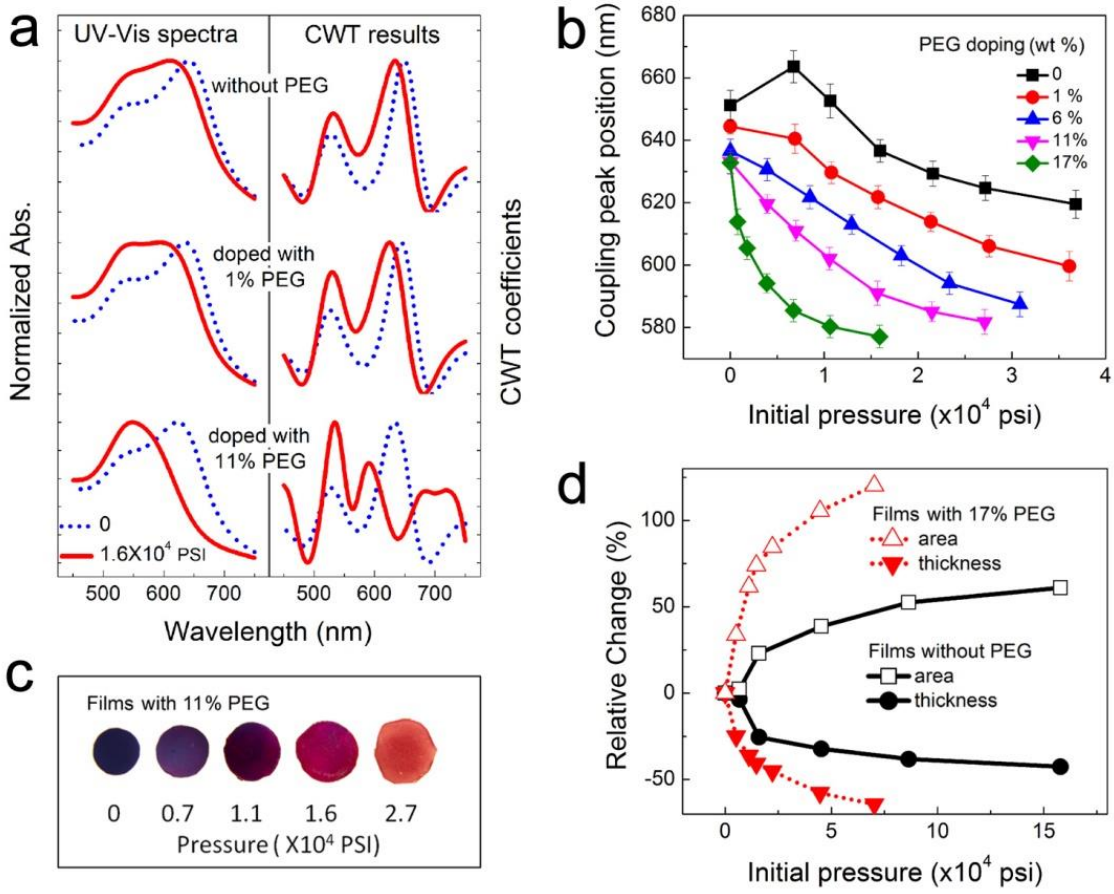

Figure 3.12 Tuning the sensitivity of the optical change to stress by doping the composite film with plasticizer. (a) UV-Vis extinction spectra (left) and their CWT profiles (right) for films doped with different amounts of PEG before (dot) and after (line) being treated with 1.6×10^4 psi of pressure for 1 min. (b) Plot of pressure-dependent coupling peak shift for films doped with different amounts of PEG (press time is 1 min). (c) Digital images of films doped with 11 wt % PEG after experiencing different pressures for 1 min. (d) Deformation profiles of films without and with 17 wt % PEG doping under different pressures for 1 min. Reprinted with permission from ref. 231.

The polymer flow induced disassembly process can be used to construct colorimetric stress sensors that can memorize the mechanical stress experienced by the composite film, as long as the relation between the applied stress at a fixed duration and the band position of the plasmon coupling is pre-established for a particular type of composite film. As PVP is relatively hard at room temperature, only applying a sufficiently large stress can induce a considerable irreversible deformation. To extend the pressure response range and also increase the stress sensitivity of the composite film, the polymer can be modified by doping with plasticizers to improve its fluidity (or to lower its hardness and viscosity). It is known that PVP is miscible with small molecules containing hydroxyl groups, as the proton-donating -OH groups can form H-bonds with the proton-accepting carbonyl groups in PVP.[235] In consequence, by adding these small molecules into PVP, the packing structure of the polymer chains will be reorganized and its fluidity can be improved. In this work, we chose short-chain poly(ethylene glycol) (typically PEG-400) as the plasticizer, which mixed well with PVP and at the same time avoided significant interference to the chain structure of the AuNPs. With increasing addition of PEG-400, the deformation of the polymer composite film becomes more sensitive to the external pressure, as reflected in the optical property change of the polymer composite. By keeping the pressure (1.6×10^4 psi) and the application duration (1 min) fixed, we examined the color change and physical deformation for films doped with various amounts of PEG. As shown in Figure 3.12a, while the sample without PEG only showed a slight blue shift of the coupling peak from ~649 nm to ~635 nm, the addition of PEG led to more significant changes in response to

the compression, with the coupling peak shifting from ~646 nm to ~627 nm (for the case of 1 wt % PEG) and from ~636 nm to ~591 nm (for the case of 11 wt % PEG). The results clearly show that the disassembly of AuNP chains in the polymer film is more significant with greater PEG doping.

We further systematically investigated the dependence of the optical property on the applied pressure for composite films doped with different amounts of PEG (1-17 wt %, Figure 3.12b, c). Samples doped with more than 17 wt % of PEG became too fluidic to form freestanding films with defined shapes. As shown in Figure 3.12b, while the film without PEG exhibits significant optical responses only at relatively high pressures, those containing PEG show a considerable shift in coupling peak position under much lower pressures. For comparison, while a pressure of 1.6×10^5 psi is needed for shifting the coupling peak of the film without PEG to ~583 nm, only 1/10 of the pressure (1.6×10^4 psi) is sufficient to shift the coupling peak to ~577 nm for the sample doped with 17 wt % PEG. Analysis of the physical deformation of the films suggests that the deformation sensitivity also increases with PEG-doping amount, as suggested in Figure 3.12d. It was also found that the shift of the coupling peak was directly related to the extent of film deformation: for films with different PEG loadings, if they have a similar extent of shift in coupling peak, they also have similar extent of deformation. For example, the film without PEG doping showed a 61% expansion in area and a plasmonic shift to ~583 nm after experiencing 1.6×10^5 psi of pressure, while the one doped with 17 wt % of PEG showed a 66% change in area and a plasmonic shift to ~577 nm after being subjected to 1.6×10^4 psi of pressure. This is in good agreement with our expected relationship

between the extent of nanoparticle disassembly and the extent of film deformation. It is therefore clear that by varying the amount of plasticizer, polymer films with different degrees flexibility can be made to detect a wide range of stresses by outputting optical responses.

3.5 Conclusions

In summary, we have studied reversible assembly and disassembly of charged AuNPs from both fundamental and practical aspects. We first synthesized charged gold nanoparticles by citrate reduction method followed by a ligand exchange process to modify the nanoparticle surface with BSPP ligand. By theoretical studying the thermodynamics of the reversible assembly process, we understood the key to control the assembly process is to manipulate colloidal interactions. Experimentally, it is realized assembly of AuNPs can be realized by change of solvent, addition of salt and change of temperature. In particular, thermoresponsive assembly and disassembly of AuNPs were realized by reversible change the temperature of the AuNPs NaCl aqueous solution. By quantitative analyzing the colloidal interaction energy among AuNPs including van der Waals attraction and electrostatic repulsion which were included in the consideration of DLVO as well as the non-DLVO short-range repulsion which is most likely originated from steric repulsion of ligands when nanoparticles begin to closely contact with each other, the thermoresponsive assembly can be understood from the energy point of view. At low temperature, assembly state is thermodynamically stable as an energy well at small interparticle distance forms in the energy diagram under this condition. In contrast,

the energy well does not exist at high temperature, which indicate disassembly state is thermodynamically stable. The kinetics of the reversible assembly process also shows different properties compared to those irreversible assemblies due to its capability of disassembly. It is found by sweeping the temperature in a designed pathway, the optical property of the assemblies can exhibit path dependent memory effect. Microscopically, it is believed the assembly behavior can be analogue to the nucleation and growth process in nanocrystal growth rather than the typical step-growth or chain-growth polymerization models which were used for description of irreversible one-dimensional assembly.

Taking advantage of the disassembly capability of the nanoparticle chains, unique applications that typical metal nanoparticle assembly cannot realize are made possible. As an example, AuNP chains can be transferred into polymer matrix which can be compactable with these Au surface while avoid disturbance of the chain structures. The AuNP chain-polymer composite film exhibits similar optical property of the nanoparticle chains dispersed in solution which shows deep blue color. By applying stress on the composite film, depending on the pressure and stress application time, the color of the film can be changed accordingly from deep blue to purple and then red. The color change is due to the disassembly of the embedded nanoparticle chains in responsive to the external stress which can be proved by the consistency of the nanoparticle shape before and after pressing and the positive correlation between the extent of disassembly and polymer deformation. Finally, the mechanical property of the composite film can be tuned by addition of plasticizers, in this case is PEG, which can extend the mechanical

responsive range of the composite film. The AuNP chain-polymer composite film is expected to be useful to be applied as colorimetric stress memory sensors.

We believe our study on reversible assembly of plasmonic nanoparticles can further be extended to other plasmonic metals including silver, which may extend the color tuning range to cover the full visible range. By incorporating nanoparticle chains into elastomers, the pressure responsive disassembly of AuNP chains can be reversible and may be extended in other applications.

Chapter 4

Conclusion and Outlook

4.1 Conclusion of this thesis

Colloidal synthesis and assembly of nanostructures is an important pathway to produce functional nanoscale devices. The strategy is a bottom-up approach which has advantages including the scalability, robust control on the size and shapes and properties of the materials at nanoscale. However, there still exist challenges for colloidal synthesis and assembly of nanoparticles. Typically, colloidal nanoparticle surfaces are wrapped by organic ligands, which are effective in control the size and shape of nanoparticles, but are difficult to be removed and create challenges for colloidal particles to be applied in a variety of applications including catalysis, photovoltaics, nanoelectronic devices that call for clean surfaces. Although previous researches have dedicated to how to synthesize colloidal nanoparticles with size and shape control, there is a lack of strategies to synthesis of nanoparticles with complex structure. Therefore, the field of colloidal synthesis still has great potentials to be further developed in order to enable colloidal synthesis to be a more useful and efficient strategy for nanomaterial production.

In comparison to colloidal synthesis, there are even fewer mature strategies towards self-assembly of colloidal nanoparticles, which created the bottleneck for the bottom-up approach to nanoscale device fabrication in mass production industry. Since the development of strategies towards self-assembly of colloidal nanostructures is still at

its infant stage, more efforts should be invested in this field. In addition, development of novel assembly strategies such as stimuli-responsive and reversible assembly are important for dynamic tuning the property of nanomaterials which can also extend the benefit of this materials processing technique.

In this thesis, we have presented our contributions to the development of colloidal synthesis and assembly of functional nanostructures and applications. In particular our studies have made contributions to development of strategies of shape control synthesis of anatase TiO_2 nanocrystals and reversible assembly of charged gold nanoparticles. We also investigated their properties and utilized them in practical applications. We started by presenting our fundamental understandings on colloidal synthesis and assembly of nanostructures. These understandings laid solid theoretical foundations for our research projects. Shape control of anatase TiO_2 nanocrystals attracts research interest as it is critical in optimize the performances of TiO_2-based applications including photocatalysis and photovoltaics. We have developed synthesis strategies towards synthesis of anatase TiO_2 nanocrystals with faceted morphology as well as with higher structural complexity by chemical transformation and seed-mediated growth methods. It has also been confirmed the development of these synthesis strategies are beneficial for optimization of the properties of anatase TiO_2 in photocatalysis. Development of strategies towards reversible assembly of plasmonic nanostructures is of great importance as the process enables dynamic tuning of the plasmonic properties. In our study, we successfully realized reversible assembly of charged gold nanoparticles and enabled dynamic tuning of their optical properties. The unique property derived from the disassembly process also

allows us to take its advantage for practical applications. In our case, we blended gold nanoparticle chains with polymer. By using mechanical stress that the nanoparticle chains can be disassembled and induce plasmon de-coupling which results in color change of the film. The composite film is expected to be used as colorimetric stress memory sensor.

4.2 Outlook and future work

In my future work, I will continue focus on TiO_2-based and gold nanoparticle-based materials for applications. The first plan is to investigate the benefit of fluorine-doping for visible light photocatalysis. As introduced in **Chapter 2**, we have successfully synthesized fluorine doped anatase TiO_2 nanocrystals with enhanced visible light absorption. It is expected the nanocrystals are capable to enhance the photocatalytic activity of TiO_2 under visible light due to the enhanced absorption. Since it is noticed in previous experiment that the dopants are not stable under oxidation environment, we also plan to study the possibility to enhance the chemical stability of the fluorine doped anatase TiO_2 nanocrystals. One of our approach will be developing an anatase TiO_2 coating on the fluorine doped TiO_2. It is expected by appropriate choosing the shape directing organic ligands, a uniform layer of non-doped anatase TiO_2 can be deposited on the doped nanocrystals by nonaqueous seed-mediated growth rather than antenna nanorods as we demonstrated in the previous cases. This strategy provides the possibility that the dopants can be limited to the inner core. Overall, the nanocrystals are expected to be active in response to visible light while maintain the chemical stability. As we have successfully demonstrated the benefit of making anatase TiO_2 nanocrystals into complex

structures for photocatalytic applications. We believe the potential of this type of materials is far beyond the use in photocatalysis. For example, one of our plans is to take advantage of the hierarchical structures of the nanocrystals to improve the performance of photovoltaic devices such as organic-nanocrystal hybrid solar cells. In this design, hierarchical anatase TiO_2 nanocrystals can be used as an acceptor layer. Meanwhile, the hierarchical structure of the nanocrystals helps the inter-penetration of the organic and nanocrystal layers which is expected to enhance the charge separation efficiency.[236]

There are also rooms for improving the reversible assembly of plasmonic nanoparticles. As has mentioned in the last chapter, the composition of the nanoparticles can be extend to gold-silver alloy or silver. Since gold-silver alloy and silver have strong plasmonic absorption at around 400 nm, assembly of these nanoparticles are expected to shift the absorption to longer wavelength and enable full visible range optical tuning.[181, 237] To extend the applications of the reversibility of this type of assembly, we plan to extend the assembly to be responsive to other types of stimuli. In particular, light and magnets are considered to be ideal external stimuli to control the assembly process as the particles can be actuated instantly. In the case of light-responsive assembly and disassembly of plasmonic nanoparticles, we plan to use linear polarized light to induce a transient dispersion force for these nanoparticles. When the nanoparticles are under the condition that are about to assemble, an introduction of attraction from the dispersion force will be critical to induce the assembly of particles. As the induced dispersion force is anisotropic, we also expect the direction of assemblies can also be controlled. Specifically in this case, we expect the direction of one-dimensional assembly of

nanoparticles should be parallel to the polarization and perpendicular to the incident light. If this type of assemblies can be achieved, the macroscopic optical property of the assembly will also be anisotropic due to the anisotropy of the plasmon coupling. In order to realize magnetic responsive assembly of plasmonic nanoparticles, magnetoplasmonic nanoparticles need to be synthesized and their surfaces need to be appropriately modified. We propose a synthesis of plasmonic nanoparticles with a superparamagnetic core by multi-step synthesis approaches. In this plan, monodispersed superparamagnetic nanoparticles are proposed to be first synthesized, with attachment of gold seeds. The composite nanoparticles are then encapsulated in a nanoshell by sequential coating of silica and polymer and removal of the sacrificial silica layer. A templated seed-mediated growth process is then performed followed by an etching of template polymer layer and appropriate surface modification of the nanoparticle surface. As the result, nanoparticles with a magnetic core and plasmonic shell should be produced. When this type of nanoparticles are dispersed in appropriate solvents, if an external magnetic field with appropriate strength is applied, the nanoparticles are expected to be assembled driven by the field-dipole packing force. When the external magnetic field is off, it is expected the nanoparticles to be disassembled. Therefore, the reversible plasmon tuning can be achieved by magnetically control of the plasmon coupling of the magnetoplasmonic nanoparticles. We also plan to add reversibility to the colorimetric stress memory sensor by substituting PVP-based polymer matrix by elastomers. If the gold nanoparticle chains can be successfully transferred to an elastomer matrix while the gold-elastomer interaction is strong enough to enable embedded nanoparticles to be able to move

individually rather than collectively moving as a chain. Disassembly of gold nanoparticle chains is expected and cause change in optical property of the composite when stress is applied and deformation of the composite film is induced. The elasticity of the composite provides the possibility for nanoparticles to re-assembly by removal of stress. Therefore, a stress responsive colorimetric elastomer can be produced.

From a broader impact, although there have been significant achievements in the field of nanostructure synthesis and assembly with many different types of materials, we will continue to put intensive efforts on development of this field as there are still plenty of opportunities to take advantage of the colloidal nanoparticles for applications. In the future, the newly developed nanostructure synthesis and assembly techniques need to be more versatile, programmable, scalable, cost-effective and in more predictable manners. The surface chemistry of colloidal nanomaterials need also be seriously taken into consideration. Thus, the applications of these colloidal nanomaterials can be extended to a broader range including those were previously limited by the issues such as cost, surface compatibility, scalability etc.

References

1. Faraday, M., *The Bakerian Lecture: Experimental relations of gold (and other metals) to light.* Philosophical Transactions of the Royal Society of London, 1857. **147**: p. 145-181.
2. www.nano.gov.
3. Alivisatos, A.P., *Semiconductor clusters, nanocrystals, and quantum Dots.* Science, 1996. **271**(5251): p. 933-937.
4. Bakonyi, I. and Péter, L., *Electrodeposited multilayer films with giant magnetoresistance (GMR): Progress and problems.* Progress in Materials Science, 2010. **55**(3): p. 107-245.
5. Treacy, M.M.J., Ebbesen, T.W., and Gibson, J.M., *Exceptionally high Young's modulus observed for individual carbon nanotubes.* Nature, 1996. **381**(6584): p. 678-680.
6. Eustis, S. and El-Sayed, M.A., *Why gold nanoparticles are more precious than pretty gold: Noble metal surface plasmon resonance and its enhancement of the radiative and nonradiative properties of nanocrystals of different shapes.* Chemical Society Reviews, 2006. **35**(3): p. 209-217.
7. Dabbousi, B.O., et al., *(CdSe)ZnS core−shell quantum dots: Synthesis and characterization of a size series of highly luminescent nanocrystallites.* The Journal of Physical Chemistry B, 1997. **101**(46): p. 9463-9475.
8. DiSalvo, F.J., *Thermoelectric cooling and power generation.* Science, 1999. **285**(5428): p. 703-706.

9. Zhao, D., et al., *Triblock copolymer syntheses of mesoporous silica with periodic 50 to 300 angstrom pores.* Science, 1998. **279**(5350): p. 548-552.

10. Yin, Y. and Alivisatos, A.P., *Colloidal nanocrystal synthesis and the organic-inorganic interface.* Nature, 2005. **437**(7059): p. 664-670.

11. Peng, X., et al., *Shape control of CdSe nanocrystals.* Nature, 2000. **404**(6773): p. 59-61.

12. Xia, Y., Xiong, Y., Lim, B., and Skrabalak, S.E., *Shape-controlled synthesis of metal nanocrystals: simple chemistry meets complex physics?* Angewandte Chemie International Edition, 2009. **48**(1): p. 60-103.

13. Xia, Y. and Whitesides, G.M., *SOFT LITHOGRAPHY.* Annual Review of Materials Science, 1998. **28**(1): p. 153-184.

14. Vieu, C., et al., *Electron beam lithography: resolution limits and applications.* Applied Surface Science, 2000. **164**(1–4): p. 111-117.

15. Cao, G., *Nanostructures and Nanomaterials: Synthesis, Properties and Applications*. 2004: World Scientific.

16. Tseng, A.A., Chen, K., Chen, C.D., and Ma, K.J., *Electron beam lithography in nanoscale fabrication: recent development.* IEEE Transactions on Electronics Packaging Manufacturing, 2003. **26**(2): p. 141-149.

17. Whitesides, G.M. and Grzybowski, B., *Self-assembly at all scales.* Science, 2002. **295**(5564): p. 2418-2421.

18. Whitesides, G.M. and Boncheva, M., *Beyond molecules: Self-assembly of mesoscopic and macroscopic components.* Proceedings of the National Academy of Sciences, 2002. **99**(8): p. 4769-4774.

19. Puntes, V.F., Krishnan, K.M., and Alivisatos, A.P., *Colloidal nanocrystal shape and size control: the case of cobalt.* Science, 2001. **291**(5511): p. 2115-2117.

20. Zhang, Q., et al., *A systematic study of the synthesis of silver nanoplates: is citrate a "magic" reagent?* Journal of the American Chemical Society, 2011. **133**(46): p. 18931-18939.

21. Sun, S., et al., *Monodisperse MFe2O4 (M= Fe, Co, Mn) nanoparticles.* Journal of the American Chemical Society, 2004. **126**(1): p. 273-279.

22. LaMer, V.K. and Dinegar, R.H., *Theory, production and mechanism of formation of monodispersed hydrosols.* Journal of the American Chemical Society, 1950. **72**(11): p. 4847-4854.

23. Sun, Y., *Controlled synthesis of colloidal silver nanoparticles in organic solutions: empirical rules for nucleation engineering.* Chemical Society Reviews, 2013. **42**(7): p. 2497-2511.

24. Cushing, B.L., Kolesnichenko, V.L., and O'Connor, C.J., *Recent advances in the liquid-phase syntheses of inorganic nanoparticles.* Chemical reviews, 2004. **104**(9): p. 3893-3946.

25. Zhang, Q., Liu, S.-J., and Yu, S.-H., *Recent advances in oriented attachment growth and synthesis of functional materials: concept, evidence, mechanism, and future.* Journal of Materials Chemistry, 2009. **19**(2): p. 191-207.

26. Peng, Z.A. and Peng, X., *Nearly monodisperse and shape-controlled CdSe nanocrystals via alternative routes: nucleation and growth.* Journal of the American Chemical Society, 2002. **124**(13): p. 3343-3353.

27. Pacholski, C., Kornowski, A., and Weller, H., *Self-assembly of ZnO: from nanodots to nanorods.* Angewandte Chemie International Edition, 2002. **41**(7): p. 1188-1191.

28. Manna, L., Scher, E.C., and Alivisatos, A.P., *Synthesis of soluble and processable rod-, arrow-, teardrop-, and tetrapod-shaped CdSe nanocrystals.* Journal of the American Chemical Society, 2000. **122**(51): p. 12700-12706.

29. Narayanaswamy, A., et al., *Formation of nearly monodisperse In2O3 nanodots and oriented-attached nanoflowers: hydrolysis and alcoholysis vs pyrolysis.* Journal of the American Chemical Society, 2006. **128**(31): p. 10310-10319.

30. Cho, K.-S., Talapin, D.V., Gaschler, W., and Murray, C.B., *Designing PbSe nanowires and nanorings through oriented attachment of nanoparticles.* Journal of the American Chemical Society, 2005. **127**(19): p. 7140-7147.

31. Norris, D.J. and Bawendi, M.G., *Measurement and assignment of the size-dependent optical spectrum in CdSe quantum dots.* Physical Review B, 1996. **53**(24): p. 16338.

32. Kelly, K.L., Coronado, E., Zhao, L.L., and Schatz, G.C., *The optical properties of metal nanoparticles: the influence of size, shape, and dielectric environment.* The Journal of Physical Chemistry B, 2003. **107**(3): p. 668-677.

33. Gao, C., et al., *One-step seeded growth of Au nanoparticles with widely tunable sizes.* Nanoscale, 2012. **4**(9): p. 2875-2878.

34. Liu, X., Yin, Y., and Gao, C., *Size-tailored synthesis of silver quasi-nanospheres by kinetically controlled seeded growth.* Langmuir, 2013. **29**(33): p. 10559-10565.

35. Haruta, M. and Daté, M., *Advances in the catalysis of Au nanoparticles.* Applied Catalysis A: General, 2001. **222**(1–2): p. 427-437.

36. Subramanian, V., Wolf, E.E., and Kamat, P.V., *Catalysis with TiO2/gold nanocomposites. Effect of metal particle size on the Fermi level equilibration.* Journal of the American Chemical Society, 2004. **126**(15): p. 4943-4950.

37. Reiss, H., *The growth of uniform colloidal dispersions.* The Journal of Chemical Physics, 1951. **19**(4): p. 482-487.

38. Peng, X., Wickham, J., and Alivisatos, A.P., *Kinetics of II-VI and III-V colloidal semiconductor nanocrystal growth:"focusing" of size distributions.* Journal of the American Chemical Society, 1998. **120**(21): p. 5343-5344.

39. Bastús, N.G., Comenge, J., and Puntes, V., *Kinetically controlled seeded growth synthesis of citrate-stabilized gold nanoparticles of up to 200 nm: size focusing versus Ostwald ripening.* Langmuir, 2011. **27**(17): p. 11098-11105.

40. de Mello Donegá, C., Liljeroth, P., and Vanmaekelbergh, D., *Physicochemical evaluation of the hot-injection method, a synthesis route for monodisperse nanocrystals.* Small, 2005. **1**(12): p. 1152-1162.

41. Kwon, S.G. and Hyeon, T., *Formation mechanisms of uniform nanocrystals via hot-injection and heat-up methods.* Small, 2011. **7**(19): p. 2685-2702.

42. Park, J., et al., *Synthesis of monodisperse spherical nanocrystals.* Angewandte Chemie International Edition, 2007. **46**(25): p. 4630-4660.

43. Peng, S., Wang, C., Xie, J., and Sun, S., *Synthesis and stabilization of monodisperse Fe nanoparticles.* Journal of the American Chemical Society, 2006. **128**(33): p. 10676-10677.

44. Park, J., et al., *One-nanometer-scale size-controlled synthesis of monodisperse magnetic Iron oxide nanoparticles.* Angewandte Chemie, 2005. **117**(19): p. 2932-2937.

45. Gao, C., Goebl, J., and Yin, Y., *Seeded growth route to noble metal nanostructures.* Journal of Materials Chemistry C, 2013. **1**(25): p. 3898-3909.

46. Duff, D.G., Baiker, A., and Edwards, P.P., *A new hydrosol of gold clusters. 1. Formation and particle size variation.* Langmuir, 1993. **9**(9): p. 2301-2309.

47. Jana, N.R., Gearheart, L., and Murphy, C.J., *Seed-mediated growth approach for shape-controlled synthesis of spheroidal and rod-like gold nanoparticles using a surfactant template.* Advanced Materials, 2001. **13**(18): p. 1389.

48. Jana, N.R., Gearheart, L., and Murphy, C.J., *Wet chemical synthesis of high aspect ratio cylindrical gold nanorods.* The Journal of Physical Chemistry B, 2001. **105**(19): p. 4065-4067.

49. Sun, S. and Zeng, H., *Size-controlled synthesis of magnetite nanoparticles.* Journal of the American Chemical Society, 2002. **124**(28): p. 8204-8205.

50. Talapin, D.V., et al., *Seeded growth of highly luminescent CdSe/CdS nanoheterostructures with rod and tetrapod morphologies.* Nano Letters, 2007. **7**(10): p. 2951-2959.

51. Nikoobakht, B. and El-Sayed, M.A., *Preparation and growth mechanism of gold nanorods (NRs) using seed-mediated growth method.* Chemistry of Materials, 2003. **15**(10): p. 1957-1962.

52. Zhang, Q., et al., *Reconstruction of silver nanoplates by UV irradiation: tailored optical properties and enhanced stability.* Angewandte Chemie, 2009. **121**(19): p. 3568-3571.

53. Tian, N., et al., *Synthesis of tetrahexahedral platinum nanocrystals with high-index facets and high electro-oxidation activity.* Science, 2007. **316**(5825): p. 732-735.

54. Yang, H.G., et al., *Anatase TiO2 single crystals with a large percentage of reactive facets.* Nature, 2008. **453**(7195): p. 638-641.

55. Chauhan, V.P., et al., *Fluorescent nanorods and nanospheres for real-time in vivo probing of nanoparticle shape-dependent tumor penetration.* Angewandte Chemie, 2011. **123**(48): p. 11619-11622.

56. Peng, X., *Mechanisms for the shape-control and shape-evolution of colloidal semiconductor nanocrystals.* Advanced Materials, 2003. **15**(5): p. 459-463.

57. Sun, Y. and Xia, Y., *Shape-controlled synthesis of gold and silver nanoparticles.* Science, 2002. **298**(5601): p. 2176-2179.

58. Jun, Y.-w., et al., *Surfactant-assisted elimination of a high energy facet as a means of controlling the shapes of TiO2 nanocrystals.* Journal of the American Chemical Society, 2003. **125**(51): p. 15981-15985.

59. Lee, S.M., Cho, S.N., and Cheon, J., *Anisotropic shape control of colloidal inorganic nanocrystals.* Advanced Materials, 2003. **15**(5): p. 441-444.

60. Jun, Y.w., Choi, J.s., and Cheon, J., *Shape control of semiconductor and metal oxide nanocrystals through nonhydrolytic colloidal routes.* Angewandte Chemie International Edition, 2006. **45**(21): p. 3414-3439.

61. Manna, L., et al., *Controlled growth of tetrapod-branched inorganic nanocrystals.* Nature Materials, 2003. **2**(6): p. 382-385.

62. Zhang, Q., et al., *Seeded growth of uniform Ag nanoplates with high aspect ratio and widely tunable surface plasmon bands.* Nano Letters, 2010. **10**(12): p. 5037-5042.

63. Zeng, J., et al., *Successive deposition of silver on silver nanoplates: lateral versus vertical growth.* Angewandte Chemie International Edition, 2011. **50**(1): p. 244-249.

64. Lofton, C. and Sigmund, W., *Mechanisms controlling crystal habits of gold and silver colloids.* Advanced Functional Materials, 2005. **15**(7): p. 1197-1208.

65. Aherne, D., Ledwith, D.M., Gara, M., and Kelly, J.M., *Optical properties and growth aspects of silver nanoprisms produced by a highly reproducible and rapid synthesis at room temperature.* Advanced Functional Materials, 2008. **18**(14): p. 2005-2016.

66. Xiong, Y. and Xia, Y., *Shape-controlled synthesis of metal nanostructures: the case of palladium.* Advanced Materials, 2007. **19**(20): p. 3385-3391.

67. Lim, B., et al., *Shape-controlled synthesis of Pd nanocrystals in aqueous solutions.* Advanced Functional Materials, 2009. **19**(2): p. 189-200.

68. Liu, Y., Goebl, J., and Yin, Y., *Templated synthesis of nanostructured materials.* Chemical Society Reviews, 2013. **42**(7): p. 2610-2653.

69. Yang, J., Lind, J.U., and Trogler, W.C., *Synthesis of hollow silica and titania nanospheres.* Chemistry of Materials, 2008. **20**(9): p. 2875-2877.

70. Gao, C., Zhang, Q., Lu, Z., and Yin, Y., *Templated synthesis of metal nanorods in silica nanotubes.* Journal of the American Chemical Society, 2011. **133**(49): p. 19706-19709.

71. Lee, Y., et al., *Large-scale synthesis of uniform and crystalline magnetite nanoparticles using reverse micelles as nanoreactors under reflux conditions.* Advanced Functional Materials, 2005. **15**(3): p. 503-509.

72. Zarur, A.J. and Ying, J.Y., *Reverse microemulsion synthesis of nanostructured complex oxides for catalytic combustion.* Nature, 2000. **403**(6765): p. 65-67.

73. Zhang, L.X., et al., *The effect of template phase on the structures of as-synthesized silica nanoparticles with fragile didodecyldimethylammonium bromide vesicles as templates.* Advanced Materials, 2007. **19**(23): p. 4279-4283.

74. Yin, Y., et al., *Formation of hollow nanocrystals through the nanoscale Kirkendall effect.* Science, 2004. **304**(5671): p. 711-714.

75. Son, D.H., Hughes, S.M., Yin, Y., and Alivisatos, A.P., *Cation exchange reactions in ionic nanocrystals.* Science, 2004. **306**(5698): p. 1009-1012.

76. Sun, Y. and Xia, Y., *Alloying and dealloying processes involved in the preparation of metal nanoshells through a galvanic replacement reaction.* Nano Letters, 2003. **3**(11): p. 1569-1572.

77. Skrabalak, S.E., et al., *Gold nanocages: synthesis, properties, and applications.* Accounts of Chemical Research, 2008. **41**(12): p. 1587-1595.

78. Goebl, J., Zhang, Q., He, L., and Yin, Y., *Monitoring the shape evolution of silver nanoplates: A marker study.* Angewandte Chemie International Edition, 2012. **51**(2): p. 552-555.

79. Lee, I., Morales, R., Albiter, M.A., and Zaera, F., *Synthesis of heterogeneous catalysts with well shaped platinum particles to control reaction selectivity.* Proceedings of the National Academy of Sciences, 2008. **105**(40): p. 15241-15246.

80. Willets, K.A. and Van Duyne, R.P., *Localized surface plasmon resonance spectroscopy and sensing.* Annual Review of Physical Chemistry, 2007. **58**: p. 267-297.

81. Gao, X., et al., *In vivo cancer targeting and imaging with semiconductor quantum dots.* Nature Biotechnology, 2004. **22**(8): p. 969-976.

82. Boisselier, E. and Astruc, D., *Gold nanoparticles in nanomedicine: preparations, imaging, diagnostics, therapies and toxicity.* Chemical Society Reviews, 2009. **38**(6): p. 1759-1782.

83. Zhang, T., Ge, J., Hu, Y., and Yin, Y., *A general approach for transferring hydrophobic nanocrystals into water.* Nano Letters, 2007. **7**(10): p. 3203-3207.

84. Dong, A., et al., *A generalized ligand-exchange strategy enabling sequential surface functionalization of colloidal nanocrystals.* Journal of the American Chemical Society, 2010. **133**(4): p. 998-1006.

85. Lohse, S.E., et al., *A simple millifluidic benchtop reactor system for the high-throughput synthesis and functionalization of gold nanoparticles with different sizes and shapes.* ACS Nano, 2013. **7**(5): p. 4135-4150.

86. Zhang, L. and Xia, Y., *Scaling up the production of colloidal nanocrystals: should we increase or decrease the reaction volume?* Advanced Materials, 2014. **26**(16): p. 2600-2606.

87. Hoefflinger, B., *ITRS: The international technology roadmap for semiconductors*, in *Chips 2020*. 2012, Springer. p. 161-174.

88. Nie, Z., Petukhova, A., and Kumacheva, E., *Properties and emerging applications of self-assembled structures made from inorganic nanoparticles.* Nature Nanotechnology, 2010. **5**(1): p. 15-25.

89. Ulman, A., *Formation and structure of self-assembled monolayers.* Chemical Reviews, 1996. **96**(4): p. 1533-1554.

90. Cui, H., et al., *Block copolymer assembly via kinetic control.* Science, 2007. **317**(5838): p. 647-650.

91. Caruso, F., Caruso, R.A., and Möhwald, H., *Nanoengineering of inorganic and hybrid hollow spheres by colloidal templating.* Science, 1998. **282**(5391): p. 1111-1114.

92. He, Y., et al., *Hierarchical self-assembly of DNA into symmetric supramolecular polyhedra.* Nature, 2008. **452**(7184): p. 198-201.

93. Butt, H.-J., Graf, K., and Kappl, M., *Physics and Chemistry of Interfaces*. 2003: John Wiley & Sons.

94. Bishop, K.J.M., Wilmer, C.E., Soh, S., and Grzybowski, B.A., *Nanoscale forces and their uses in self-assembly.* Small, 2009. **5**(14): p. 1600-1630.

95. Min, Y., et al., *The role of interparticle and external forces in nanoparticle assembly.* Nature Materials, 2008. **7**(7): p. 527-538.

96. Grzelczak, M., Vermant, J., Furst, E.M., and Liz-Marzán, L.M., *Directed self-assembly of nanoparticles.* ACS Nano, 2010. **4**(7): p. 3591-3605.

97. Verwey, E.J.W. and Overbeek, J.T.G., *Theory of the stability of lyophobic colloids: The interaction of sol particles having an electric double layer*. 1948: Elsevier Publishing Company.

98. Hamaker, H.C., *The London—van der Waals attraction between spherical particles.* Physica, 1937. **4**(10): p. 1058-1072.

99. Dzyaloshinskii, I.E.e., Lifshitz, E.M., and Pitaevskii, L.P., *General theory of van der Waals force.* Soviet Physics Uspekhi, 1961. **4**(2): p. 153-176.

100. Kim, H.-Y., et al., *Van der Waals forces between nanoclusters: importance of many-body effects.* The Journal of Chemical Physics, 2006. **124**(7): p. 074504.

101. Hong, L., Cacciuto, A., Luijten, E., and Granick, S., *Clusters of charged Janus spheres.* Nano Letters, 2006. **6**(11): p. 2510-2514.

102. Badawy, A.M.E., et al., *Impact of environmental conditions (pH, ionic strength, and electrolyte type) on the surface charge and aggregation of silver nanoparticles suspensions.* Environmental Science & Technology, 2010. **44**(4): p. 1260-1266.

103. Chapman, D.L., *LI. A contribution to the theory of electrocapillarity.* The London, Edinburgh, and Dublin Philosophical Magazine and Journal of Science, 1913. **25**(148): p. 475-481.

104. Grahame, D.C., *The electrical double layer and the theory of electrocapillarity.* Chemical Reviews, 1947. **41**(3): p. 441-501.

105. Ge, J., He, L., Goebl, J., and Yin, Y., *Assembly of magnetically tunable photonic crystals in nonpolar solvents.* Journal of the American Chemical Society, 2009. **131**(10): p. 3484-3486.

106. He, L., Hu, Y., Wang, M., and Yin, Y., *Determination of solvation layer thickness by a magnetophotonic approach.* ACS Nano, 2012. **6**(5): p. 4196-4202.

107. Pashley, R.M., *DLVO and hydration forces between mica surfaces in Li+, Na+, K+, and Cs+ electrolyte solutions: A correlation of double-layer and hydration forces with surface cation exchange properties.* Journal of Colloid and Interface Science, 1981. **83**(2): p. 531-546.

108. Sánchez-Iglesias, A., et al., *Hydrophobic interactions modulate self-assembly of nanoparticles.* ACS Nano, 2012. **6**(12): p. 11059-11065.

109. Tang, Z., Kotov, N.A., and Giersig, M., *Spontaneous organization of single CdTe nanoparticles into luminescent nanowires.* Science, 2002. **297**(5579): p. 237-240.

110. Tang, Z. and Kotov, N.A., *One-dimensional assemblies of nanoparticles: preparation, properties, and promise.* Advanced Materials, 2005. **17**(8): p. 951-962.

111. Ge, J., Hu, Y., and Yin, Y., *Highly tunable superparamagnetic colloidal photonic crystals.* Angewandte Chemie, 2007. **119**(39): p. 7572-7575.

112. Ge, J., et al., *Self-assembly and field-responsive optical diffractions of superparamagnetic colloids.* Langmuir, 2008. **24**(7): p. 3671-3680.

113. Klajn, R., Bishop, K.J.M., and Grzybowski, B.A., *Light-controlled self-assembly of reversible and irreversible nanoparticle suprastructures.* Proceedings of the National Academy of Sciences, 2007. **104**(25): p. 10305-10309.

114. Sreeprasad, T.S. and Pradeep, T., *Reversible assembly and disassembly of gold nanorods induced by EDTA and its application in SERS tuning.* Langmuir, 2011. **27**(7): p. 3381-3390.

115. Park, S.Y., et al., *DNA-programmable nanoparticle crystallization.* Nature, 2008. **451**(7178): p. 553-556.

116. Ai, K., Liu, Y., and Lu, L., *Hydrogen-bonding recognition-induced color change of gold nanoparticles for visual detection of melamine in raw milk and infant formula.* Journal of the American Chemical Society, 2009. **131**(27): p. 9496-9497.

117. Akcora, P., et al., *Anisotropic self-assembly of spherical polymer-grafted nanoparticles.* Nature Materials, 2009. **8**(4): p. 354-359.

118. Chandler, D., *Interfaces and the driving force of hydrophobic assembly.* Nature, 2005. **437**(7059): p. 640-647.

119. Baranov, D., et al., *Assembly of colloidal semiconductor nanorods in solution by depletion attraction.* Nano Letters, 2010. **10**(2): p. 743-749.

120. Young, K.L., et al., *Assembly of reconfigurable one-dimensional colloidal superlattices due to a synergy of fundamental nanoscale forces.* Proceedings of the National Academy of Sciences, 2012. **109**(7): p. 2240-2245.

121. Hu, M.-J., et al., *High yield synthesis of bracelet-like hydrophilic Ni−Co magnetic alloy flux-closure nanorings.* Journal of the American Chemical Society, 2008. **130**(35): p. 11606-11607.

122. Glotzer, S.C. and Solomon, M.J., *Anisotropy of building blocks and their assembly into complex structures.* Nature Materials, 2007. **6**(8): p. 557-562.

123. Liu, K., et al., *Step-growth polymerization of inorganic nanoparticles.* Science, 2010. **329**(5988): p. 197-200.

124. Gangwal, S., Pawar, A., Kretzschmar, I., and Velev, O.D., *Programmed assembly of metallodielectric patchy particles in external AC electric fields.* Soft Matter, 2010. **6**(7): p. 1413-1418.

125. He, L., Wang, M., Ge, J., and Yin, Y., *Magnetic assembly route to colloidal responsive photonic nanostructures.* Accounts of Chemical Research, 2012. **45**(9): p. 1431-1440.

126. Lin, Y., et al., *Nanoparticle assembly and transport at liquid-liquid interfaces.* Science, 2003. **299**(5604): p. 226-229.

127. Böker, A., He, J., Emrick, T., and Russell, T.P., *Self-assembly of nanoparticles at interfaces.* Soft Matter, 2007. **3**(10): p. 1231-1248.

128. Brinker, C.J., Lu, Y., Sellinger, A., and Fan, H., *Evaporation-induced self-assembly: nanostructures made easy.* Advanced Materials, 1999. **11**(7): p. 579-585.

129. Zhang, J., Li, Y., Zhang, X., and Yang, B., *Colloidal self-assembly meets nanofabrication: From two-dimensional colloidal crystals to nanostructure arrays.* Advanced Materials, 2010. **22**(38): p. 4249-4269.

130. Xia, Y., Gates, B., Yin, Y., and Lu, Y., *Monodispersed colloidal spheres: old materials with new applications.* Advanced Materials, 2000. **12**(10): p. 693-713.

131. Shevchenko, E.V., et al., *Structural diversity in binary nanoparticle superlattices.* Nature, 2006. **439**(7072): p. 55-59.

132. Talapin, D.V. and Murray, C.B., *PbSe nanocrystal solids for n-and p-channel thin film field-effect transistors.* Science, 2005. **310**(5745): p. 86-89.

133. Chen, X. and Mao, S.S., *Titanium dioxide nanomaterials: synthesis, properties, modifications, and applications.* Chemical Reviews, 2007. **107**(7): p. 2891-2959.

134. Fujishima, A. and Honda, K., *Electrochemical photolysis of water at a semiconductor electrode.* Nature, 1972(238): p. 37-8.

135. Zhang, Q., et al., *A highly active titanium dioxide based visible-light photocatalyst with nonmetal doping and plasmonic metal decoration.* Angewandte Chemie, 2011. **123**(31): p. 7226-7230.

136. Joo, J.B., et al., *Mesoporous anatase titania hollow nanostructures though silica-protected calcination.* Advanced Functional Materials, 2012. **22**(1): p. 166-174.

137. Joo, J.B., et al., *Control of the nanoscale crystallinity in mesoporous TiO 2 shells for enhanced photocatalytic activity.* Energy & Environmental Science, 2012. **5**(4): p. 6321-6327.

138. O'Regan, B. and Gratzel, M., *A low-cost, high-efficiency solar cell based on dye-sensitized colloidal TiO2 films.* Nature, 1991. **353**(6346): p. 737-740.

139. Subramanian, V., Wolf, E., and Kamat, P.V., *Semiconductor-metal composite nanostructures. To what extent do metal nanoparticles improve the photocatalytic activity of TiO2 films?* The Journal of Physical Chemistry B, 2001. **105**(46): p. 11439-11446.

140. Liu, B. and Aydil, E.S., *Growth of oriented single-crystalline rutile TiO2 nanorods on transparent conducting substrates for dye-sensitized solar cells.* Journal of the American Chemical Society, 2009. **131**(11): p. 3985-3990.

141. Williams, S.S., et al., *Nanostructured titania− polymer photovoltaic devices made using PFPE-based nanomolding techniques.* Chemistry of Materials, 2008. **20**(16): p. 5229-5234.

142. Li, J. and Xu, D., *Tetragonal faceted-nanorods of anatase TiO2 single crystals with a large percentage of active {100} facets.* Chemical Communications, 2010. **46**(13): p. 2301-2303.

143. Pan, J., Liu, G., Lu, G.Q.M., and Cheng, H.M., *On the true photoreactivity order of {001},{010}, and {101} facets of anatase TiO2 crystals.* Angewandte Chemie International Edition, 2011. **50**(9): p. 2133-2137.

144. Liu, G., Jimmy, C.Y., Lu, G.Q.M., and Cheng, H.-M., *Crystal facet engineering of semiconductor photocatalysts: motivations, advances and unique properties.* Chemical Communications, 2011. **47**(24): p. 6763-6783.

145. Xu, H., et al., *High-active anatase TiO2 nanosheets exposed with 95%{100} facets toward efficient H2 evolution and CO2 photoreduction.* ACS Applied Materials & Interfaces, 2013. **5**(4): p. 1348-1354.

146. Roy, N., Sohn, Y., and Pradhan, D., *Synergy of low-energy {101} and high-energy {001} TiO2 crystal facets for enhanced photocatalysis.* ACS Nano, 2013. **7**(3): p. 2532-2540.

147. Ma, X., Dai, Y., Guo, M., and Huang, B., *Relative photooxidation and photoreduction activities of the {100},{101}, and {001} surfaces of anatase TiO2.* Langmuir, 2013. **29**(44): p. 13647-13654.

148. Cho, I.S., et al., *Branched TiO2 nanorods for photoelectrochemical hydrogen production.* Nano Letters, 2011. **11**(11): p. 4978-4984.

149. Lu, Q., et al., *Photocatalytic synthesis and photovoltaic application of Ag-TiO2 nanorod composites.* Nano Letters, 2013. **13**(11): p. 5698-5702.

150. Li, S.-S., et al., *Interplay of three-dimensional morphologies and photocarrier dynamics of polymer/TiO2 bulk heterojunction solar cells.* Journal of the American Chemical Society, 2011. **133**(30): p. 11614-11620.

151. Lv, L., et al., *Self-assembled TiO2 nanorods as electron extraction layer for high-performance inverted polymer solar cells.* Chemistry of Materials, 2015. **27**(1): p. 44-52.

152. Coakley, K.M., Liu, Y., Goh, C., and McGehee, M.D., *Ordered organic–inorganic bulk heterojunction photovoltaic cells.* MRS bulletin, 2005. **30**(01): p. 37-40.

153. McGehee, M.D., *Nanostructured organic–inorganic hybrid solar cells.* MRS bulletin, 2009. **34**(02): p. 95-100.

154. Jiang, X., Herricks, T., and Xia, Y., *Monodispersed spherical colloids of titania: synthesis, characterization, and crystallization.* Advanced Materials, 2003. **15**(14): p. 1205-1209.

155. Trentler, T.J., et al., *Synthesis of TiO2 nanocrystals by nonhydrolytic solution-based reactions.* Journal of the American Chemical Society, 1999. **121**(7): p. 1613-1614.

156. Wang, C.-C. and Ying, J.Y., *Sol-gel synthesis and hydrothermal processing of anatase and rutile titania nanocrystals.* Chemistry of Materials, 1999. **11**(11): p. 3113-3120.

157. Stafford, U., Gray, K.A., Kamat, P.V., and Varma, A., *An in situ diffuse reflectance FTIR investigation of photocatalytic degradation of 4-chlorophenol on a TiO2 powder surface.* Chemical physics letters, 1993. **205**(1): p. 55-61.

158. Riegel, G. and Bolton, J.R., *Photocatalytic efficiency variability in TiO2 particles.* The Journal of Physical Chemistry, 1995. **99**(12): p. 4215-4224.

159. Hurum, D.C., et al., *Explaining the enhanced photocatalytic activity of Degussa P25 mixed-phase TiO2 using EPR.* The Journal of Physical Chemistry B, 2003. **107**(19): p. 4545-4549.

160. Sun, C., et al., *Titania-water interactions: a review of theoretical studies.* Journal of Materials Chemistry, 2010. **20**(46): p. 10319-10334.

161. Gordon, T.R., et al., *Nonaqueous synthesis of TiO2 nanocrystals using TiF4 to engineer morphology, oxygen vacancy concentration, and photocatalytic activity.* Journal of the American Chemical Society, 2012. **134**(15): p. 6751-6761.

162. Joo, J., et al., *Large-scale synthesis of TiO2 nanorods via nonhydrolytic sol-gel ester elimination reaction and their application to photocatalytic inactivation of E. coli.* The Journal of Physical Chemistry B, 2005. **109**(32): p. 15297-15302.

163. Cozzoli, P.D., Kornowski, A., and Weller, H., *Low-temperature synthesis of soluble and processable organic-capped anatase TiO2 nanorods.* Journal of the American Chemical Society, 2003. **125**(47): p. 14539-14548.

164. Wu, B., et al., *Nonaqueous production of nanostructured anatase with high-energy facets.* Journal of the American Chemical Society, 2008. **130**(51): p. 17563-17567.

165. Salgueiriño-Maceira, V., Liz-Marzán, L.M., and Farle, M., *Water-based ferrofluids from FexPt1-x nanoparticles synthesized in organic media.* Langmuir, 2004. **20**(16): p. 6946-6950.

166. Zhang, Q., Liu, Y., and Yin, Y., unpublished.

167. Liu, Y., Tang, A., Zhang, Q., and Yin, Y., submitted.

168. Donnay, J.D.H. and Harker, D., *A new law of crystal morphology extending the law of Bravais.* American Mineralogist, 1937. **22**(5): p. 446-467.

169. Hartman, P. and Perdok, W.G., *On the relations between structure and morphology of crystals. I.* Acta Crystallographica, 1955. **8**(1): p. 49-52.

170. Penn, R.L. and Banfield, J.F., *Morphology development and crystal growth in nanocrystalline aggregates under hydrothermal conditions: insights from titania.* Geochimica et Cosmochimica Acta, 1999. **63**(10): p. 1549-1557.

171. Peng, Z.A. and Peng, X., *Mechanisms of the shape evolution of CdSe nanocrystals.* Journal of the American Chemical Society, 2001. **123**(7): p. 1389-1395.

172. Anker, J.N., et al., *Biosensing with plasmonic nanosensors.* Nature Materials, 2008. **7**(6): p. 442-453.

173. Hu, M.-S., et al., *Photosensitive gold-nanoparticle-embedded dielectric nanowires.* Nature Materials, 2006. **5**(2): p. 102-106.

174. Huang, X., Jain, P.K., El-Sayed, I.H., and El-Sayed, M.A., *Plasmonic photothermal therapy (PPTT) using gold nanoparticles.* Lasers in Medical Science, 2008. **23**(3): p. 217-228.

175. Huang, X., El-Sayed, I.H., Qian, W., and El-Sayed, M.A., *Cancer cell imaging and photothermal therapy in the near-infrared region by using gold nanorods.* Journal of the American Chemical Society, 2006. **128**(6): p. 2115-2120.

176. Nie, S. and Emory, S.R., *Probing single molecules and single nanoparticles by surface-enhanced Raman scattering.* Science, 1997. **275**(5303): p. 1102-1106.

177. Li, W., Camargo, P.H.C., Lu, X., and Xia, Y., *Dimers of silver nanospheres: facile synthesis and their use as hot spots for surface-enhanced Raman scattering.* Nano Letters, 2008. **9**(1): p. 485-490.

178. McFarland, A.D., Young, M.A., Dieringer, J.A., and Van Duyne, R.P., *Wavelength-scanned surface-enhanced Raman excitation spectroscopy.* The Journal of Physical Chemistry B, 2005. **109**(22): p. 11279-11285.

179. Link, S. and El-Sayed, M.A., *Spectral properties and relaxation dynamics of surface plasmon electronic oscillations in gold and silver nanodots and nanorods.* The Journal of Physical Chemistry B, 1999. **103**(40): p. 8410-8426.

180. Pastoriza-Santos, I. and Liz-Marzán, L.M., *Colloidal silver nanoplates. State of the art and future challenges.* Journal of Materials Chemistry, 2008. **18**(15): p. 1724-1737.

181. Gao, C., et al., *Fully alloyed Ag/Au nanospheres: combining the plasmonic property of Ag with the stability of Au.* Journal of the American Chemical Society, 2014. **136**(20): p. 7474-7479.

182. Jiang, R., et al., *Unraveling the evolution and nature of the plasmons in (Au core)–(Ag shell) nanorods.* Advanced Materials, 2012. **24**(35): p. OP200-OP207.

183. Sönnichsen, C., Reinhard, B.M., Liphardt, J., and Alivisatos, A.P., *A molecular ruler based on plasmon coupling of single gold and silver nanoparticles.* Nature Biotechnology, 2005. **23**(6): p. 741-745.

184. Halas, N.J., et al., *Plasmons in strongly coupled metallic nanostructures.* Chemical Reviews, 2011. **111**(6): p. 3913-3961.

185. Lin, S., et al., *One-dimensional plasmon coupling by facile self-assembly of gold nanoparticles into branched chain networks.* Advanced Materials, 2005. **17**(21): p. 2553-2559.

186. Taladriz-Blanco, P., et al., *Reversible assembly of metal nanoparticles induced by penicillamine. Dynamic formation of SERS hot spots.* Journal of Materials Chemistry, 2011. **21**(42): p. 16880-16887.

187. Barrow, S.J., et al., *Surface plasmon resonances in strongly coupled gold nanosphere chains from monomer to hexamer.* Nano Letters, 2011. **11**(10): p. 4180-4187.

188. Zhu, M.-Q., Wang, L.-Q., Exarhos, G.J., and Li, A.D.Q., *Thermosensitive gold nanoparticles.* Journal of the American Chemical Society, 2004. **126**(9): p. 2656-2657.

189. Li, D., He, Q., Cui, Y., and Li, J., *Fabrication of pH-responsive nanocomposites of gold nanoparticles/poly (4-vinylpyridine).* Chemistry of Materials, 2007. **19**(3): p. 412-417.

190. Elghanian, R., et al., *Selective colorimetric detection of polynucleotides based on the distance-dependent optical properties of gold nanoparticles.* Science, 1997. **277**(5329): p. 1078-1081.

191. Maye, M.M., et al., *Mediator-template assembly of nanoparticles.* Journal of the American Chemical Society, 2005. **127**(5): p. 1519-1529.

192. Lu, Z., Goebl, J., Ge, J., and Yin, Y., *Self-assembly and tunable plasmonic property of gold nanoparticles on mercapto-silica microspheres.* Journal of Materials Chemistry, 2009. **19**(26): p. 4597-4602.

193. Kim, T., Lee, K., Gong, M.-s., and Joo, S.-W., *Control of gold nanoparticle aggregates by manipulation of interparticle interaction.* Langmuir, 2005. **21**(21): p. 9524-9528.

194. Corezzi, S., et al., *Connecting irreversible to reversible aggregation: time and temperature.* The Journal of Physical Chemistry B, 2009. **113**(5): p. 1233-1236.

195. Wang, Y., et al., *A systems approach towards the stoichiometry-controlled hetero-assembly of nanoparticles.* Nature Communications, 2010. **1**: p. 87.

196. Sun, Z., et al., *pH-controlled reversible assembly and disassembly of gold nanorods.* Small, 2008. **4**(9): p. 1287-1292.

197. Hazarika, P., Ceyhan, B., and Niemeyer, C.M., *Reversible switching of DNA–gold nanoparticle aggregation.* Angewandte Chemie, 2004. **116**(47): p. 6631-6633.

198. Nergiz, S.Z. and Singamaneni, S., *Reversible tuning of plasmon coupling in gold nanoparticle chains using ultrathin responsive polymer film.* ACS Applied Materials & Interfaces, 2011. **3**(4): p. 945-951.

199. Fava, D., Winnik, M.A., and Kumacheva, E., *Photothermally-triggered self-assembly of gold nanorods.* Chemical Communications, 2009(18): p. 2571-2573.

200. Wang, C., Flynn, N.T., and Langer, R., *Controlled structure and properties of thermoresponsive nanoparticle–hydrogel composites.* Advanced Materials, 2004. **16**(13): p. 1074-1079.

201. Bhattacharjee, R.R., Chakraborty, M., and Mandal, T.K., *Reversible association of thermoresponsive gold nanoparticles: polyelectrolyte effect on the lower critical solution temperature of poly (vinyl methyl ether).* The Journal of Physical Chemistry B, 2006. **110**(13): p. 6768-6775.

202. Zhang, H. and Wang, D., *Controlling the growth of charged-nanoparticle chains through interparticle electrostatic repulsion.* Angewandte Chemie, 2008. **120**(21): p. 4048-4051.

203. Zhang, H., et al., *Controlled chainlike agglomeration of charged gold nanoparticles via a deliberate interaction balance.* The Journal of Physical Chemistry C, 2008. **112**(43): p. 16830-16839.

204. Yang, M., et al., *Mechanistic investigation into the spontaneous linear assembly of gold nanospheres.* Physical Chemistry Chemical Physics, 2010. **12**(38): p. 11850-11860.

205. Chen, T., et al., *Tailoring plasmon coupling in self-assembled one-dimensional Au nanoparticle chains through simultaneous control of size and gap separation.* The Journal of Physical Chemistry Letters, 2013. **4**(13): p. 2147-2152.

206. Collier, C.P., Vossmeyer, T., and Heath, J.R., *Nanocrystal superlattices.* Annual Review of Physical Chemistry, 1998. **49**(1): p. 371-404.

207. Kotov, N.A., Meldrum, F.C., Wu, C., and Fendler, J.H., *Monoparticulate layer and Langmuir-Blodgett-type multiparticulate layers of size-quantized cadmium sulfide clusters: a colloid-chemical approach to superlattice construction.* The Journal of Physical Chemistry, 1994. **98**(11): p. 2735-2738.

208. Murray, C.B., Kagan, C.R., and Bawendi, M.G., *Synthesis and characterization of monodisperse nanocrystals and close-packed nanocrystal assemblies.* Annual Review of Materials Science, 2000. **30**(1): p. 545-610.

209. Han, X., Li, Y., Wu, S., and Deng, Z., *A general strategy toward pH-controlled aggregation–dispersion of gold nanoparticles and single-walled carbon nanotubes.* Small, 2008. **4**(3): p. 326-329.

210. Han, X., Goebl, J., Lu, Z., and Yin, Y., *Role of salt in the spontaneous assembly of charged gold nanoparticles in ethanol.* Langmuir, 2011. **27**(9): p. 5282-5289.

211. Liao, J.H., et al., *Self-assembly of length-tunable gold nanoparticle chains in organic solvents.* Applied Physics A, 2003. **76**(4): p. 541-543.

212. Liu, Y., Han, X., He, L., and Yin, Y., *Thermoresponsive assembly of charged gold nanoparticles and their reversible tuning of plasmon coupling.* Angewandte Chemie International Edition, 2012. **51**(26): p. 6373-6377.

213. Pramod, P. and Thomas, K.G., *Plasmon coupling in dimers of Au nanorods.* Advanced Materials, 2008. **20**(22): p. 4300-4305.

214. Girard, C., Dujardin, E., Li, M., and Mann, S., *Theoretical near-field optical properties of branched plasmonic nanoparticle networks.* Physical Review Letters, 2006. **97**(10): p. 100801.

215. Djabourov, M., Clark, A.H., Rowlands, D.W., and Ross-Murphy, S.B., *Small-angle x-ray scattering characterization of agarose sols and gels.* Macromolecules, 1989. **22**(1): p. 180-188.

216. Narayanan, J., Xiong, J.-Y., and Liu, X.-Y. *Determination of agarose gel pore size: Absorbance measurements vis a vis other techniques*. Journal of Physics: Conference Series.

217. Liu, J., Shih, W.Y., Sarikaya, M., and Aksay, I.A., *Fractal colloidal aggregates with finite interparticle interactions: Energy dependence of the fractal dimension.* Physical Review A, 1990. **41**(6): p. 3206.

218. Feke, D.L., Prabhu, N.D., Mann Jr, J.A., and Mann Iii, J.A., *A formulation of the short-range repulsion between spherical colloidal particles.* The Journal of Physical Chemistry, 1984. **88**(23): p. 5735-5739.

219. Parsegian, V.A. and Weiss, G.H., *Spectroscopic parameters for computation of van der Waals forces.* Journal of Colloid and Interface Science, 1981. **81**(1): p. 285-289.

220. Enustun, B.V. and Turkevich, J., *Coagulation of colloidal gold.* Journal of the American chemical society, 1963. **85**(21): p. 3317-3328.

221. Richardi, J., *One-dimensional assemblies of charged nanoparticles in water: A simulation study.* The Journal of Chemical Physics, 2009. **130**(4): p. 044701.

222. Elimelech, M., Gregory, J., Jia, X., and Williams, R., *Particle Deposition and Aggregation, Measurement, Modeling and Simulation.* Colloids and Surfaces A: Physicochemical and Engineering Aspects, 1997. **1**(125): p. 93-94.

223. Revil, A., Pezard, P.A., and Glover, P.W.J., *Streaming potential in porous media: 1. Theory of the zeta potential.* Journal of Geophysical Research: Solid Earth (1978–2012), 1999. **104**(B9): p. 20021-20031.

224. Venditti, R., Xuan, X., and Li, D., *Experimental characterization of the temperature dependence of zeta potential and its effect on electroosmotic flow velocity in microchannels.* Microfluidics and Nanofluidics, 2006. **2**(6): p. 493-499.

225. Revil, A., Hermitte, D., Spangenberg, E., and Cochémé, J.J., *Electrical properties of zeolitized volcaniclastic materials.* Journal of Geophysical Research: Solid Earth (1978–2012), 2002. **107**(B8).

226. Reppert, P.M. and Morgan, F.D., *Temperature-dependent streaming potentials: 1. Theory.* Journal of Geophysical Research: Solid Earth (1978–2012), 2003. **108**(B11).

227. Long, J.A., Osmond, D.W.J., and Vincent, B., *The equilibrium aspects of weak flocculation.* Journal of Colloid and Interface Science, 1973. **42**(3): p. 545-553.

228. Bentz, J. and Nir, S., *Aggregation of colloidal particles modeled as a dynamical process.* Proceedings of the National Academy of Sciences, 1981. **78**(3): p. 1634-1637.

229. Liu, Y. and Yin, Y., unpublished.

230. Wang, H., et al., *Unconventional Chain-Growth Mode in the Assembly of Colloidal Gold Nanoparticles.* Angewandte Chemie International Edition, 2012. **51**(32): p. 8021-8025.

231. Han, X., Liu, Y., and Yin, Y., *Colorimetric Stress Memory Sensor Based on Disassembly of Gold Nanoparticle Chains.* Nano Letters, 2014. **14**(5): p. 2466-2470.

232. Balazs, A.C., Emrick, T., and Russell, T.P., *Nanoparticle polymer composites: where two small worlds meet.* Science, 2006. **314**(5802): p. 1107-1110.

233. Dinç, E. and Baleanu, D., *Multicomponent quantitative resolution of binary mixtures by using continuous wavelet transform.* Journal of AOAC International, 2004. **87**(2): p. 360-365.

234. Esteban, R., Taylor, R.W., Baumberg, J.J., and Aizpurua, J., *How chain plasmons govern the optical response in strongly interacting self-assembled metallic clusters of nanoparticles.* Langmuir, 2012. **28**(24): p. 8881-8890.

235. Feldstein, M.M., Shandryuk, G.A., Kuptsov, S.A., and Platé, N.A., *Coherence of thermal transitions in poly (N-vinyl pyrrolidone)–poly (ethylene glycol) compatible blends 1. Interrelations among the temperatures of melting, maximum cold crystallization rate and glass transition.* Polymer, 2000. **41**(14): p. 5327-5338.

236. Milliron, D.J., Gur, I., and Alivisatos, A.P., *Hybrid organic–nanocrystal solar cells.* MRS bulletin, 2005. **30**(01): p. 41-44.

237. Xia, H., Bai, S., Hartmann, J.r., and Wang, D., *Synthesis of monodisperse quasi-spherical gold nanoparticles in water via silver (I)-assisted citrate reduction.* Langmuir, 2009. **26**(5): p. 3585-3589.